

AD-A195 489

DTIC FILE COPY

(2)

AFOSR-TR. 88-0457

A Study of the Fatigue Behavior of Small Cracks in Nickel-Base  
Superalloys

Final Report

Submitted to

Air Force Office of Scientific Research  
Grant # AFOSR-84-0075

Attention: Dr. A. Rosenstein

by

Professor Regis M. Pelloux  
Dr. Jun Feng  
Glenn Romanoski  
Department of Materials Science & Engineering  
Massachusetts Institute of Technology  
77 Massachusetts Avenue  
Cambridge, MA 02139

February 24, 1988

DTIC  
ELECTE  
MAY 03 1988  
S D  
G H

DISTRIBUTION STATEMENT A

Approved for public release;  
Distribution Unlimited

88 8 02 227

REPORT DOCUMENTATION PAGE				Form Approved OMB No. 0704-0188	
1a. REPORT SECURITY CLASSIFICATION UNCLASSIFIED			1b. RESTRICTIVE MARKINGS		
2a. SECURITY CLASSIFICATION AUTHORITY			3. DISTRIBUTION / AVAILABILITY OF REPORT		
2b. DECLASSIFICATION / DOWNGRADING SCHEDULE			UNLIMITED		
4. PERFORMING ORGANIZATION REPORT NUMBER(S)			5. MONITORING ORGANIZATION REPORT NUMBER(S)		
			AFOSR-TR- 88 - 0457		
6a. NAME OF PERFORMING ORGANIZATION Massachusetts Inst of Tech		6b. OFFICE SYMBOL (If applicable)	7a. NAME OF MONITORING ORGANIZATION AFOSR/NE		
6c. ADDRESS (City, State, and ZIP Code) 77 Massachusetts Avenue Cambridge, MA 02139			7b. ADDRESS (City, State, and ZIP Code) Bldg 410 Bolling AFB, DC 20332-6448		
8a. NAME OF FUNDING / SPONSORING ORGANIZATION AFOSR/NE		8b. OFFICE SYMBOL (If applicable) NE	9. PROCUREMENT INSTRUMENT IDENTIFICATION NUMBER AFOSR-84-0075		
8c. ADDRESS (City, State, and ZIP Code) Bldg 410 Bolling AFB, DC 20332-6448			10. SOURCE OF FUNDING NUMBERS		
	PROGRAM ELEMENT NO.	PROJECT NO.	TASK NO.	WORK UNIT ACCESSION NO.	
	61102F	2306	A1		
1. TITLE (Include Security Classification) A STUDY OF THE FATIGUE BEHAVIOR OF SMALL CRACKS IN NICKEL-BASE SUPERALLOYS					
12. PERSONAL AUTHOR(S) Professor Regis M Pelloux					
13a. TYPE OF REPORT Final Report		13b. TIME COVERED FROM 01 Jan 84 TO 1 Aug 87	14. DATE OF REPORT (Year, Month, Day)		15. PAGE COUNT
16. SUPPLEMENTARY NOTATION					
17. COSATI CODES			18. SUBJECT TERMS (Continue on reverse if necessary and identify by block number)		
FIELD	GROUP	SUB-GROUP			
19. ABSTRACT (Continue on reverse if necessary and identify by block number)					
<p>→ The fatigue of behavior of short cracks was investigate in five wrought nickel-base superalloys currently used for aircraft turbine disks. The alloys and test temperature were: Inconel X-750 (25°C and 427°C), Inconel 718 (427°C), powder metallurgy Rene 95 (25°C) and powder metallurgy IN100 (649°C). Cracks were initiated at artificial defects and at persistent slip bands. Test frequencies ranged from 20Hz to 10cpm. Fatigue crack growth rates were measured over crack lengths ranging from 10um to 1mm. Most of the testing was performed in load control with stress ranges approaching the cyclic yield strengths of alloys. Strain controlled tests were performed on IN100 under elastic-plastic cycling conditions. <i>work: crack propagation physical metallurgy</i></p>					
20. DISTRIBUTION / AVAILABILITY OF ABSTRACT <input type="checkbox"/> UNCLASSIFIED/UNLIMITED <input type="checkbox"/> SAME AS RPT. <input type="checkbox"/> DTIC USERS			21. ABSTRACT SECURITY CLASSIFICATION UNCLASSIFIED		
22a. NAME OF RESPONSIBLE INDIVIDUAL DR ROSENSTEIN			22b. TELEPHONE (Include Area Code) 202-767-4933		22c. OFFICE SYMBOL NE

## ABSTRACT

The fatigue behavior of small cracks was investigated in five wrought nickel-base superalloys currently used for aircraft turbine disks. The alloys and test temperature were: Inconel X-750 (25° C), Waspaloy (25° C and 427° C), Inconel 718 (427° C), powder metallurgy René 95 (25° C) and powder metallurgy IN100 (649° C). Cracks were initiated at artificial defects and at persistent slip bands. Test frequencies ranged from 20 Hz to 10 cpm. Fatigue crack growth rates were measured over crack lengths ranging from 10  $\mu$ m to 1 mm. Most of the testing was performed in load control with stress ranges approaching the cyclic yield strengths of the alloys. Strain controlled tests were performed on IN100 under elastic-plastic cycling conditions.

In room temperature tests of X-750 and Waspaloy, fatigue cracks are strongly crystallographic and their growth rates are grain size dependent. Small cracks grew at higher rates in large grains than long cracks at the same calculated nominal value of  $\Delta K$ . In these two alloys grain boundaries served as obstacles to crack extension resulting in considerable scatter in  $\Delta K_{TH}$  and near threshold crack growth rates. In fine grained materials such as René 95, the fatigue crack growth rates of small cracks correlate well with  $\Delta K$ . The data is in agreement with long crack results.

In elevated temperature tests under elastic cyclic loading conditions the fatigue crack growth rates of small cracks ( $a \geq 100 \mu$ m) correlate very well with  $\Delta K$ . The upper bound of the  $da/dN$  -  $\Delta K$  data for small cracks coincides with the data for long cracks.

At elevated temperatures in the elastic-plastic regime where the maximum cyclic stress reaches the macroscopic yield stress, the fatigue crack growth rates for  $100 \mu$ m  $\leq a \leq 300 \mu$ m are independent of crack length. This test regime needs further investigation.



By _____	
Distribution/ _____	
Availability Codes _____	
Dist _____	Avail and/or Special _____
A-1	

### ACKNOWLEDGEMENTS

This investigation was performed under sponsorship of the Air Force Office of Scientific Research under Grant # AFOSR-84-0075. Dr. A. Rosenstein was grant monitor.

The authors would like to thank: M. Blackburn, J. Hill and V. Moreno of Pratt and Whitney Aircraft; D. Backman, R. H. Van Stone, M. Henry and D. Krueger of General Electric; and K. Bain of Allison Gas Turbine Division of General Motors for material support and valuable discussions. Special thanks go to S. Doucette for typing this report.

## TABLE OF CONTENTS

	<u>PAGE</u>
ABSTRACT.....	i
ACKNOWLEDGEMENTS.....	ii
TABLE OF CONTENTS.....	iii
LIST OF TABLES.....	iv
LIST OF FIGURES.....	v
1. INTRODUCTION.....	1
2. EXPERIMENTAL PROCEDURES.....	3
2.1 Materials.....	3
2.1.1 Inconel X-750.....	3
2.1.2 Waspaloy.....	4
2.1.3 Inconel 718.....	4
2.1.4 René 95 (PM).....	5
2.1.5 IN100 (PM).....	6
2.2 Test Specimen Geometry.....	6
2.2.1 Room Temperature Tests.....	6
2.2.2 Elevated Temperature Tests.....	7
2.3 Specimen Preparation.....	7
2.4 Initiation of Short Cracks.....	8
2.4.1 Crack Initiation from EDM Pits.....	9
2.4.2 Crack Initiation from Nd-YAG Laser Generated Defects.....	9
2.4.3 Crack Initiation from Al <sub>2</sub> O <sub>3</sub> particles.....	10
2.4.4 Precracking.....	10
2.5 Crack Length Measurement by Plastic Replica.....	11
2.6 Crack Length Measurement by A. C. Potential Drop.....	12
2.7 Small Crack Growth Testing at Room Temperature.....	12
2.8 Small Crack Growth Testing at Elevated Temperature.....	13
3. DATA ANALYSIS .....	28
3.1 Computation of Crack Growth Rates.....	29

3.2 Stress Intensity Factor Calculations.....	30
4. RESULTS AND DISCUSSION.....	37
4.1 Fatigue Behavior of Small Cracks at Room Temperature.....	37
4.1.1 Inconel X-750.....	37
4.1.2 Waspaloy.....	41
4.1.3 René 95 (PM).....	42
4.1.4 Fractography, Room Temperature Tests.....	43
4.2 Fatigue Behavior of Small Cracks at Elevated Temperature.....	75
4.2.1 Waspaloy, 427°C.....	75
4.2.2 Inconel 718, 427°C.....	78
4.2.3 IN100 (PM), 649°C.....	80
4.2.4 Fractography, Elevated Temperature Tests.....	81
5. CONCLUSIONS.....	120
REFERENCES.....	122
APPENDIX A: A Multi-Frequency A. C. Potential Drop System for the Measurement of Fatigue Micro-Cracks.....	125
LIST OF TABLES.....	iv
Table 2.1 Alloy and Test Temperature.....	3
Table 2.2 Chemical Compositions.....	15
Table 2.3 Heat Treatment Conditions.....	16
Table 2.4 Mechanical Properties.....	17
Table 2.5 Small Crack Fatigue Tests at Room Temperature.....	18
Table 2.6 Small Crack Fatigue Tests at Elevated Temperature.....	19

## List of Figures

- Figure 2.1 Typical microstructures for: a) Inconel X-750 and b) Waspaloy used in this investigation.
- Figure 2.2 Typical microstructure for Inconel 718 used in this investigation.
- Figure 2.3 Typical microstructures for: a) powder metallurgy René 95 and b) powder metallurgy IN100.
- Figure 2.4 Specimen geometry used for room temperature tests.
- Figure 2.5 Specimen geometry used for elevated temperature tests.
- Figure 2.6 Modification to specimen gauge section, shown in Figure 2.5, used for elevated temperature tests.
- Figure 2.7 a) A typical EDM defect and fatigue crack shown here in the surface of Inconel X-750.  
b) A typical laser defect and fatigue crack shown here in the surface of Waspaloy.
- Figure 2.8 a) Fatigue crack initiation at an  $\text{Al}_2\text{O}_3$  particle in powder metallurgy René 95.  
b) Fatigue crack initiation at PSB's in Waspaloy tested at room temperature.
- Figure 3.1 Crack front profiles as evidenced by the presence of oxidation on the fracture surfaces of Waspaloy specimens tested at 427° C.
- Figure 3.2 The aspect ratio,  $c/a$  versus  $c$  for numerous cracks in Waspaloy tested at 427° C under several stress ranges.
- Figure 3.3 a) Elliptical crack embedded in an infinite solid subjected to a uniform stress.  
b) Surface crack in a finite plate subjected to a uniform stress (from Ref. 10).
- Figure 4.1 Normalized relation between threshold stress and crack length for Inconel X-750 tested at 25C,  $R = 0.05$ .
- Figure 4.2 Normalized relation between threshold stress intensity factor range and crack length for Inconel X-750 tested at 25C,  $R = 0.05$ .
- Figure 4.3 Normalized relation between threshold stress intensity factor range and load ratio,  $R$ , for Inconel X-750 tested at 25° C.
- Figure 4.4 Normalized relation between threshold stress intensity factor and load ratio,  $R$ , for Inconel X-750 tested at 25° C.

- Figure 4.5 Fatigue crack growth rates versus stress intensity factor range for Inconel X-750 tested at 25° C,  $R = -1$ .
- Figure 4.6 Fatigue crack growth rates versus stress intensity factor range for Inconel X-750 tested at 25° C,  $R = 0.05$ .
- Figure 4.7 Fatigue crack growth rates versus stress intensity factor range for Inconel X-750 tested at 25° C,  $R = 0.5$ .
- Figure 4.8 Summary of the fatigue crack growth rates versus stress intensity factor range for Inconel X-750 tested at 25° C,  $R$  ratio varied.
- Figure 4.9 Crack length versus cycle number for Waspaloy tested at 25° C, Max. Stress varied,  $R = -1$ .
- Figure 4.10 Crack length versus cycle number for Waspaloy tested at 25° C, Max. Stress = 758 MPa,  $R$  ratio varied.
- Figure 4.11 Summary of fatigue crack growth rates versus stress intensity factor range for Waspaloy, tested at 25° C,  $R = -1$ .
- Figure 4.12 Summary of fatigue crack growth rates versus stress intensity factor range for Waspaloy, tested at 25° C,  $R = 0$ .
- Figure 4.13 Fatigue crack growth rates versus stress intensity factor range for Waspaloy, tested at 25° C, Max. Stress = 758 MPa,  $R = 0.5$ .
- Figure 4.14 Summary of fatigue crack growth rates versus stress intensity factor range for Waspaloy, tested at 25° C,  $R$  varied.
- Figure 4.15 Crack length versus cycle number for René 95 (PM) tested at 25° C, Max. Stress = 758 MPa,  $R$  varied.
- Figure 4.16 Crack length versus cycle number for René 95 (PM) tested at 25° C, Max. Stress was varied,  $R = -1$ .
- Figure 4.17 Fatigue crack growth rates versus stress intensity factor range for René 95 (PM), tested at 25° C, Max. Stress = 758 MPa,  $R = -1$ .
- Figure 4.18 Fatigue crack growth rates versus stress intensity factor range for René 95 (PM), tested at 25° C, Max. Stress = 483 MPa,  $R = -1$ .
- Figure 4.19 Summary of fatigue crack growth rates versus stress intensity factor range for René 95 (PM), tested at 25° C,  $R = -1$ .
- Figure 4.20 Fatigue crack growth rates versus stress intensity factor range for René 95 (PM), tested at 25° C, Max. Stress = 758 MPa,  $R = 0$ .
- Figure 4.21 Fatigue crack growth rates versus stress intensity factor range for René 95 (PM), tested at 25° C, Max. Stress = 758 MPa,  $R = 0.5$ .
- Figure 4.22 Summary of fatigue crack growth rates versus stress intensity factor range for René 95 (PM), tested at 25° C, Max. Stress and  $R$  ratio were varied.



- Figure 4.23 Scanning Electron Micrographs of small cracks initiated from an EDM pit in Inconel X-750, tests at 25° C.
- Figure 4.24 Scanning Electron Micrographs of the fracture surface of the small crack in Figure 4.23.
- Figure 4.25 Scanning Electron Micrographs of the fracture surface in Inconel X-750 tested at 25° C.
- Figure 4.26 Angle distribution spectrum of a small crack with length 900  $\mu\text{m}$  in Inconel X-750, tested at 25° C.
- Figure 4.27 Scanning Electron Micrographs of a small crack in René 95 (PM) tested at 25° C: a) crack root, b) crack up.
- Figure 4.28 Scanning Electron Micrographs of the fracture surface of a small crack in René 95 (PM) tested at 25° C.
- Figure 4.29 Micrograph of small cracks initiated from an EDM pit in Waspaloy tested at 25° C.
- Figure 4.30 Micrographs of fatigue cracks in persistent slip bands in Waspaloy tested at 25° C.
- Figure 4.31 Crack depth versus cycle number for Waspaloy tested at 427° C, Max. Stress = 504 MPa, R = -1, Freq. = 0.33 Hz.
- Figure 4.32 Crack growth rate versus stress intensity factor range for Waspaloy tested at 427° C, Max. Stress = 504 MPa, R = -1, Freq. = 0.33 Hz.
- Figure 4.33 Crack depth versus cycle number for Waspaloy tested at 427° C, Max. Stress = 621 MPa, R = -1, Freq. = 0.33 Hz.
- Figure 4.34 Crack growth rate versus stress intensity factor range for Waspaloy tested at 427° C, Max. Stress = 621 MPa, R = -1, Freq. = 0.33 Hz.
- Figure 4.35 Crack depth versus cycle number for Waspaloy tested at 427° C, Max. Stress = 754 MPa, R = -1, Freq. = 0.33 Hz.
- Figure 4.36 Crack growth rate versus stress intensity factor range for Waspaloy tested at 427° C, Max. Stress = 754 MPa, R = -1, Freq. = 0.33 Hz.
- Figure 4.37 Summary of crack growth rate versus stress intensity factor range for Waspaloy tested at 427° C, Max. Stress was varied with R = -1, Freq. = 0.33 Hz.
- Figure 4.38 Crack depth versus cycle number for Waspaloy tested at 427° C, Max. Stress = 766 MPa, R = 0, Freq. = 0.33 Hz.
- Figure 4.39 Crack growth rate versus stress intensity factor range for Waspaloy tested at 427° C, Max. Stress = 766 MPa, R = 0, Freq. = 0.33 Hz.

- Figure 4.40 Crack depth versus cycle number for Waspaloy tested at 427° C, Max. Stress = 765 MPa, R = 0.3, Freq. = 0.33 Hz.
- Figure 4.41 Crack growth rate versus stress intensity factor range for Waspaloy tested at 427° C, Max. Stress = 765 MPa, R = 0.3, Freq. = 0.33 Hz.
- Figure 4.42 Crack depth versus cycle number for Waspaloy tested at 427° C, Max. Stress = 903 MPa, R = 0.5, Freq. = 0.33 Hz.
- Figure 4.43 Crack growth rate versus stress intensity factor range for Waspaloy tested at 427° C, Max. Stress = 903 MPa, R = 0.5, Freq. = 0.33 Hz.
- Figure 4.44 Summary of crack growth rate versus stress intensity factor range for Waspaloy tested at 427° C, Max. Stress 758 MPa & 903 MPa, R ratio was varied Freq. = 0.33 Hz.
- Figure 4.45 Comparison of crack growth rates versus stress intensity factor range for Waspaloy tested at 25° C and 427° C, R = -1.
- Figure 4.46 Comparison of crack growth rates versus stress intensity factor range for Waspaloy tested at 25° C and 427° C, R = 0.
- Figure 4.47 Crack depth versus cycle number for Inconel 718 tested at 427° C, Max. Stress = 621 MPa, R = -1, Freq. = 0.33 Hz.
- Figure 4.48 Crack growth rate versus stress intensity factor range for Inconel 718 tested at 427° C, Max. Stress = 621 MPa, R = -1, Freq. = 0.33 Hz.
- Figure 4.49 Crack depth versus cycle number for Inconel 718 tested at 427° C, Max. Stress = 758 MPa, R = -1, Freq. = 0.33 Hz.
- Figure 4.50 Crack growth rate versus stress intensity factor range for Inconel 718 tested at 427° C, Max. Stress = 758 MPa, R = -1, Freq. = 0.33 Hz.
- Figure 4.51 Summary of crack growth rate versus stress intensity factor range for Inconel 718 tested at 427° C, Max. Stress was varied, R = -1, Freq. = 0.33 Hz.
- Figure 4.52 Crack depth versus cycle number for Inconel 718 tested at 427° C, Max. Stress = 758 MPa, R = 0.05, Freq. = 0.33 Hz.
- Figure 4.53 Crack growth rate versus stress intensity factor range for Inconel 718 tested at 427° C, Max. Stress = 758 MPa, R = 0.05, Freq. = 0.33 Hz.
- Figure 4.54 Summary of crack growth rate versus stress intensity factor range for Inconel 718 tested at 427° C, Max. Stress = 758 MPa, R ratio was varied, Freq. = 0.33 Hz.
- Figure 4.55 Crack depth versus cycle number for IN100 (PM) tested at 649° C, Max. Stress = 758 MPa, R = 0.1, Freq. = 10 cpm.
- Figure 4.56 Crack growth rate versus stress intensity factor range for IN100 (PM) tested at 649° C, Max. Stress = 758 MPa, R = 0.1, Freq. = 10 cpm.

- Figure 4.57 First hysteresis loop for IN100 (PM) tested under strain control at 649° C, Average Max. Stress = 1100 MPa, Total Strain Range = 0 to 0.80%.
- Figure 4.58 Crack depth versus cycle number for IN100 (PM) tested under strain control at 649° C, Average Max. Stress = 1100 MPa, Total Strain Range = 0 to 0.80%.
- Figure 4.59 Crack growth rate versus stress intensity factor range for IN100 (PM) tested under strain control at 649° C, Average Max. Stress = 1100 MPa, Total Strain Range = 0 to 0.80%.
- Figure 4.60 Typical hysteresis loop for IN100 (PM) tested under strain control at 649° C, Average Max. Stress = 1026 MPa, Total Strain Range =  $\pm 0.55\%$ .
- Figure 4.61 Crack depth versus cycle number for IN100 (PM) tested under strain control at 649° C, Average Max. Stress = 1026 MPa, Total Strain Range =  $\pm 0.55\%$ .
- Figure 4.62 Crack growth rate versus stress intensity factor range for IN100 (PM) tested under strain control at 649° C, Average Max. Stress = 1026 MPa, Total Strain Range =  $\pm 0.55\%$ .
- Figure 4.63 Summary of crack growth rate versus stress intensity factor range for IN100 (PM) tested under load control and strain control at 649° C.
- Figure 4.64 Fractographs of Waspaloy tested at 427° C.
- Figure 4.65 (a) Optical micrograph of fatigue crack trace on gauge section surface and (b) SEM fractograph for Inconel 718 tested at 427° C.
- Figure 4.66 (a) SEM micrograph of a typical fracture surface and (b) SEM micrograph of pore and fatigue crack in gauge section surface after 150 cycles of strain controlled cycling at a total strain range of 0% to 0.80%

## 1. INTRODUCTION

Turbine disks are regarded as the most critical flight safety components of high performance jet engines. Presently, turbine disks are designed on the basis of a low-cycle fatigue (LCF) life limitation criterion which is in accordance with guidelines established by the Air Force Engine Structural Integrity Program (ENSIP) [1]. This LCF (cycles-to-crack-initiation) criterion tends to be conservative since it "builds in" a further life margin associated with crack propagation. Hence, there is considerable economic incentive to extend engine service lives by combining crack initiation and crack propagation criteria in life prediction methodologies of turbine disks.

Some materials are subject to premature fatigue crack initiation due to handling or machining damage, fretting, and intrinsic defects such as porosity and inclusions usually found in powder metallurgy (PM) alloys. Given initial premature cracking, it is necessary to employ a defect-tolerant design approach to assure adequate crack propagation lives from small initial defects and/or cracks.

To achieve either of the two goals described above, extending lives of LCF damaged disks or assuring safe lives for defect-containing disks, requires the application of a fracture mechanics type approach to very short cracks. This entails the determination of threshold and fatigue crack growth rates for short cracks at elevated temperatures.

It has recently been demonstrated that short crack fatigue behavior cannot be described accurately by conventional linear elastic fracture mechanics (LEFM). Consequently, developing a methodology for dealing with short crack behavior remains a critical but missing link in life management and design of gas turbine disks.

The objective of this research was to determine the fatigue crack growth behavior of small cracks in nickel-base superalloys at room temperature and at elevated temperatures. More specifically, the objective includes:

1. The measurement of crack growth rates in the low growth rate regime.
2. The determination of the threshold stress range,  $\Delta\sigma_{TH}$ , and/or the threshold stress intensity factor range,  $\Delta K_{TH}$ , for the nonpropagation of small fatigue cracks.
3. An evaluation of the effect of temperature and environment on near threshold fatigue growth rates of small cracks.
4. A determination of the conditions under which a small fatigue crack will be different from a long fatigue crack.

In this investigation, subject cracks will be referred to as "small cracks" to characterize them as being physically small. Crack depths considered were generally in the range of 50  $\mu\text{m}$  to 1mm. The terms "short crack" or "short crack effect" will be used to characterize the fatigue behavior of small cracks for which LEFM does not correlate crack growth rates with long crack results. Crack depth and semicrack length are synonymous.

## 2. EXPERIMENTAL PROCEDURES

### 2.1 Materials

The alloys selected for this investigation are five nickel-base superalloys. Four\* of these alloys are currently being used extensively for aircraft turbine disks. They include conventional cast and wrought alloys and powder metallurgy processed alloys. The alloys are listed in Table 2.1 with the test temperatures.

Table 2.1

<u>Alloy</u>	<u>Test Temperature</u>
Inconel X-750	25° C
* Waspaloy	25° C and 427° C
* Inconel 718	427° C
* René 95 (PM)	25° C
* IN100 (PM)	649° C

The chemical composition of these alloys are given in Table 2.2. The heat treatment conditions and grain sizes are given in Table 2.3. The relevant mechanical properties are given in Table 2.4.

#### 2.1.1 Inconel X-750

Inconel X-750 is a precipitation-hardened nickel-chromium alloy used for its corrosion and oxidation resistance and high strength up to 700° C. The heat treated alloy has useful strength up to 980° C. Typical applications include land-based gas turbine components, nuclear reactor springs, bellows and forming tools.

The Inconel X-750 used in this investigation was supplied by the International Nickel Company in the form of a 12.7 mm thick plate in the annealed condition. It was

given a two-stage heat treatment as described in Table 2.3. The typical microstructure of the heat-treated alloy is given in Figure 1a. The average grain size is about 130  $\mu\text{m}$  and uniform in all directions. The two-stage ageing treatment produces a bimodal distribution of  $\gamma'$  precipitates, the ordered intermetallic phase  $\text{Ni}_3(\text{Al}, \text{Ti})$  which is coherent with the austenite matrix  $\gamma$ . A coarse  $\gamma'$  phase ( $\sim 0.15 \mu\text{m}$ ) and a fine  $\gamma'$  phase ( $\sim 0.01 \mu\text{m}$ ) are present. The total volume fraction of  $\gamma'$  phase is approximately 20% [2, 3].

#### 2.1.2 Waspaloy

Waspaloy is a conventionally processed nickel-base superalloy which is used for aircraft turbine disks. The general structure of Waspaloy consists of a nickel rich austenite matrix ( $\gamma$ ) and is strengthened by  $\gamma'$  precipitates. Solid solution strengthening is provided by Co, Cr, and Mo. The high melting points of Ni and Co provide the basis for good mechanical properties at elevated temperatures [4].

This alloy was received as a hot rolled plate and given the heat treatment described in Table 2.3. The typical microstructure of the heat treated alloy is given in Figure 1b. The microstructure is comprised of a duplex grain structure with two different grain sizes. The large grains have a 200  $\mu\text{m}$  average diameter and the small grains a 7  $\mu\text{m}$  average diameter. The large grains give good creep properties to the detriment of low temperature tensile strength. The same lot of Waspaloy was used for short crack growth testing at room temperature and at 427° C as well as testing of conventional long crack specimens.

#### 2.1.3 Inconel 718

Alloy 718 is a precipitation hardened nickel-base superalloy. It is currently being used as an aircraft gas turbine disk material. The elements which primarily partition to the austenite phase,  $\gamma$ , are Cr and Mo. The Cr provides oxidation resistance while both Cr and Mo contribute to solid solution strengthening. The Nb, Ti and Al govern the phase precipitation characteristics while small additions of C and B are intended to enhance grain

boundary strength and ductility. Alloy 718 contains  $\gamma'$  and  $\gamma''$  precipitates phases.  $\gamma'$  is a metastable, ordered, coherent precipitate phase having an  $L1_2$  structure.  $\gamma''$  is a metastable, ordered, coherent precipitate phase having a body-centered tetragonal (BCT) crystal structure with a  $Ni_3(Nb, Al, Ti)$  stoichiometry. The total amount of  $\gamma'$  and  $\gamma''$  precipitate in Alloy 718 is approximately 19 volume percent [4].

The material used in this investigation was received in the form of hot rolled bars of 22.2 mm diameter from Huntington Alloys. The material was given the conventional solution plus 2-step ageing heat treatment as described in Table 2.3. The typical microstructure of the heat treated Inconel 718 is shown in Figure 2.2. The microstructure is nonuniform with grain sizes ranging from 5  $\mu m$  to 500  $\mu m$ . This is an unfortunate consequence of prior processing which cannot be rectified by heat treatment alone. Note that the solution temperature used in heat treatment, 955° C, is below the  $\delta$ -phase solvus near 982° C. It is the  $\delta$ -phase that inhibits grain boundary migration and controls grain size. Further grain refinement would require additional thermal-mechanical processing. We opted to proceed with the material as shown in Figure 2.2.

#### 2.1.4 René 95 (PM)

René 95 is a high strength nickel-based superalloy which is processed by powder metallurgy and is currently used for advanced aircraft turbine disks. Powders are produced by an argon gas atomization process. René 95 is reported to contain the following phases:  $\gamma$ , MC, MC',  $M_{23}C_6$  and  $M_3B_2$ . The microstructure of as HIP materials are generally quite homogeneous with large  $\gamma'$  particles (~5  $\mu m$ ) frequently observed at grain boundaries. The matrix contains both small (~0.2  $\mu m$ ) and intermediate (~2  $\mu m$ ) sized  $\gamma'$  particles [5].

In this investigation, René 95 powders of 140 mesh were used to make the compact. Before consolidation, the alloy powder was intentionally seeded with  $Al_2O_3$  particles with an average diameter of 114  $\mu m$ . The heat treatment employed is described in



Table 2.3. The typical microstructure of René 95 is shown in Figure 2.3a. The average grain diameter is about 5  $\mu\text{m}$ .

#### 2.1.5 IN100 (PM)

IN100 is high strength nickel based superalloy which is processed by powder metallurgy and is currently used for advanced aircraft turbine disks. Strengthening is based on a high volume fraction of  $\gamma$  precipitates which are coherent with the matrix. Solid solution strengthening elements and carbides play the same role in this alloy as in those described above [4]. This material was supplied by Pratt & Whitney Aircraft. Specimens were cut from a gatorized disk. The heat treatment employed is described in Table 2.3. The typical microstructure of IN100 (PM) is shown in Figure 2.3b. The Average grain diameter is about 3-5  $\mu\text{m}$ .

### 2.2 Test Specimen Geometry

#### 2.2.1 Room Temperature Tests

The specimen geometry employed in the investigation of fatigue behavior of short cracks in turbine disk alloys at room temperature is shown in Figure 2.4. This geometry was selected because it has the following advantages:

- 1) Flat surfaces can be easily ground and polished to a mirror finish.
- 2) Flat surfaces can be replicated over a larger area.
- 3) Large flat areas allow the monitoring of a greater number of propagating short cracks in each specimen.
- 4) Calculation of the stress intensity factor range is simplified for a flat surface.

In experiments where the maximum stress was high, the width of the specimen was reduced from 11.4 mm to 6.4 mm to prevent premature failure in the threads.

### 2.2.2 Elevated Temperature Tests

The two specimen geometries employed in the investigation of the fatigue behavior of short cracks in turbine disk alloys at elevated temperature are shown in Figure 2.5 and Figure 2.6. The specimen is essentially an axisymmetric button head low-cycle fatigue specimen of 6.35 mm diameter gauge section. It was chosen to be suitable for both elastic and elastic-plastic loading conditions. These specimens are induction heated and have a sufficiently long gauge length ( $l_0 = 19$  mm), of uniform cross section, for total longitudinal strain control testing. A modified low-cycle fatigue specimen with flats on opposite faces, Figure 2.6, was adopted when it was found that the curvature of the cylindrical specimen surface may have contributed to a deflection of the crack when the surface crack length exceeded about 600  $\mu$ m. This problem will be discussed later.

### 2.3 Specimen Preparation

All specimens used in this investigation were machined by low stress grinding or by electro-chemical machining. After low stress grinding, there exists a disturbed layer of about 50 to 100  $\mu$ m in depth which contains residual stresses [6]. This residual stress layer was removed to avoid interference with the propagation behavior of small cracks.

Removal of the residual stress layer was accomplished by the following procedures. Flat segments and round segments of specimen gauge sections were hand ground with successively finer grades of SiC paper; 240, 320, 400 and 600 grit sizes. Gauge section surfaces were ground in the longitudinal and transverse (circumferential) directions. Sharp corners were rounded to prevent crack initiation. In the final steps of hand grinding, 6  $\mu$ m diamond paste was used. Finally, the reduced section of each specimen was electropolished with a solution of 45% butyl-cellusolve, 45% acetic acid and

10% perchloric acid, at 40-50 volts for 30 seconds at a temperature of  $\sim 0$  to  $5^{\circ}$  C. Approximately  $100\text{ }\mu\text{m}$  of surface layer was removed by the procedure described above. When artificially introduced surface defects were used as crack initiation sites, they were processed at this time.

Thermocouples were spot welded to precise locations below the gauge section to control the temperature using the "set point" technique in elevated temperature tests.

#### 2.4 Initiation of Short Cracks

Two important and practical considerations dictate the use of artificial means to initiate fatigue micro-cracks. The first consideration is that, due to the statistical nature of small cracks, the probability of having a characteristically maximum size defect intersecting the surface of the gauge section of a laboratory test specimen is small. The second consideration is that measuring small crack lengths is experimentally difficult. However, this task can be greatly facilitated by knowing the exact location of the cracks.

The desired defect geometry is that which is conducive to crack initiation at the smallest possible defect size. Such a pseudo-crack should have a sharp defect tip radius and be oriented normal to the principal applied stress. The process employed to produce defects must not induce significant residual stresses or other large scale microstructural damage. In this investigation, small cracks were initiated using three types of artificially made defects:

- 1) electro-discharge machined (EDM) surface defects, hemispherical "pits"
- 2) elliptical surface defects created by a pulsed Nd-YAG laser
- 3) alumina particles intentionally introduced into powder metallurgy René 95 before powder consolidation.

Fatigue crack initiation sites at persistent slip bands (PSB's) in conventionally processed alloys and at micro-porosity in powder metallurgy alloys were also used in this study of small crack behavior.

#### 2.4.1 Crack Initiation from EDM Pits

For many of the crack propagation experiments carried out at room temperature short cracks were initiated at electro-discharge machined pits. These surface defects were made with a conventional EDM using a monel electrode with a conically shaped tip. The resulting defect is a hemispherical pit. A typical EDM pit can be seen in Figure 2.7a. There is a shallow cast layer of about 10  $\mu\text{m}$  thickness surrounding the pit. This technique leaves the surrounding matrix free of residual stress. The advantages of this technique are that it is experimentally expedient and reproducible. There are, however, limitations on minimum defect size and defect tip radius.

#### 2.4.2 Crack Initiation from Nd-YAG Laser Generated Defects

The EDM technique, using equipment presently available at MIT, was found to be limited to a minimum diameter of  $\sim 200 \mu\text{m}$ . In the course of testing it was soon realized that anomalous crack growth behavior in turbine disk alloys could likely occur at crack sizes less than 100  $\mu\text{m}$ . In fact, cracks were found to initiate at sites of micro-porosity of  $\sim 10 \mu\text{m}$  diameter in powder metallurgy IN100. It was also felt that fatigue cycles required to propagate a crack from 10  $\mu\text{m}$  to 100  $\mu\text{m}$  would constitute a significant contribution to the fatigue life of a component. Consequently, it became desirable to initiate cracks from smaller artificially introduced defects.

A pulsed laser was employed to introduce surface defects in fatigue test specimens to serve as initiation sites for small cracks. The principal advantage of this technique is that small sizes are obtainable. The laser used was a Quanta Ray, ND-YAG laser operating in the Q-switched mode with a wavelength of 532 nm. The incident beam diameter is  $\sim 3 \text{ mm}$

with an output energy of around  $10^{-3}$  Joules/pulse and a pulse duration of  $0.2 \mu \text{ sec}$ . The incident beam is focused by a series of two cylindrical lenses which generates an elliptical defect in the specimen surface as shown in Figure 2.7b from 100 to 500 pulses are used for each defect. The depth of each defect is determined by the number of pulses and the intensity of radiation in the incident beam. Similar defects have also been made using a spherical lens and translating the specimen with respect to the focal point to achieve the desired surface length. The disadvantage of this technique is the difficulty encountered in controlling the depth of the defect. This was due to the nonuniform spatial distribution of intensity in the incident beam and changes in the beam characteristics between each use of the laser.

#### 2.4.3 Crack Initiation from $\text{Al}_2\text{O}_3$ Particles

The René 95 used in this investigation was intentionally seeded with  $\text{Al}_2\text{O}_3$  particles with an average diameter of  $114 \mu\text{m}$ . The oxide particles were mixed at a ratio of 20,000 particles of  $\text{Al}_2\text{O}_3$  per pound of alloy. Fatigue crack initiation generally occurs where an  $\text{Al}_2\text{O}_3$  particle intersects the surface of the specimen gauge section as shown in Figure 2.8a.

#### 2.4.4. Precracking

In nearly all experiments where artificial defects were used, cracks were initiated by precracking at  $R = -1$  and a stress range of approximately  $\pm 520 \text{ MPa}$ . Precracking required from 20 K to 50 K cycles. Precracking was found to be necessary because:

- 1) Negative R-ratios promote crack initiation.
- 2) It was necessary to initiate and propagate cracks at least  $10\text{-}20 \mu\text{m}$  to grow out of the local influence of the defect.

- 3) It was intended that cracks should assume a stable crack front geometry before surface crack length measurements would correlate with crack depth.

## 2.5 Crack Length Measurement by Plastic Replica

The plastic replica technique was used to measure crack lengths in room temperature and elevated temperature tests. This technique has a resolution of about 1  $\mu\text{m}$  in crack length. In addition, it serves as a valuable record which can later be used to correlate crack growth rates with crack tip-microstructural interactions. Acetyl cellulose tape of 125  $\mu\text{m}$  thickness was used as the replicating material and acetone or methyl acetate as the solvent.

The replicating procedure was as follows:

- 1) Cyclic loading was stopped at zero load after a preset number of cycles.
- 2) Induction heating was automatically turned off in elevated temperature tests.
- 3) The specimen was loaded in tension to 50-80% of the peak cyclic load. This static load was decreased as the cracks became longer.
- 4) The softened side (with a few drops of solvent) of a piece of replicating film was applied to the specimen surface under a light pressure for about 15 seconds.
- 5) The film was allowed to dry for 10 minutes.
- 6) The film was peeled off and taped to a glass microscope slide with the replica facing up.
- 7) The replica was then viewed under a reflected light microscope at magnifications ranging from 50x to 500x.

8) Crack lengths were measured using a calibrated eyepiece micrometer.

## 2.6 Crack Length Measurement by A. C. Potential Drop

Due to the considerable labor involved in monitoring crack length by replication, especially at elevated temperature, a program was undertaken to develop an A. C. Potential Drop system for the continuous and automated measurement of crack length. A resolution of  $\sim 2 \mu\text{m}$  in crack length was achieved. Unfortunately, a significant problem was encountered in the long term stability of the system. Consequently, work proceeded using the plastic replication technique for measuring crack length.

The A. C. Potential Drop system is described and discussed in Appendix A.

## 2.7 Small Crack Growth Testing at Room Temperature

The fatigue tests for small cracks were carried out for Inconel X-750, PM René 95 and Waspaloy on a servo-hydraulic machine under load control at room temperature, in lab air and at a frequency of 20 Hz. The test conditions for small crack growth in Inconel X-750, René 95 (PM) and Waspaloy is shown in Table 2.5. The load ratios selected were -1, 0.05, and 0.5. The maximum stresses for different tests varied from 331 MPa (48 Ksi) to 758 MPa (110 Ksi). Initial crack lengths ranged from  $6 \mu\text{m}$  to  $200 \mu\text{m}$ . To measure crack lengths the tests were interrupted at regular intervals and replicas were taken of both faces of the specimen at 80% of maximum load.

The investigations of the threshold behavior of small cracks were conducted only for Inconel X-750. The threshold stress ranges for small cracks at a given R ratio and a given crack length were determined by increasing stress range by about 3% every 500,000 cycles if the growth rate was  $\leq 10^{-11}$  m/cycle.

The polished specimen surfaces were etched by Kalling's solution (100 ml HCl + 100 ml ethanol + 5 gm  $\text{CuCl}_2$ ) or modified Kalling's solution (100 ml  $\text{H}_2\text{O}$  + 200 ml

methanol + 100 ml HCl + 7 gm  $\text{FeCl}_3$  + 2 gm  $\text{CuCl}_2$ ). Etched specimen surfaces were observed under optical microscopy to reveal the microstructure, the morphology of defects, small crack path and associated slip bands, and the relationship between the microstructures and the cracks.

The fracture surfaces of small cracks were opened up by breaking the specimens after making a saw slot along the small crack plane. They were then examined by scanning electron microscopy (SEM) to reveal fracture surface features.

## 2.8 Small Crack Growth Testing at Elevated Temperature

Test specimens were prepared in the manner described in previous sections. Three defects were introduced at orthogonal positions in the midplane of round gauge section specimens. Two defects were introduced on opposite faces of round-with-flats gauge section specimens. Testing was performed on a closed-loop, servo-hydraulic testing machine. Water cooled grips were aligned on axis to within  $\pm 15 \mu\text{m}$  before every test. This tolerance is less than the lateral play in the actuator.

Specimens were heated by a 2.5 kilowatt - 400 kilohertz induction heating unit using an eight-turn, axi-symmetric induction coil. The temperature in the plane of the crack was maintained at the desired test temperature within  $\pm 1^\circ \text{C}$ . The temperature gradient along the gauge length was less than  $\pm 5^\circ \text{C}$  as determined by a system calibration.

The test conditions for small crack growth in Waspaloy, Inconel 718 and IN100 (PM) are shown in Table 2.6.

### Load Controlled Testing

Load controlled tests were performed at 20 cpm or 10 cpm using a sinusoidal waveform. Cycling was stopped at zero load and induction heating turned off



automatically at preset cycle intervals. After the specimen cooled to room temperature, crack lengths were measured by replication. Tests were terminated when the largest surface crack length was in the 2-3 mm range. Specimens were separated along the crack plane by continuing to cycle at room temperature and a positive stress ratio.

The principal test variables were maximum stress and R-ratio, (minimum stress/maximum stress). The stress was calculated as the engineering stress,  $P/A_0$ .

#### Strain Controlled Testing

Strain (displacement) controlled tests were performed at 10 cpm using a sawtooth waveform. Longitudinal displacement was measured on specimen gauge sections to achieve total strain control. The effective gauge length between extensometer probes was 14.4 mm. Total strain,  $\epsilon_T$ , was measured and controlled to a precision of  $\pm 0.01\%$ .

At the end of each cycle interval; cycling was automatically stopped at zero strain, hydraulic pressure turned off returning to zero load along an elastic path and the induction heating turned off. After the specimen cooled to room temperature, the extensometer was removed and crack lengths were measured by replication. When elastic-plastic cycling occurred, care was taken to return the extensometer and the strain-load value to the appropriate position on the hysteresis loop. Tests were terminated in the same manner employed in load controlled tests.

Total strain ranges were chosen to be relevant to notch locations in turbine disks.

Table 2.2  
Chemical Composition (Normal, Weight %)

Material	Ni	Cr	Co	Mo	W	Cb + Ta	Al	Ti	Fe	Mn	Si	C	B	Zr	Cu
Inconel X-750	73.0	15.0	-	-	-	0.9	0.8	2.5	6.8	0.70	0.30	0.04	-	-	-
Waspaloy	58.3	19.5	13.5	4.3	-	-	1.3	3.0	-	-	-	0.08	0.006	0.06	-
Inconel 718	53.8	18.0	0.28	3.01	-	5.23	0.62	0.94	17.6	0.13	0.18	0.04	0.012	-	0.16
René 95 (PM)	61.3	14.0	8.0	3.5	3.5	3.5	3.5	2.5	-	-	-	0.15	0.010	0.05	-
IN100 (PM)*	55.4	12.4	18.5	3.2	0.025	0.02	4.98	4.33	0.15	0.01	0.005	0.07	0.020	0.060	0.035

\* Represents the average of maximum and minimum specified values.

Table 2.2  
Heat Treatment Conditions

Material	Heat Treatment		Grain Size ( $\mu\text{m}$ )
Inconel X-750	1150° C x 4 hrs. +AC	850° C x 24 hrs. +AC	700° C x 20 hrs. +AC 130
Waspaloy	1080° C x 4 hrs. + quench in oil or water	845° C x 4 hrs. +AC	760° C x 16 hrs. +AC 200 & 7
Inconel 718	955° C x 1 hr. +AC	720° C x 8 hrs. FC to 620° C @ 56° C/hr.	620° C x 8 hrs. +AC 5 to 500
René 95 (PM)	1107° C + 25 sec. delay in air + OQ		760° C x 8 hrs. +AC 5
IN100 (PM)	1121° C x 2 hrs. + OQ		871° C x 40 min. + AC < 371° C 982° C x 45 min. + AC 649° C x 24 hr. + AC 760° C x 4 hr. + AC 3 to 5
AC FC OQ	air cool furnace cool oil quench		

Table 2.4  
Mechanical Properties

Material	Temp (°C)	E (GPa)	$\sigma_{0.2\%}$ (MPa)	$\sigma_{UTS}$ (MPa)	Elog. (%)
Inconel X-750	25	214	610	1000	30
Waspaloy	25 538	206	903 949	1324 1251	24 31
Inconel 718	25 427	204 183	1131 1100	1340 1250	23 47
René 95 (PM)	25	214	1240	1650	16.6
IN100 (PM)	649	179	1100	1380	22

Table 2.5  
Small Crack Fatigue Tests at Room Temperature

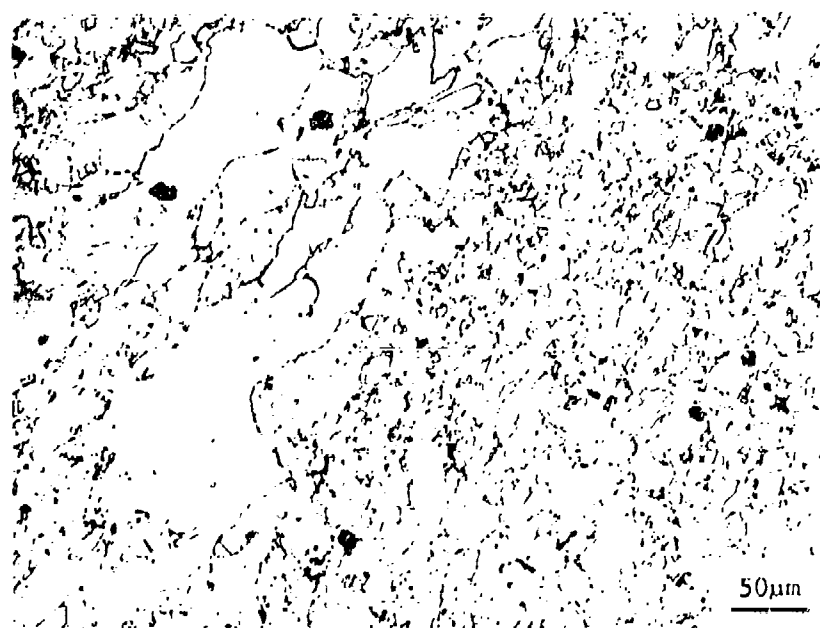
Test Number	Material	R-ratio	$\sigma_{max}$ (MPa)	Number of Cracks
JF1	X-750	-1	424	4
JF2	X-750	-1	350	2
JF3	X-750	-1	331	6
JF4	X-750	0.05	515	1
JF5	X-750	0.05	456	6
JF6	X-750	varied	483	3
JF7	Waspaloy	-1	483	10
JF8	Waspaloy	-1	758	10
JF9	Waspaloy	0	758	10
JF10	Waspaloy	-1	621	7
JF11	Waspaloy	-1	345	6
JF12	Waspaloy	-1	758	3
JF13	Waspaloy	0	483	4
JF14	René 95 (PM)	-1	483	2
JF15	René 95 (PM)	-1	758	13
JF16	René 95 (PM)	0	758	4
JF17	René 95 (PM)	0.5	758	3

Table 2.6  
Small Crack Fatigue Tests at Elevated Temperature

Test Number	Material	Temp (°C)	R-ratio	$\sigma_{max}$ (MPa)	Number of Cracks
GR1	Waspaloy	427	-1	483	2
GR2	Waspaloy	427	-1	758	3
GR3	Waspaloy	427	0	758	1
GR4	Waspaloy	427	-1	621	3
GR5	Waspaloy	427	0.3	758	2
GR6	Waspaloy	427	0.5	896	3
GR0	Waspaloy	427	0.05	621	2
GR7	Inconel 718	427	-1	758	2
GR8	Inconel 718	427	0.05	758	2
GR9	Inconel 718	427	-1	621	2
GR16	IN 100 (PM)	649	0.1	785	2
$\epsilon$ - control			$\epsilon_{min.}$	$\epsilon_{max.}$	
GR14	IN 100 (PM)	649	-0.55%	0.55%	2
GR17	IN 100 (PM)	649	0	0.80%	2



(a)



(b)

Figure 2.1 Typical microstructures for: a) Inconel X-750 and b) Waspaloy used in this investigation.

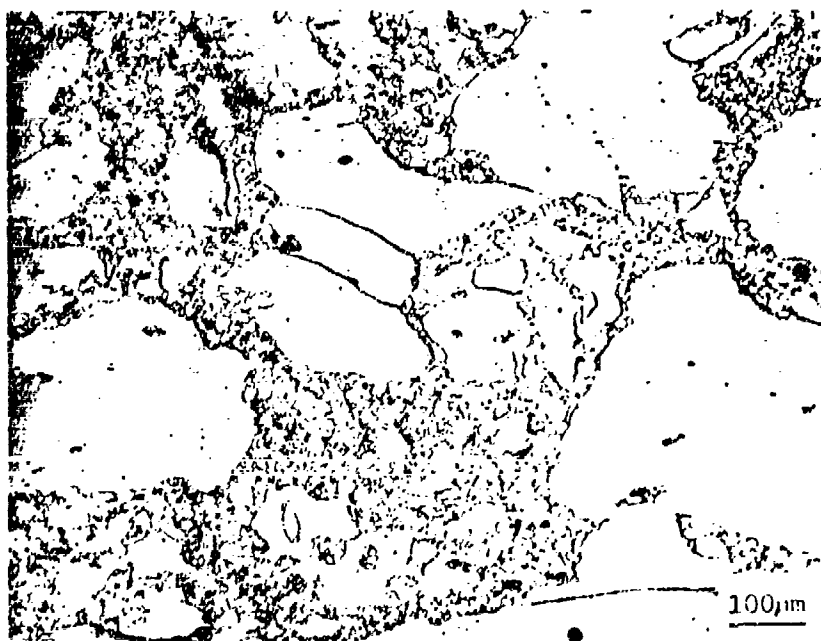
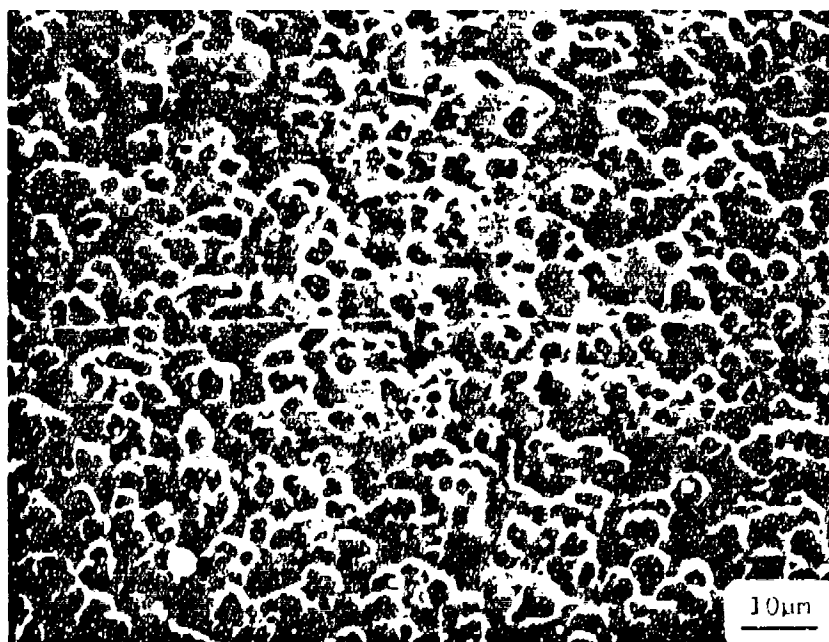
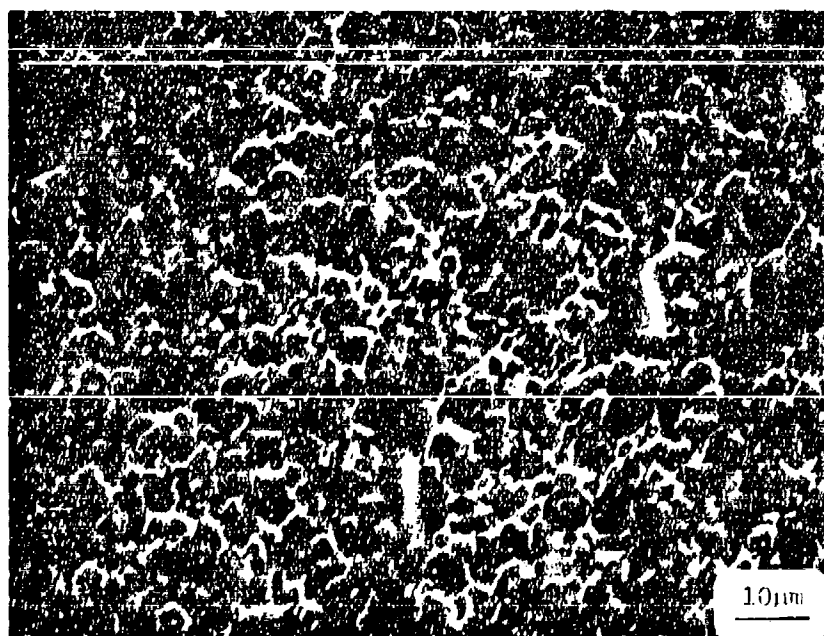


Figure 2.2 Typical microstructure for Inconel 718 used in this investigation.



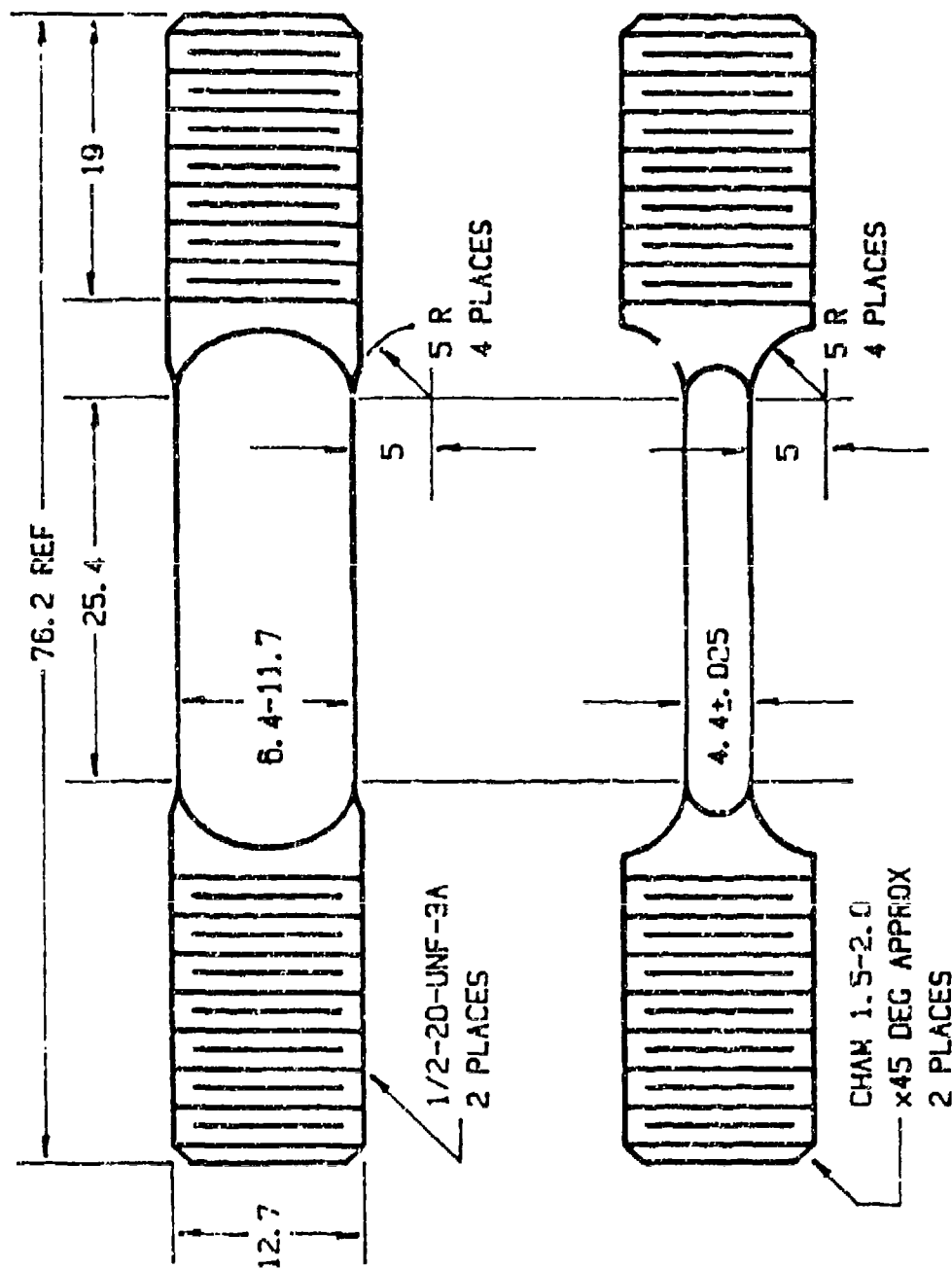


(a)



(b)

Figure 2.3 Typical microstructures for: a) powder metallurgy René 95 and b) powder metallurgy IN100.



Dimensions in mm.

Figure 2.4 Specimen geometry used for room temperature tests.

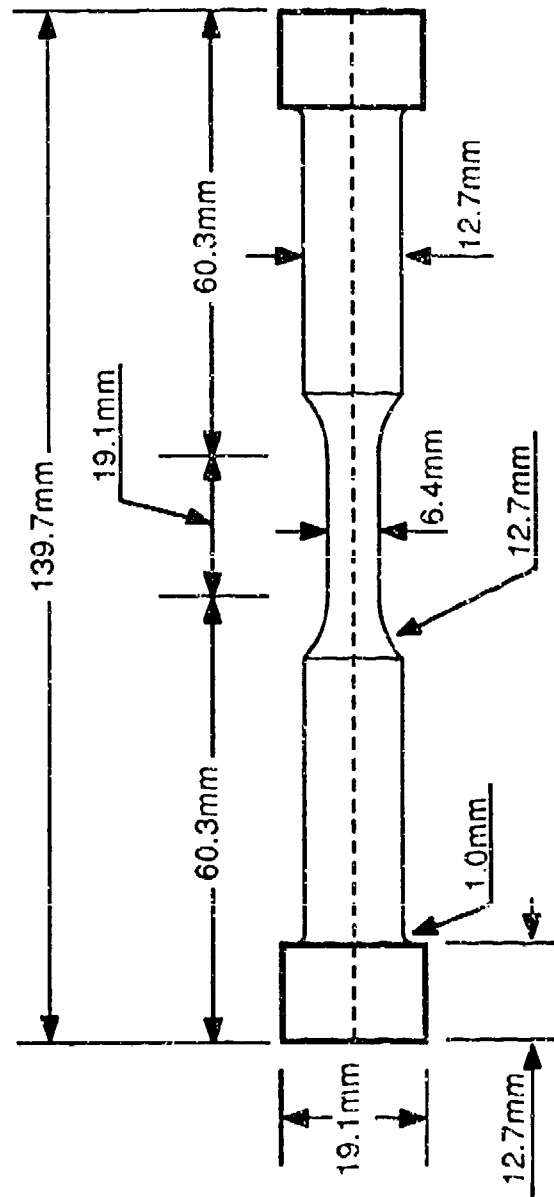


Figure 2.5 Specimen geometry used for elevated temperature tests.

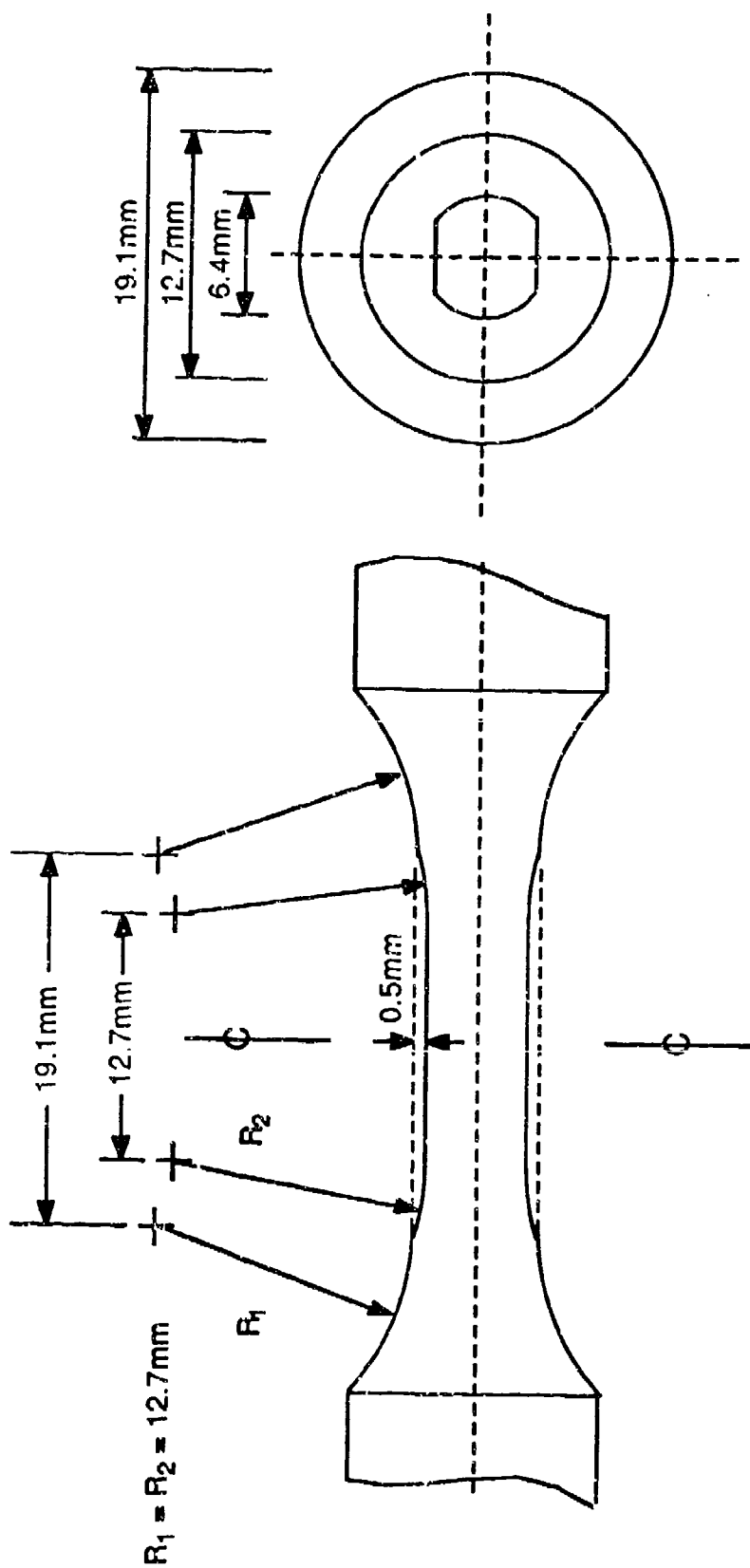
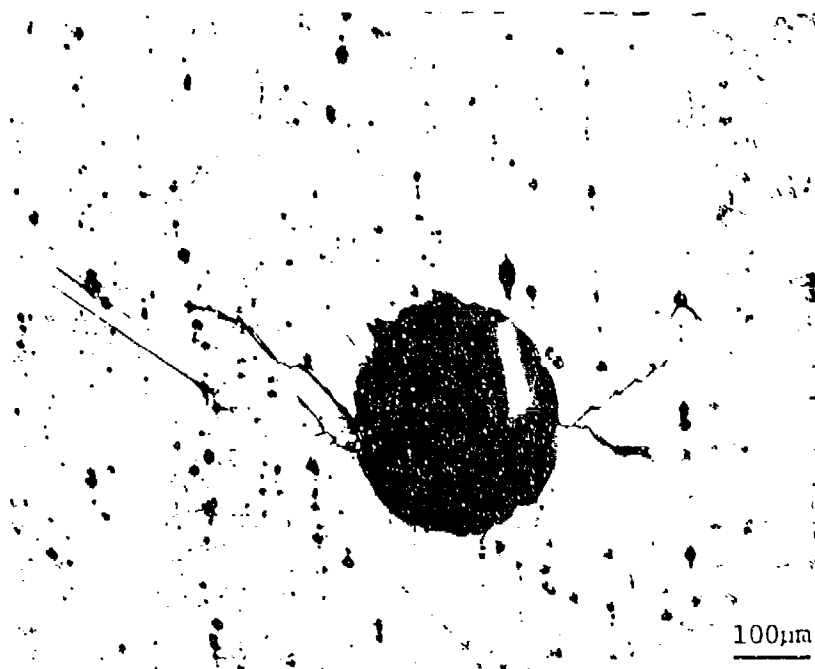
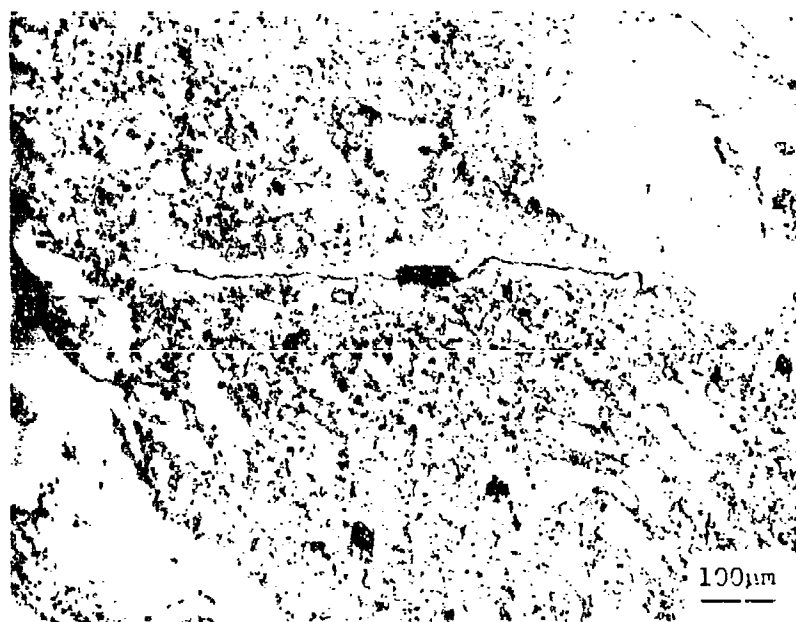


Figure 2.6 Modification to specimen gauge section, shown in Figure 2.5, used for elevated temperature tests.

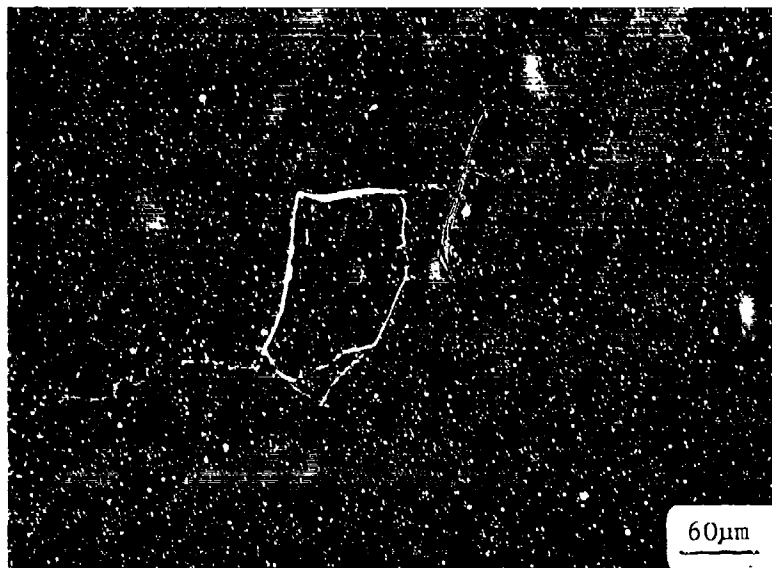


(a)



(b)

Figure 2.7 a) A typical EDM defect and fatigue crack shown here in the surface of Inconel X-750.  
b) A typical laser defect and fatigue crack shown here in the surface of Waspaloy.



(a)



(b)

Figure 2.8 a) Fatigue crack initiation at an  $\text{Al}_2\text{O}_3$  particle in powder metallurgy René 95.  
b) Fatigue crack initiation at PSB's in Waspaloy tested at room temperature.

### 3. DATA ANALYSIS

The raw data taken from each fatigue experiment was surface crack length,  $2c$ , and cycle number,  $N$ . The desired presentation of the data is crack depth,  $a$ , versus  $N$  and crack growth rate,  $da/dN$ , versus stress intensity factor range,  $\Delta K$ . This requires a determination of crack size and shape.

Elevated temperature fatigue experiments were terminated when one or more cracks had achieved a surface crack length of approximately 2 mm. At room temperature, fatigue loading was continued at a positive stress ratio, but reduced stress amplitude, until specimen separation occurred. The shape of the subject cracks at the termination of high temperature testing was then evident on the fracture surface as a result of heat tinting. Figure 3.1 shows several fracture surfaces with crack front profiles readily distinguished by the presence of oxidation.

Cracks of different sizes are present in the same specimen due to the variability in the number of cycles required for initiation from the artificial defects. In some cases, one or more cracks may have arrested. Careful measurements of surface crack length and crack depth were made from these and other photographs. These values are shown graphically in Figure 3.2 where  $c/a$  is plotted against  $c$  for a number of tests under different conditions. A  $c/a$  ratio of  $\sim 1$  is the predominant value over the full range of crack sizes considered and for the variety of testing conditions employed. Any variation from  $c/a = 1$  cannot be systematically related to testing conditions. Hence, all subsequent data reduction will be performed by first taking the crack depth,  $a$ , to be equal to half the surface length  $c$ . The  $c/a$  ratio was taken to be equal to one for room temperature experiments as well.

Each fatigue experiment yielded from 7 to  $\sim 30$  data points. These  $N_i, a_i$  pairs were tabulated and first plotted as  $a_i$  vs.  $N_i$ . The data was edited for potential measurement

errors. If a data point appeared to fall erroneously out of place, the replica was measured again.

Values of  $a$  were compared to artificial defect size and shape on the fracture surface. Data pairs were considered to be valid only after the crack assumed a semicircular shape encompassing the defect. For this reason some of the first  $N_i, a_i$  pairs may have been rejected.

### 3.1 Computation of Crack Growth Rates

The determination of  $da/dN$  from  $a$  versus  $N$  was accomplished using two well established data processing techniques; the secant method and the incremental polynomial technique.

In some  $a$  versus  $N$  curves, it was obvious that considerable variability existed in crack growth rate. This was usually attributed to the interaction of short cracks with variable resistance in the microstructure. The secant or point-to-point technique was frequently employed when depicting this variability. The secant method is simply a calculation of the slope of a straight line which connects two adjacent data points on the  $a$  versus  $N$  curve. The crack growth rate may be calculate as:

$$\frac{da}{dN} = \frac{a_{i+1} - a_i}{N_{i+1} - N_i} \quad (3.1)$$

The stress intensity factor range associated with this crack growth rate was calculated using the average crack length where  $a_m = (a_{i+1} + a_i)/2$ . The principal disadvantage of the secant method is that the variability calculated for  $da/dN$  often includes a significant component which can be attributed to error in the measurement of crack length.



The bulk of the crack growth rate data was processed using the 7 point-incremental polynomial technique. This technique "smooths out" the crack growth rate curve and minimizes the influence of measurement error on  $da/dN$  by fitting the  $a$  versus  $N$  curve locally in increments. This technique involves fitting a parabola to successive 7-point subsets of the data using a "least squares" procedure. To determine  $da/dN$  at point  $i$ , the equation of a parabola was determined for data points  $N_{i-3}$ ,  $a_{i-3}$  through  $N_{i+3}$ ,  $a_{i+3}$ . The slope at point  $i$  is simply the first derivative of the equation of the parabola. In view of the limited number of data points for each experiment, the slope at the first and last three points was determined using the first and last fitted parabolas [7].

### 3.2 Stress Intensity Factor Calculations

The essence of the short crack problem in fatigue is the inability of the stress intensity factor,  $K$ , based on linear elastic fracture mechanics, to consolidate crack growth rate data at very small crack sizes in some materials. The anomalous behavior of short cracks is generally characterized in terms of  $da/dN$  versus  $\Delta K$ . The breakdown of LEFM for short cracks is attributed to a lack of similitude between short and long cracks. In some cases, the apparent deviation from long crack behavior may be attributed to an inappropriate determination of the effective stress intensity factor range,  $\Delta K_{eff}$ . This may be due to an inaccurate characterization of crack geometry, failure to account for crack closure, or an incorrect assessment of the stress intensity factor.

The stress intensity factor solution employed in this investigation was that for a semi-elliptical surface crack.

Irwin [8] developed an expression for the mode I stress intensity factor around an elliptical crack embedded in an infinite elastic solid subjected to uniform tension. The most general formulation is given by

$$K_I = \sigma \sqrt{\pi a} \frac{[\sin^2 \phi + (a^2/c^2) \cos^2 \phi]^{1/4}}{\phi} \quad (3.2)$$

where  $\phi$  is an elliptical integral of the second kind and is given by

$$\phi = \int_0^{\pi/2} \left[ 1 - \frac{(c^2 - a^2)}{c^2} \sin^2 \phi \right]^{1/2} d\phi \quad (3.3)$$

The symbols  $a$ ,  $c$  and  $\phi$  are defined in Figure 3.3a. As discussed in a previous section, the  $c/a$  ratio was found to be approximately one and constant over the full range of crack sizes considered. By substituting  $c = a$ , the above expression for stress intensity simplifies to

$$K = \frac{2}{\pi} \sigma \sqrt{\pi a} = 0.637 \sigma \sqrt{\pi a} \quad (3.4)$$

This expression was first developed by Sneddon [9] and is valid for all values of  $\phi$  when  $c = a$ , that is for a circular internal crack of radius  $a$  (penny-shaped crack) embedded in an infinite solid.

The stress intensity factor for surface cracks in finite elastic bodies (laboratory specimens) may be expressed in terms of a boundary correction factor modification to the stress intensity factor for cracks in infinite bodies. The most general formulation is given by

$$K = \sigma \sqrt{\pi a} \frac{[\sin^2 \phi + (a^2/c^2) \cos^2 \phi]^{1/4}}{\phi} F(a/t, a/c, c/W, \phi) \quad (3.5)$$

The boundary correction terms are defined in Figure 3.3b.

Newman [10] has reviewed a significant number of boundary correction factors for surface cracks. For the case of the semicircular surface crack ( $a/c = 1$ ) and  $a/t < 0.2$ , the maximum value of  $F$  occurs at or near the intersection of the crack with the specimen surface ( $\phi = 0$ ) where  $F \approx 1.15$ . Hence, the maximum value of the mode I stress intensity factor for small semicircular surface cracks may be approximated by

$$K = \frac{(1.15) 2\sigma \sqrt{\pi a}}{\pi} = 0.73 \sigma \sqrt{\pi a}. \quad (3.6)$$

This expression was used for all data analysis in this investigation.

The specimen geometry employed in room temperature tests, shown in Figure 2.4, was of rectangular cross section similar to Figure 3.3b. A boundary correction factor of 1.15 is the appropriate estimate for this geometry and the range of  $a/t$  covered in all tests. Usually  $a/t$  was less than 0.2.

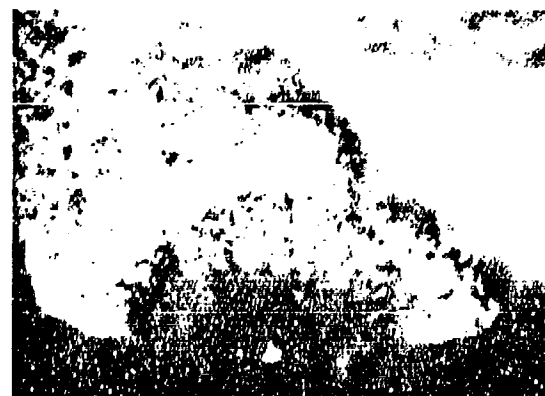
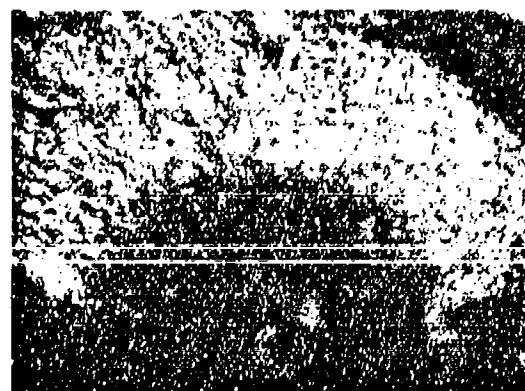
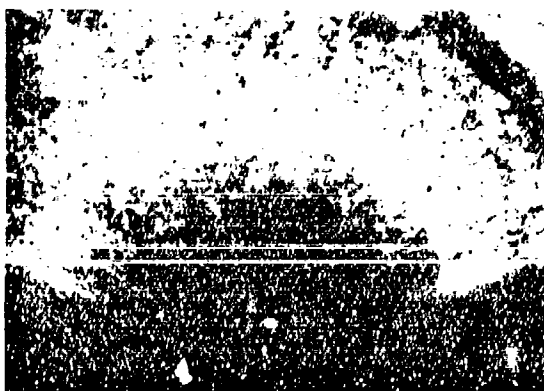
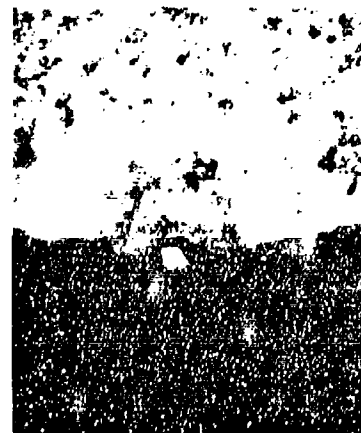
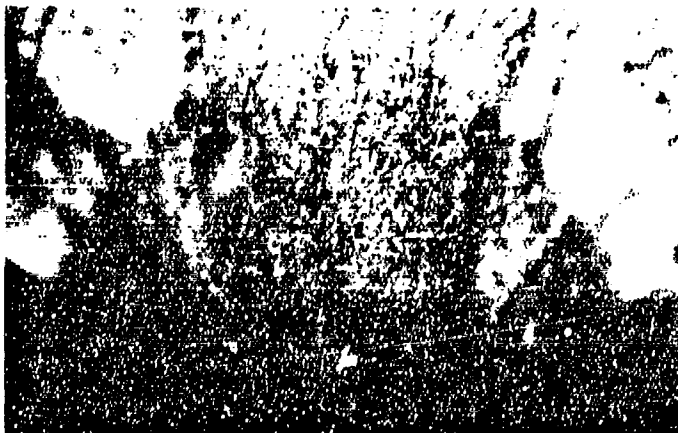
The specimen geometry employed in many elevated temperature tests, shown in Figure 2.5, has a cylindrical gauge section. Nisitani and Chen [11] have calculated stress intensity factors for semi-elliptical surface cracks in cylindrical rods by modifying the solution for elliptical surface cracks in finite plates, Eq. 3.6. They have calculated this correction factor to be equal one when  $c/a = 1$  and  $a/r$  is less than 0.2 which was the case in the elevated temperature test specimens.

Raju and Newman [12] calculated stress intensity factors for semi-elliptical flaws in cylindrical rods using a three dimensional finite element method. The results were presented in terms of  $K/\sigma \sqrt{\pi a Q}$  versus  $\phi$ . When  $c/a = 1$ ,  $Q = (\pi/2)^2$  and  $a/D \leq 0.2$ , therefore,  $K/\sigma \sqrt{\pi a/Q} = 1.15$  which is the boundary correction factor for the cylindrical specimen.

The stress intensity factor range was calculated using only the positive portion of the loading cycle. These tests were not instrumented for the measurement of crack opening/closure stresses, therefore, the stress range,  $\Delta\sigma$ , was taken as  $\sigma_{\max}$  when  $\sigma_{\min} \leq 0$  and as  $(\sigma_{\max} - \sigma_{\min})$  when  $\sigma_{\min} > 0$ . Cracks grew nominally perpendicular to the applied stress. Crack lengths were taken as their projected lengths. Hence, for the specimen and crack geometries considered in this investigation, the nominal stress intensity factor range was calculated according to

$$\Delta K = 0.73 \Delta\sigma \sqrt{\pi a} \quad (3.7)$$

It is important not to underestimate  $\Delta K$  for small cracks because it could yield crack growth rates that are apparently higher than the true values when compared at a given  $\Delta K$ .



Mag = 30X

Figure 3.1 Crack front profiles as evidenced by the presence of oxidation on the fracture surfaces of Waspaloy specimens tested at 427° C.

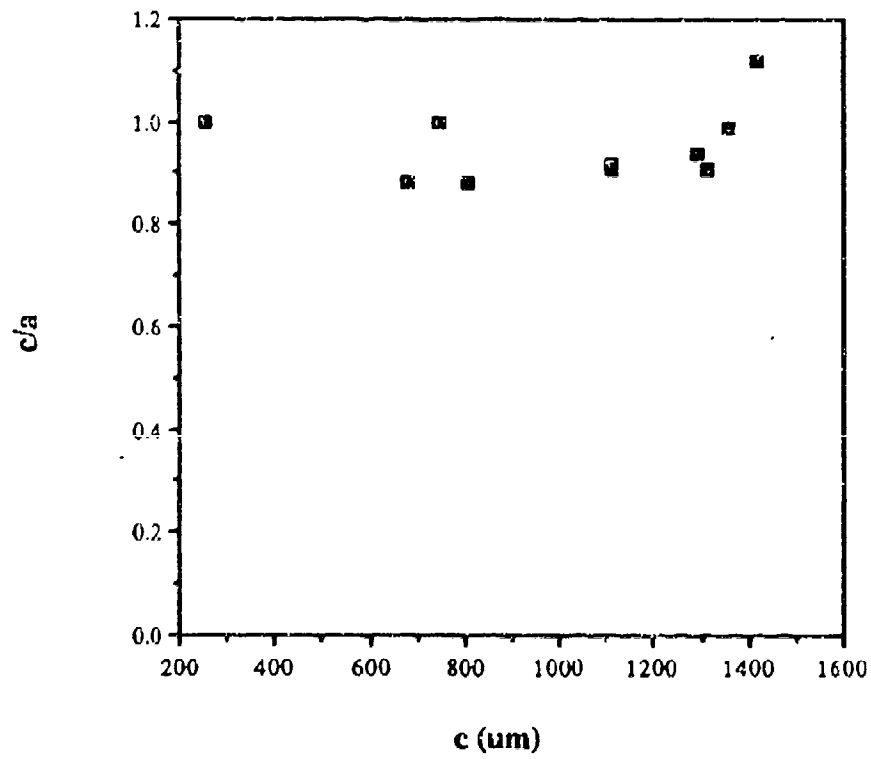
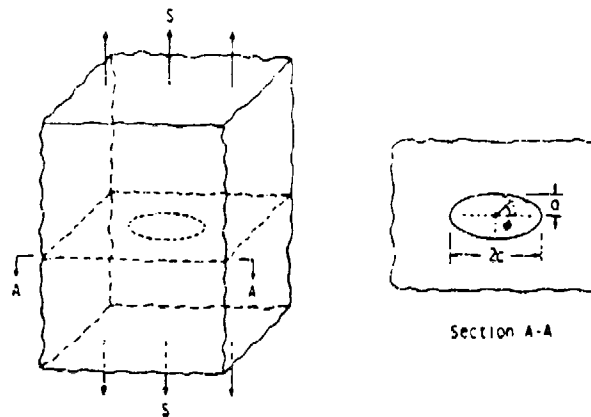
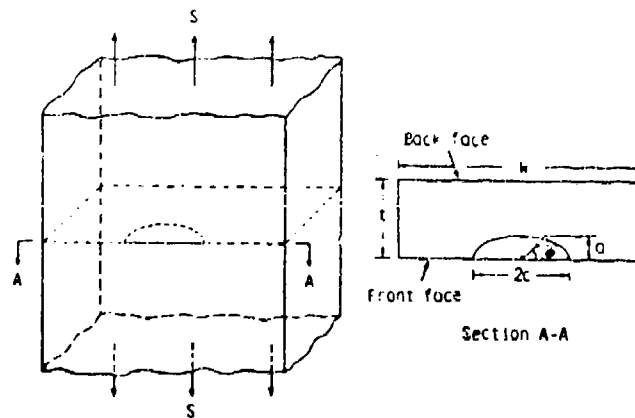


Figure 3.2 The aspect ratio,  $c/a$  versus  $c$  for numerous cracks in Waspaloy tested at 427C under several stress ranges



(a)



(b)

Figure 3.3 a) Elliptical crack embedded in an infinite solid subjected to a uniform stress.  
 b) Surface crack in a finite plate subjected to a uniform stress (from Ref. 10).

## 4. RESULTS AND DISCUSSION

### 4.1. Fatigue Behavior of Small Cracks at Room Temperature

#### 4.1.1 Inconel X-750

The variation of threshold stress range with semicrack length for Inconel X-750 at  $R=0.05$  is shown in Figure 4.1, in which  $a_0$  is the intrinsic crack length and  $\sigma_s$  is the fatigue limit. The corresponding plot of threshold  $K$  vs. semicrack length is shown in Figure 4.2. It is found that when the crack is long the data points approach the line representing the long crack threshold values. At small crack lengths these data points deviate from the long crack line at some critical point, with the threshold stress approaching the fatigue limit of the alloy and with the threshold stress intensity factor approaching zero. This threshold behavior of small cracks has been observed by other investigators [13, 14].

The breakdown of LEFM for small surface cracks gives one explanation for the unusual small crack threshold behavior. The lower plastic constraint for a small crack near the free surface provides a condition of extensive plastic flow. This factor combined with a high applied stress (near yield stress) for small cracks results in a high ratio of  $r_p / a$ . The stress and strain fields at the crack tip thus can best be described by EPFM due to the rather large plastic zone at the crack tip. As an alternative approach, an effective crack length which contains part of the plastic zone was proposed to substitute for the actual crack length in the calculation of  $K$  in order to get a better description of the stress field at a small crack tip. The effective crack length contains an extra term in addition to the actual crack length. The extra term is called "intrinsic crack length ( $a_0$ )", which is directly related to the plastic zone size. When the crack is very long, the effective crack length is almost the same as the actual crack length, then the crack behavior follows LEFM. But when the crack length approaches zero, the effective crack length approaches the intrinsic length  $a_0$ , then the small crack behavior appears as shown in Figures 4.1 and 4.2.



Grain boundaries play a critical role in the threshold behavior of small cracks since grain boundaries give large constraint to the plastic flow at the tip of a small crack. The grain size provides a limit to the plastic zone size at the crack tip and thus a limit to the intrinsic crack length  $a_0$ . It then can be inferred that the smaller the grain size, the smaller the intrinsic crack length and the less is the extent of small crack behavior. This inference has been confirmed by experimental observations [15, 16].

Another important factor which affects the threshold behavior of small cracks is the crack closure effect. As described in [17-23] small cracks have less closure than long cracks. This fact results in the much higher effective  $\Delta K$  for small cracks than for long cracks, which decreases the nominal threshold  $\Delta K$  of small cracks (Figure 4.2).

Figure 4.3 shows the variation of maximum and minimum values of threshold stress intensity factor of small cracks with the load ratio  $R$  in Inconel X-750, with cracks having almost the same length ( $\sim 110 \mu\text{m}$ ). The data can also be plotted as  $\Delta K_{th}$  vs  $R$ , shown in Figure 4.4 where  $\Delta K_{th}$  is only the positive part when  $R < 0$ .

It is found that the maximum value of the threshold stress intensity factor  $K_{max}$  increases with increasing  $R$  (Figure 4.3).  $\Delta K_{th}$  is the highest at  $R = 0$  and the lowest at  $R = 0.5$  (Figure 4.4). The relation shown in Figure 4.4 was expressed by Klesnil and Lukas' equation if  $\Delta K_{th}$  is now taken as the whole SIF range [24].

$$\Delta K_{th} (\text{MPa } \sqrt{\text{m}}) = 7.236 (1-R)^\gamma \quad (4.1)$$

or in other forms:

$$\Delta K_{th}/7.236 = (1 - R)^\gamma \quad (4.2)$$

$$K_{th}^{max}/7.236 = (1 - R)^{\gamma-1} \quad (4.3)$$

$$\text{where } \gamma = 0.956 \quad R \geq 0$$

$$\gamma = 0.514 \quad R < 0$$

Equation (4.1) can also be transformed into Walker's equation [25]:

$$\Delta K_{\text{eff}} = K_{\text{th}}^{\text{max}} (1-R)^p \quad (4.4)$$

$$\text{where } p = 0.044 \quad R \geq 0$$

$$p = 0.486 \quad R < 0$$

Crack closure plays a critical role in the effect of  $R$  on the threshold value of small cracks. Elber [22] proposed the following equation to show the variation of closure parameter  $U$  with  $R$  in aluminum alloy:

$$U = 0.5 + 0.4 R \quad (4.5)$$

$$\text{where } U = \Delta K_{\text{eff}} / \Delta K$$

Similar relations were also found by other investigators [26, 27].

Equation 4.5 implies that closure decreases with increasing  $R$ . Although Equation 4.5 is for plastic-induced closure, there is the same tendency for variation of  $U$  with  $R$  for roughness-induced closure [28]. If a constant effective  $\Delta K_{\text{th}}$  is assumed through all  $R$  ratios, it is not surprising that when  $R$  increases, the nominal  $\Delta K_{\text{th}}$  will decrease due to the decrease of crack closure, as shown in Figure 4.4. A further examination of the  $R$  effect reveals some discrepancies between the  $R$  effect and its closure explanation. For instance, when  $R$  is high enough (say  $R = 0.5$ ) the closure effect almost disappears,  $\Delta K_{\text{th}}$  is supposed to be constant (equal to effective  $\Delta K_{\text{th}}$ ) as  $R$  continues to increase according to the closure model, but the threshold values of  $\Delta K$  have been found still to decrease with increasing  $R$  ratio [29]. The other possible reason for  $R$  ratio effect may be the mode II component and compression. For a small fatigue crack with a zig-zag path, as a tension load is applied to the specimen, both mode I and mode II mechanisms operate. As a compressive load is applied to the specimen only mode II contributes to the driving force

for the crack growth. The compression and mode II effect were not taken into account in closure explanations [21].

The crack growth rates computed from "a vs N" curves by polynomial regression were plotted as a function of the stress intensity factor range  $\Delta K$  for  $R = -1, 0.05, 0.5$  respectively in Figures 4.5 - 4.7, where  $\Delta K$  was calculated by Eq. 3.7. The effect of EDM pits on initial K values was accounted for with Bowie's correction [30, 31]. All the crack growth data for different R ratio ( -1, 0.05, 0.5 ) are then plotted together as a function of  $\Delta K$  in Figure 4.8 in order to compare the effect of different load ratios on crack growth rates. The long crack data of  $R = 0.5$  and  $R = -1$  are calculated by Walker's equation (4.4) based on long crack data for  $R = 0.05$  after reference [32].

It is found that the growth rates of small cracks are much higher than those predicted for long cracks at the same  $\Delta K$  for all three different R ratios (Figures 4.5 - 4.7). The transition points from typical small crack region to long crack behavior are around a length of 400 $\mu\text{m}$  to 600 $\mu\text{m}$  in Inconel X-750. This length is about 3-5 times the grain size. It is also very interesting to note that some very small cracks with a length less than the grain size had higher growth rates than longer small cracks (Figure 4.5).

The higher growth rates come from the EPFM nature of small cracks due to the high ratio of  $r_p/a$ . From the point of view of modified LEFM, a high ratio of  $r_p/a$  provides a larger effective driving force  $\Delta K_e = Y \Delta \sigma \sqrt{\pi (a + r_p/2)}$ . Alternatively, according to EPFM, the high ratio  $r_p/a$  results in a larger crack tip opening displacement (CTOD) (see Dugdale model). For a growing small crack, when its plastic zone size is smaller than the grain size, it behaves like in a single crystal with less plastic constraint and thus a high ratio  $r_p/a$ . After its plastic zone size exceeds the grain size, more plastic constraint leads to a lower ratio  $r_p/a$ . The transition plastic zone size ( $r_p = d$ ) corresponds to a semicrack length of 4-5 times the grain size [33, 34, 35, 36].

From the above discussion it is clear that the  $\Delta K$  values based on LEFM can not be taken as a general parameter to rationalize all small crack data. A new parameter based on EPFM should be proposed to better characterize the crack driving force for small cracks.

Figure 4.8 shows the inability of  $\Delta K$  to rationalize the  $R$  ratio effect for both small cracks and long cracks. To solve this problem, the effective stress intensity factor range,  $\Delta K_{\text{eff}} = K_{\text{max}} - K_{\text{op}}$ , has been used instead of  $\Delta K$  in the plots of  $da/dN$  vs SIF. The use of  $\Delta K_{\text{eff}}$  works in general, but it fails to correlate the data at negative  $R$  ratios. This suggests that other factors such as the mode II component or other criteria must be looked at.

#### 4.1.2 Waspaloy

A comparison of fatigue behavior for different stresses at  $R = -1$  and for different  $R$  ratios at  $\sigma_{\text{max}} = 758$  MPa are shown in Figures 4.9 and 4.10. This data is similar to the data of Rene' 95.

Figures 4.11 - 4.13 show the crack growth rates versus the stress intensity factor range for different  $R$  ratios and different stress levels. It is found that the test data of small cracks initiated in fine grains fall within the scatter bands of the long fatigue crack data. However, it is also observed that some very small cracks, initiated naturally from PSBs inside large grains, had much higher growth rates than the other small cracks (Figure 4.13). The different behavior of small cracks in large and small grains of Waspaloy provides more evidence of the critical role of grain size in the fatigue behavior of small cracks.

High applied tensile stress levels and a compressive stress are two important factors which promote the formation of PSBs and the initiation of microcracks in PSBs. The interaction between these PSB cracks and the main crack results in the fluctuation of crack

growth rates and sometimes leads to the higher growth rates of small cracks, see the scatter in data of small cracks at  $R = -1$  and  $\sigma_{\max} = 758$  MPa in Figure 4.11.

Figure 4.14 summarizes the test data for different  $R$  ratios and stress levels.

#### 4.1.3 René 95 (PM)

A comparison of the fatigue behavior for different  $R$  ratios at  $\sigma_{\max} = 758$  MPa, as well as for different stress levels at  $R = -1$  is shown in Figures 4.15 and 4.16, respectively. At the same maximum applied stress, the fatigue life was found to be the longest at  $R = 0.5$  and the shortest at  $R = -1$ . This fact is due to the small  $\Delta K$  at  $R = 0.5$ , a mode II effect and less closure effect at  $R = -1$ . The higher  $\sigma_{\max}$  results in a higher driving force for crack growth and thus a shorter fatigue life can be seen in Figure 4.16.

The crack growth rates,  $da/dN$ , versus  $\Delta K$  are shown in Figures 4.17 to 4.21 for three different  $R$  ratios and two different  $\sigma_{\max}$ , respectively. The test data for two different stress levels at  $R = -1$  are found to fall in same region in the plot of  $da/dN$  vs  $\Delta K$  (Figure 4.19). The small crack data points fall around the long crack trend at  $R = 0$  (Figure 4.20). In the case of  $R = -1$  and  $R = 0.5$ , the small crack data are distributed within a scatter band with a mean slope of 3, which is also the slope of long crack line (Figures 4.17, 4.18 and 4.21). It appears that the small cracks in René 95 obey the LEFM law of the long cracks. Only a few data points fall above the scatter bands (Figures 4.17 and 4.21), this is probably due to an underestimation of the stress concentration around inclusions and the role of the debonded interfaces [37].

By comparing the results of René 95 to those of Inconel X-750, the grain size is found to be a critical factor in the small crack behavior. The small cracks in Inconel X-750 with large grains have obvious small crack behavior (higher growth rates than long cracks at the same nominal driving force), but small cracks in fine grain PM René 95 behave like long cracks. This fact can be understood from the discussion given in the last section.

When the grain size is very small such as in PM René 95, the free surface effect (less plastic constraint) almost disappears since the plastic zone size and crack length are all far greater than the grain size, no difference exists between small cracks and long cracks. On the other hand, the closure effect (mostly the roughness induced closure effect) happens very early for small cracks in fine grains because the dimension of surface roughness is directly related to the grain size. So the closure effect and thus the effective driving force between small cracks and long cracks in very fine grains are almost same.

Figure 4.22 shows a summary of all test data points for  $R = -1, 0, 0.5$ . It seems that the  $R$  effect for PM René 95 is not as strong as for Inconel X-750. It is probably due to the small grain size leading to less closure and less mode II.

#### 4.1.4 Fractography, Room Temperature Tests

##### Inconel X-750

Metallographic examination revealed that at low applied stress ranges, small cracks initiated from or around EDM pits and then propagated approximately perpendicular to the applied stress following a zig-zag path. Initiation sites at inclusions and propagation along twin boundaries were also observed. At high stress ranges, initiation of small cracks also occurred along persistent slip bands which developed around the EDM pits. These microcracks then linked together to form a main crack.

The preferred initiation of small cracks at EDM pits or inclusions at low stress ranges is obviously due to the strong stress concentration. At stresses approaching the surface flow stress of the alloy, extensive plastic deformation occurs at the specimen free surface, especially around EDM pits, resulting in PSBs in the grains of favorable orientation. These PSBs promote the initiation of small cracks.

The specimen with a small crack initiated from an EDM pit (Figure 4.23) was broken open to show the corresponding fracture surface (Figure 4.24). The examination of the fracture surface shows crystallographic growth features in the small crack region (Figure 4.25).

The crystallographic growth is one of the important factors which affects the growth rate of small cracks. As pointed by Schijve [15], the elastic restraint surrounding a small crack in a free surface is very different from that experienced at the tip of a long crack inside the material. For a small surface crack with size of the order of the grain size, the low plastic constraint on the free surface results in only a few active slip systems. The cyclic plastic slip along the slip system of the highest critical resolved shear stress produces a mode II + mode I slip band crack, which has strong crystallographic growth features. For a long crack front which spans many grains, maintaining such slip band cracking in a single direction in each grain is difficult. This results in an increased restraint on cyclic plasticity which activates more slip systems leading to crack advance by alternating or simultaneous shear on many different slip systems.

When the crack is long the crack mouth was found to remain open even at zero applied stress, due to a "crack closure effect," which is induced by fracture surface roughness. When the crack is small this closure effect decreases and even disappears when the crack length is less than some critical length.

A lower closure stress for small cracks than for long cracks is one of the most important factors which leads to the faster growth rate of small cracks than for long cracks at the same nominal  $\Delta K$ .

The zigzag propagation paths of the small cracks were quantified by measuring the angle distribution spectrum. The frequency of occurrence for angle  $\Theta$ ,  $F(\Theta)$ , was computed using

$$F(\Theta) = 1/L_{tot} [\sum_{i=0}^{n_i} L_i(\Theta)] \quad (4.6)$$

where  $L_i(\Theta)$  is the length of a segment of crack which is at  $\Theta$  degree with respect to the plane perpendicular to the applied stress.

$L_{tot}$  is the total crack length and given by

$$L_{tot} = \sum_{\Theta=0}^{90} \sum_{i=0}^{n_i} L_i(\Theta) \quad (4.7)$$

Figure 4.26 shows the angle distribution of a typical zig-zag small fatigue crack at low applied stress within a total length of about 900  $\mu\text{m}$ . It was found that the maximum distribution, i.e. the most probable deviation angle, takes place for  $40^\circ < \Theta < 55^\circ$ .

Near the threshold for small cracks and even for some long cracks, if the extent of local plasticity is small enough to be contained within a single grain, the cracks will propagate by a single shear mechanism with the orientation of the slip band crack changing at each grain boundary, thus leading to a faceted or zig-zag crack path. The occurrence of this shear mode of crack extension, together with the development of a faceted fracture surface, will result in the roughness induced closure effect.

#### René 95 (PM)

The fatigue cracks were initiated from debonded inclusions (Figure 2.8a). No slip band cracks were observed. The preferred initiation at inclusions can be understood by the dislocation model proposed by Tanaka and Mura [38]. This model described localized decohesion around inclusions. These localized decohesions clustered to cause complete debonding. The debonded particles and the corresponding surface intrusions/extrusions constitute strong stress concentration centers which favor microcracks initiation.

Figures 4.27a and 4.27b show that the zigzag small crack initiated from a debonded inclusion still remained open at the crack tip and at the crack root under zero applied stress.



The shear mechanism of mode II deformation can be clearly observed. This mode II deformation combined with the fracture surface roughness results in the "roughness induced crack closure effect".

Figure 4.28 shows that fracture surface of a small crack after intentionally breaking the specimen open. The fracture path is predominately transgranular.

#### Waspaloy

Figure 4.29 shows a small crack initiated from an EDM pit. Figure 2.8b shows clearly that small cracks also initiate from persistent slip bands. Most small cracks initiated from slip bands stop growing before or at grain boundaries. The grain boundaries offer an obstacle to the growth of small cracks.

Extensive plastic deformation associated with crack propagation was found at the crack tip as well as around the crack wake (Figure 4.30). The crack propagation along slip bands can also be observed.

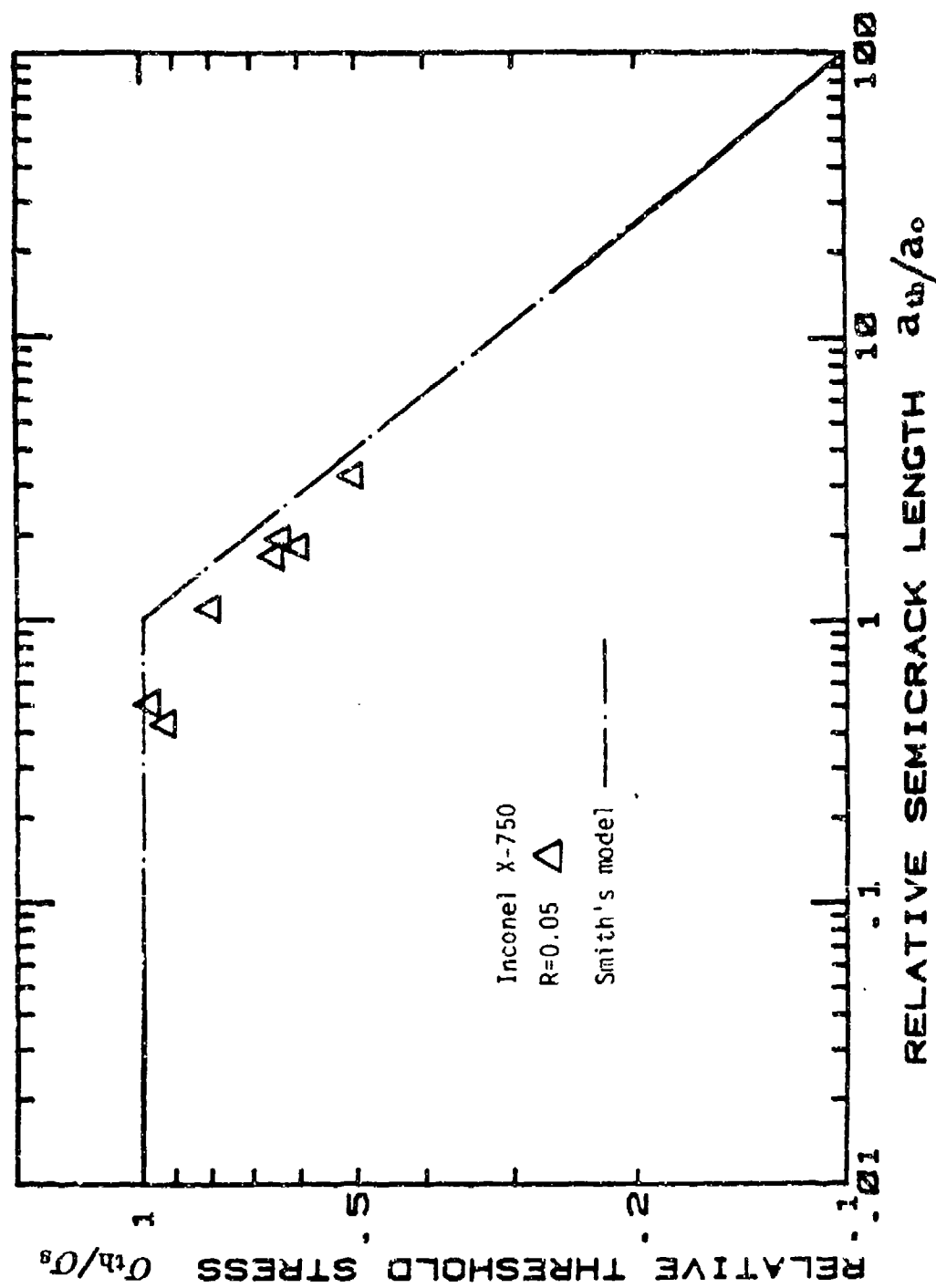


Figure 4.1 Normalized relation between threshold stress and crack length for Inconel X-750 tested at 25C,  $R = 0.05$ .

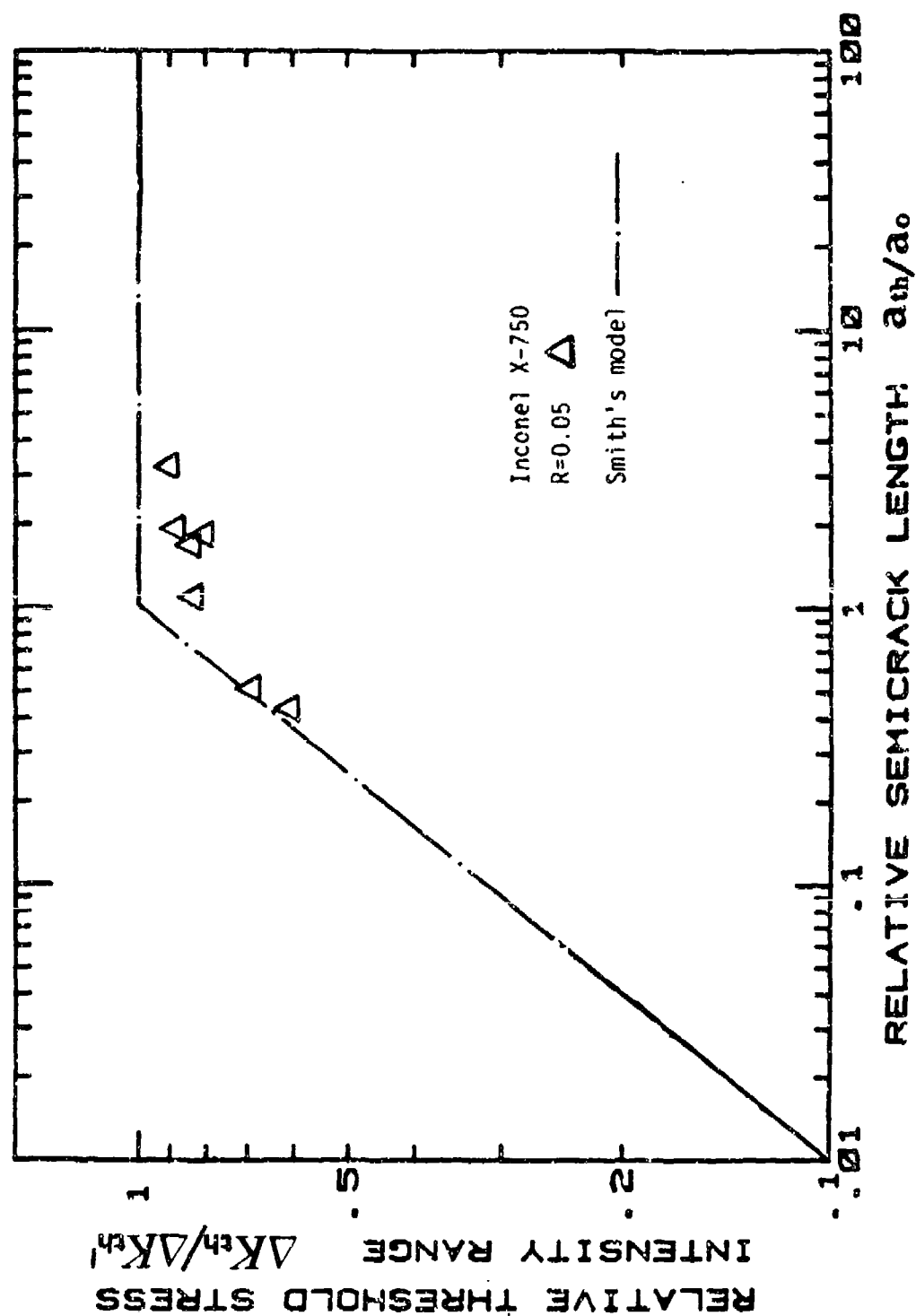


Figure 4.2 . Normalized relation between threshold stress intensity factor range and crack length for Inconel X-750 tested at 25°C,  $R \approx 0.05$ .

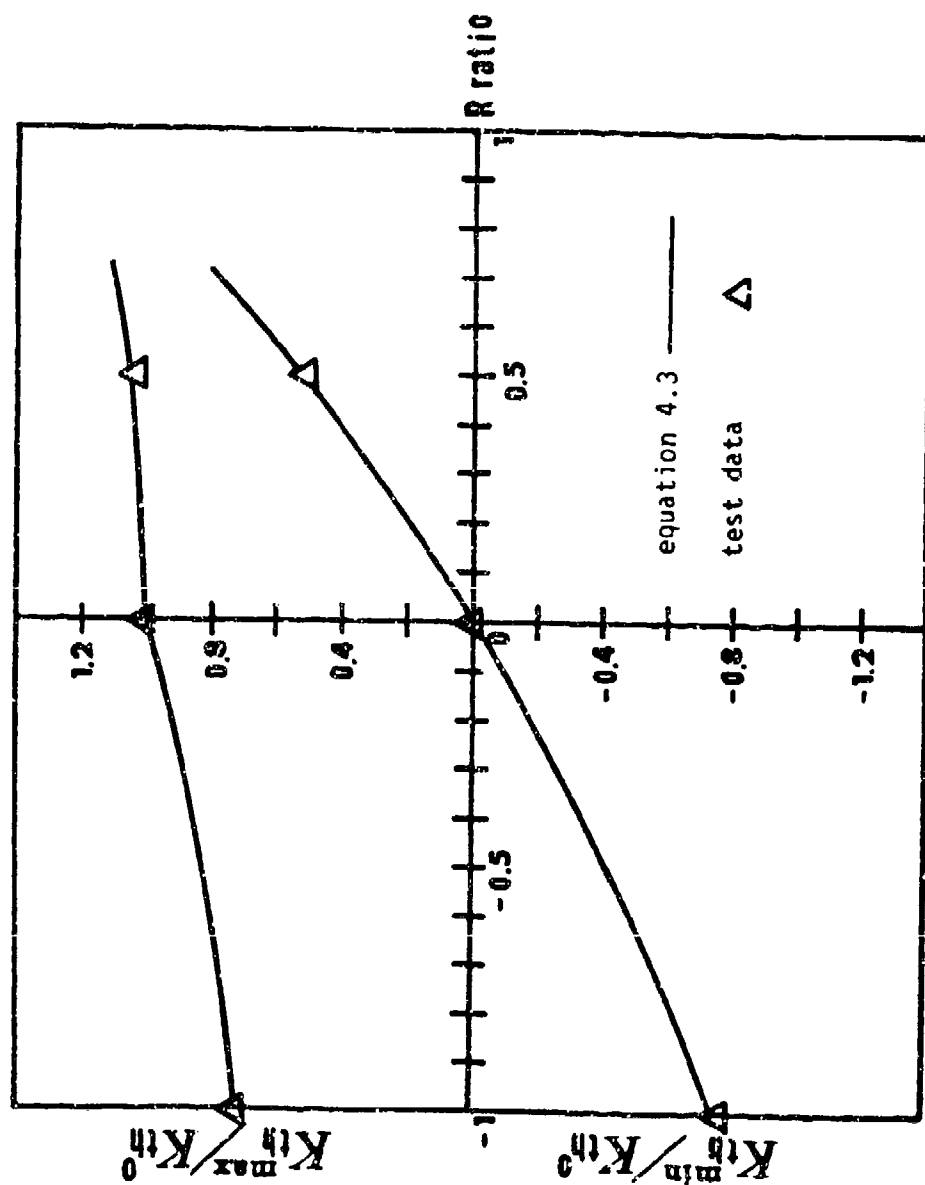


Figure 4.3 Normalized relation between threshold stress intensity factor range and load ratio,  $R$ , for Inconel X-750 tested at 25°C.

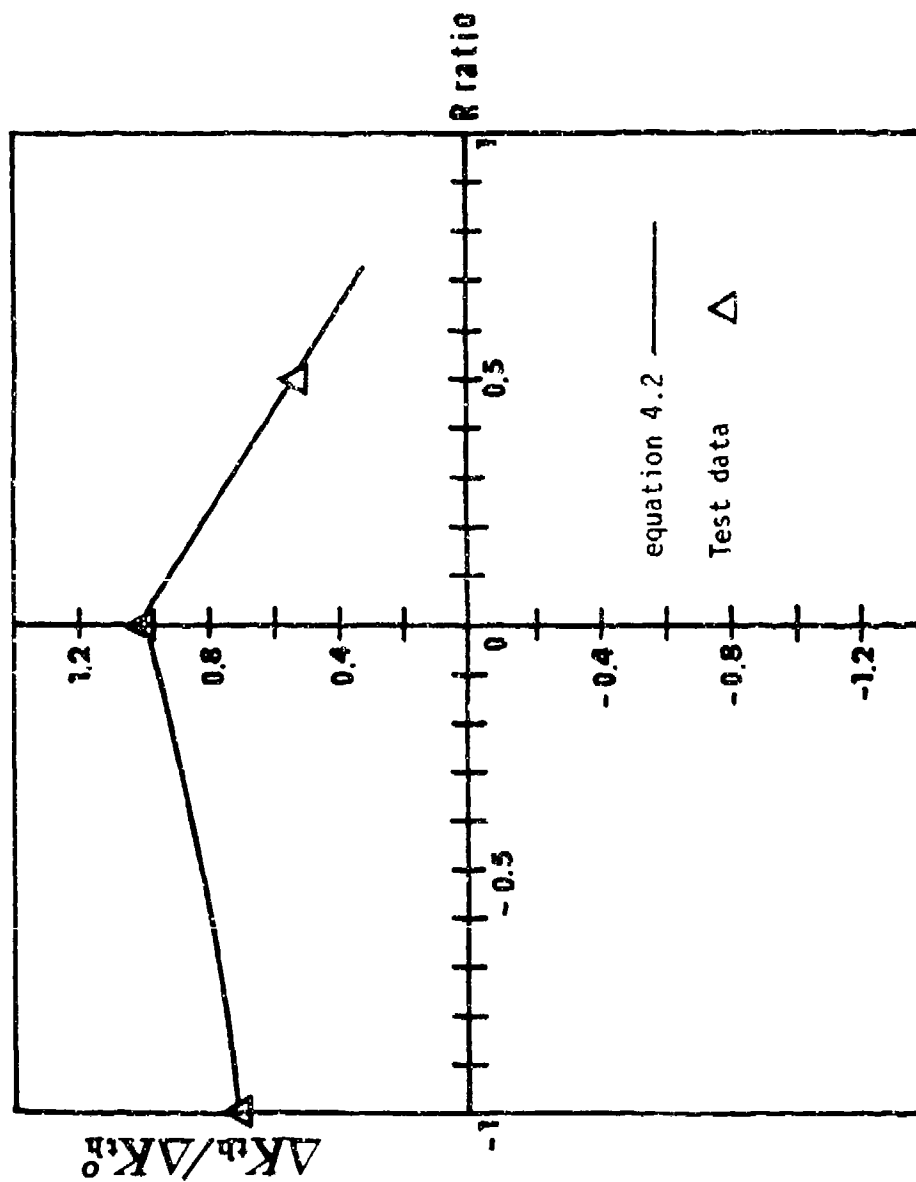
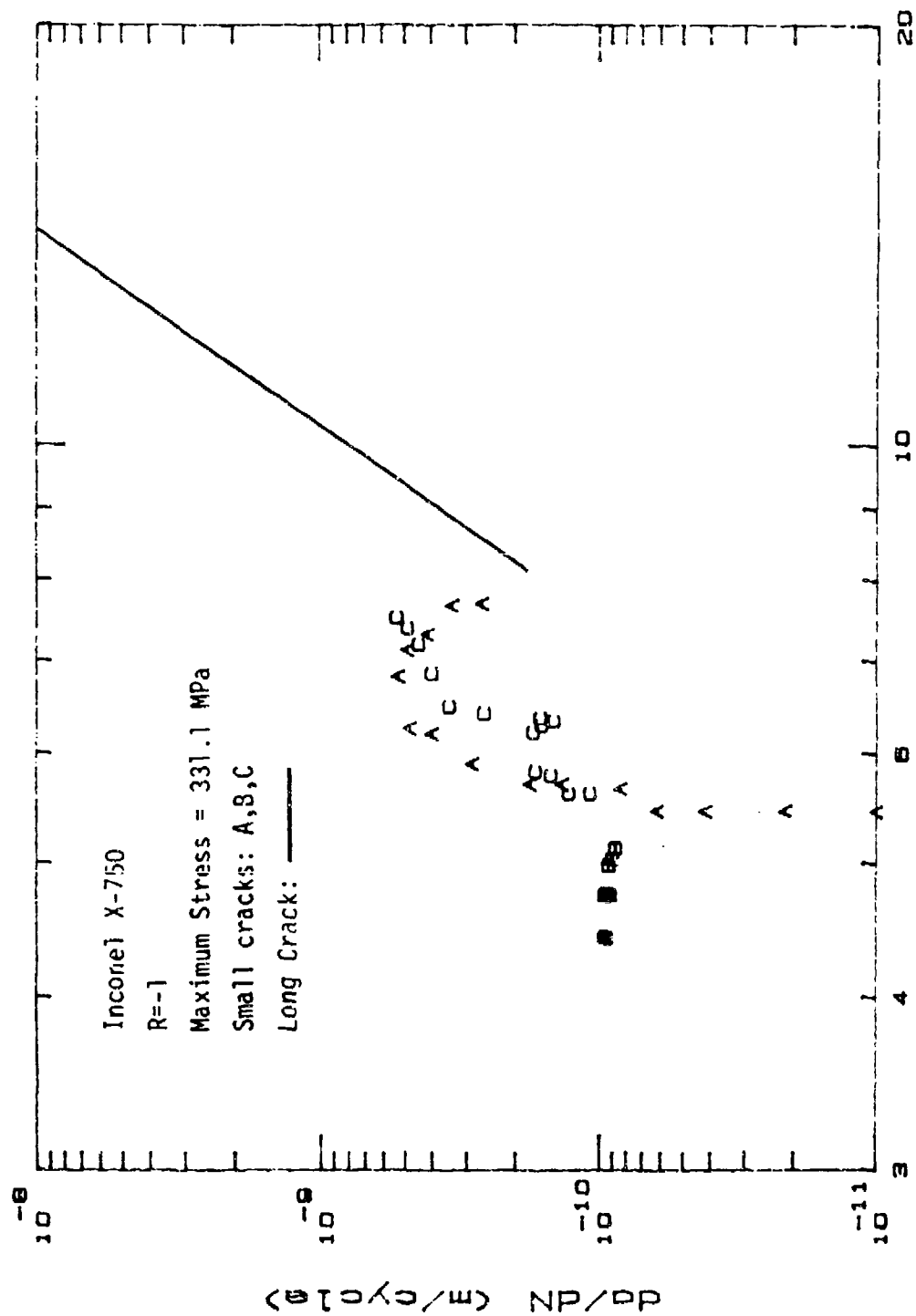


Figure 4.4 Normalized relation between threshold stress intensity factor and load ratio,  $R$ , for Inconel X-750 tested at 25°C.



STRESS INTENSITY FACTOR RANGE  $\Delta K$  ( $\text{MPa}\sqrt{\text{m}}$ )

Figure 4.5 Fatigue crack growth rates versus stress intensity factor range for Inconel X-750 tested at 25°C, R = -1.

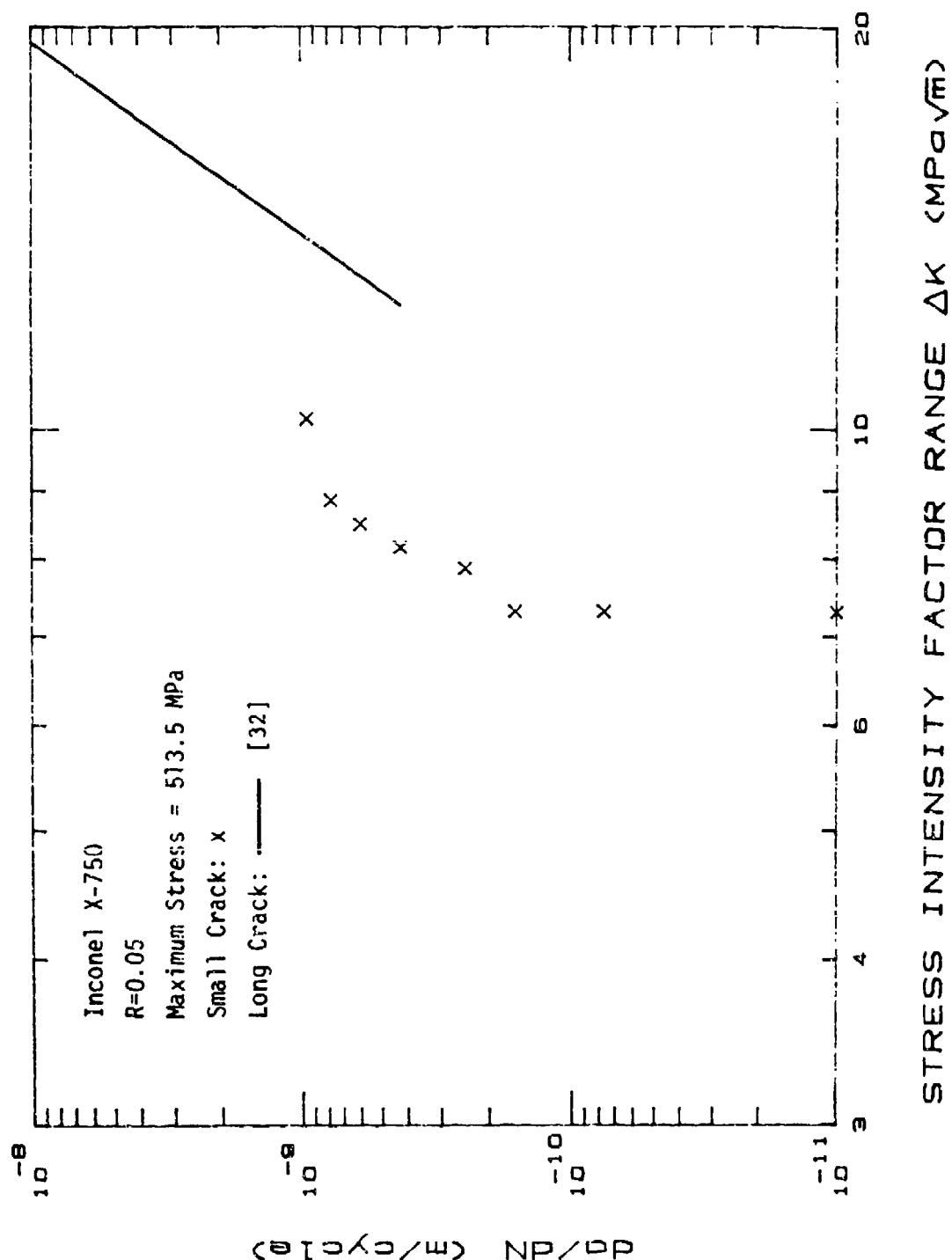
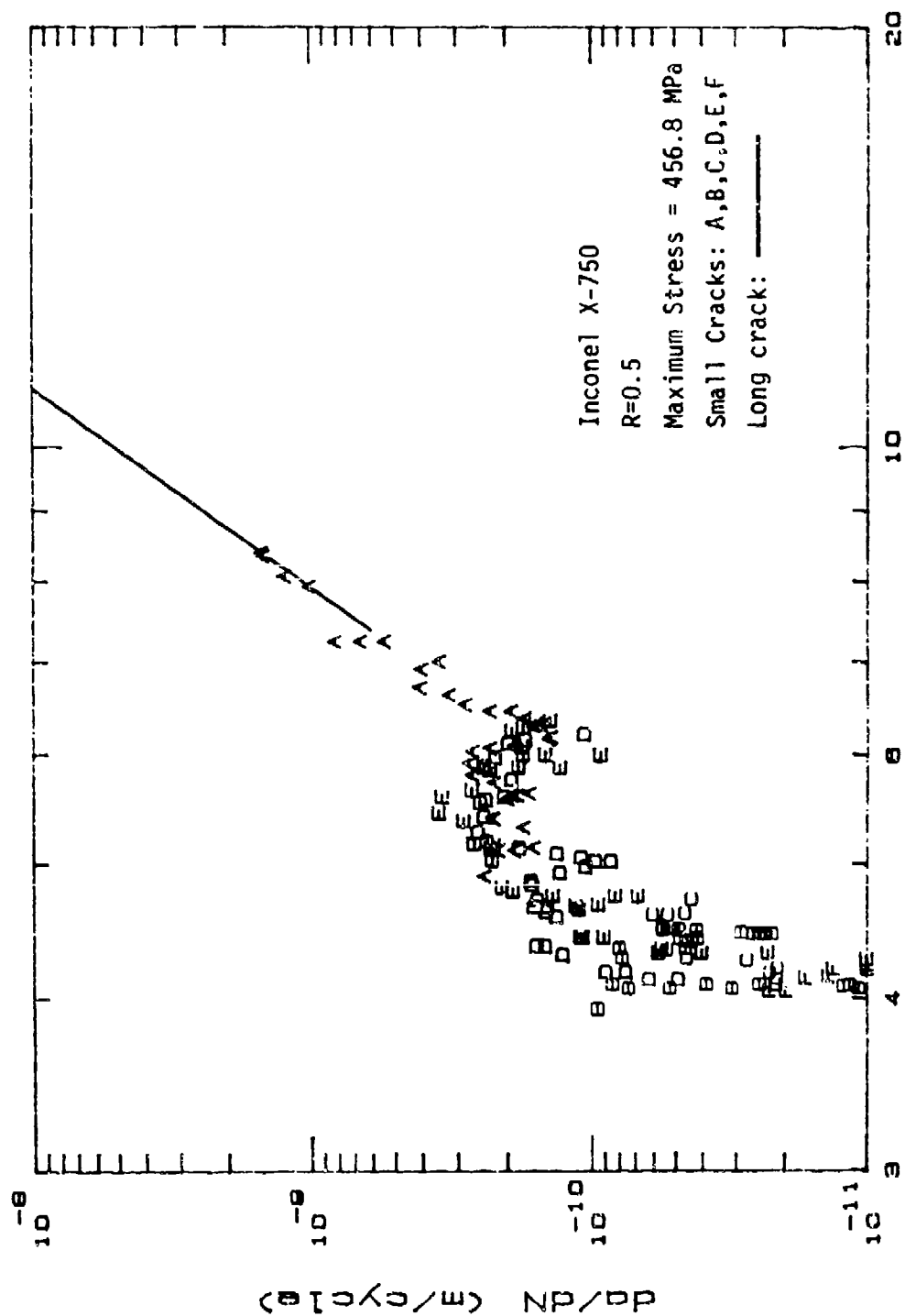


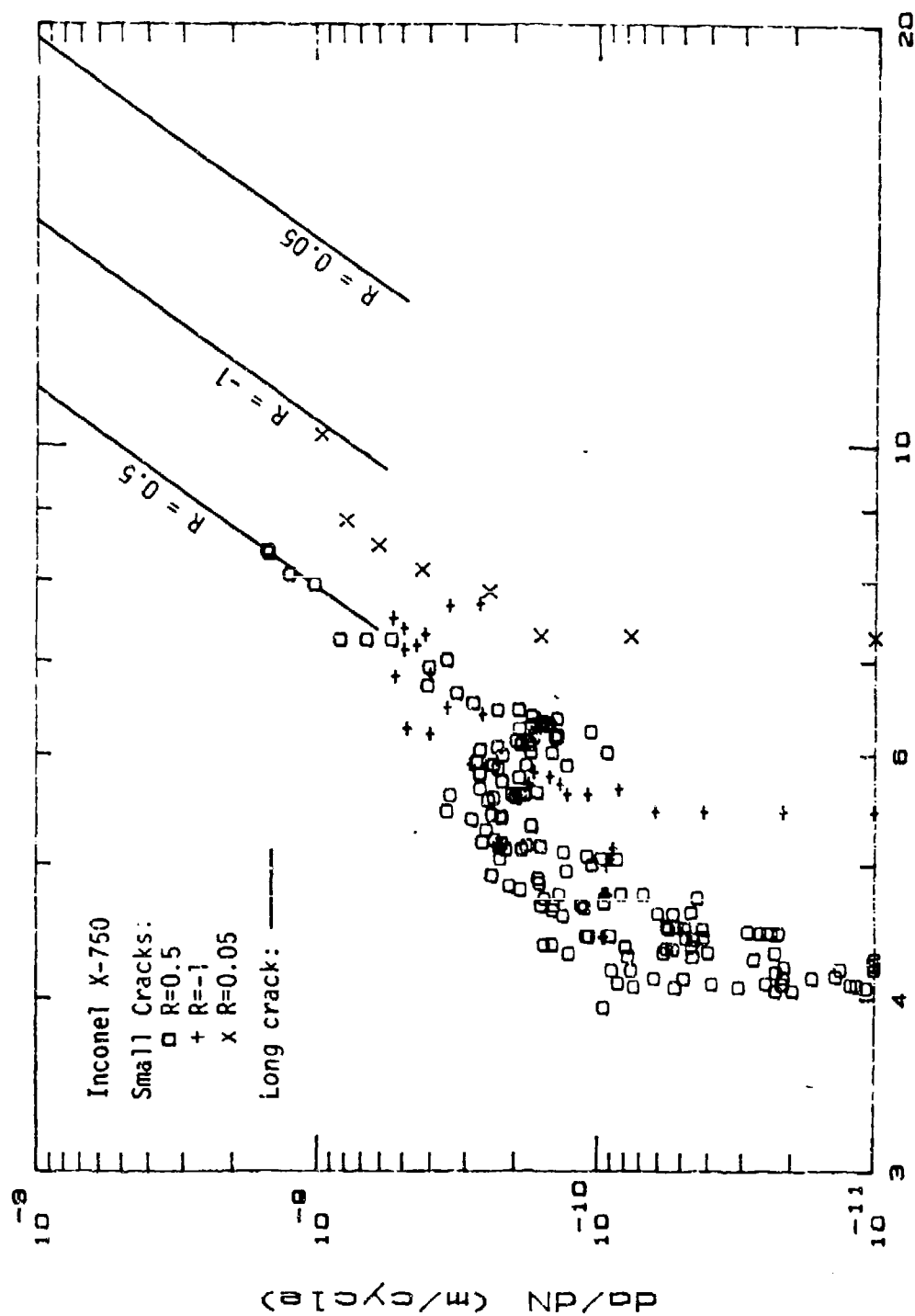
Figure 4.6 Fatigue crack growth rates versus stress intensity factor range for Inconel X-750 tested at 25° C, R = 0.05.



# STRESS INTENSITY FACTOR RANGE $\Delta K$ (MPa $\sqrt{m}$ )

Figure 4.7 Fatigue crack growth rates versus stress intensity factor range for Inconel X-750 tested at 25°C, R = 0.5.





STRESS INTENSITY FACTOR RANGE  $\Delta K$  (MPa $\sqrt{m}$ )

Figure 4.8 Summary of the fatigue crack growth rates versus stress intensity factor range for Inconel X-750 tested at 25°C; R ratio varied.

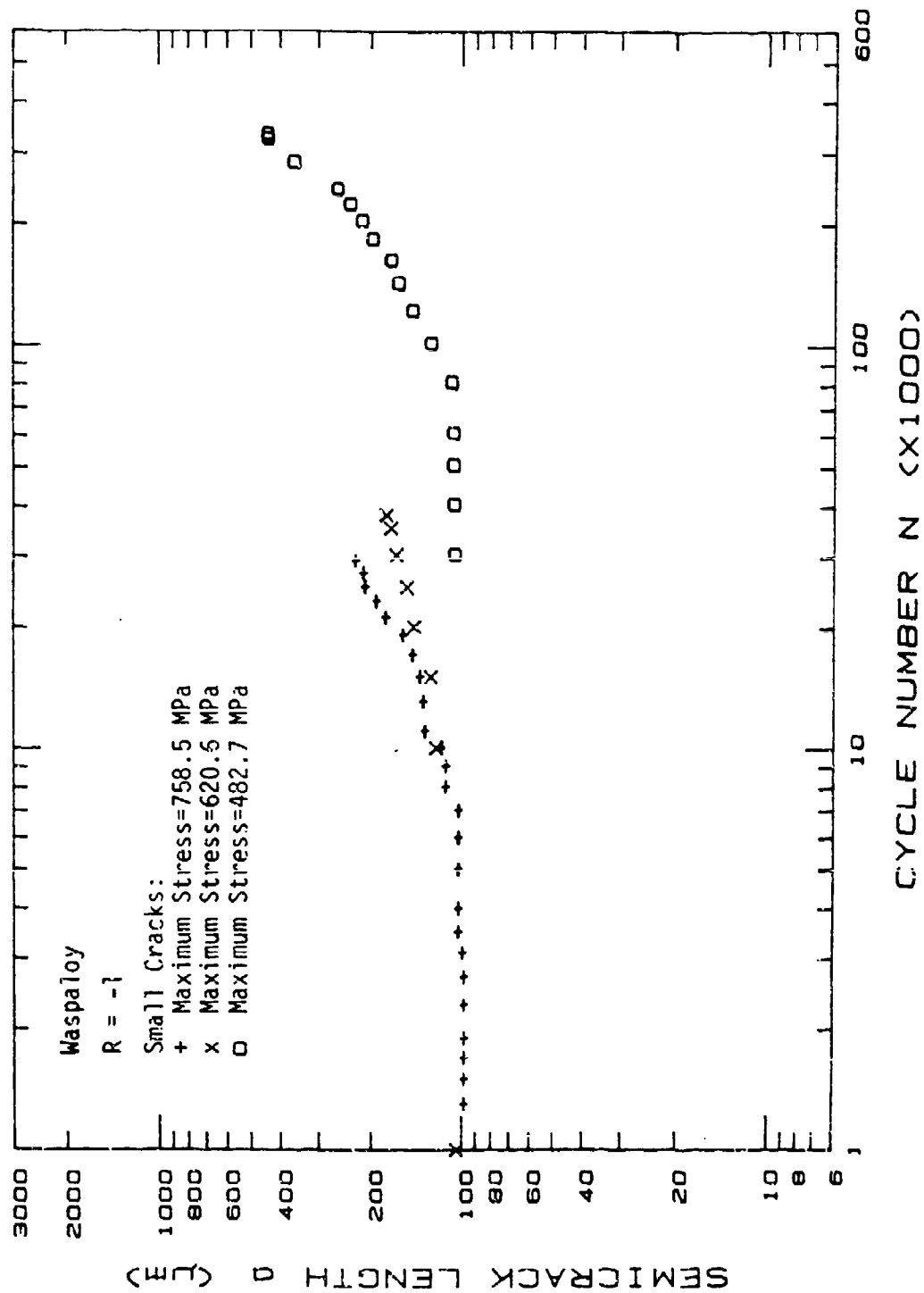


Figure 4.9 Crack length versus cycle number for Waspalloy tested at 25° C, Max. Stress varied,  $R = -1$ .

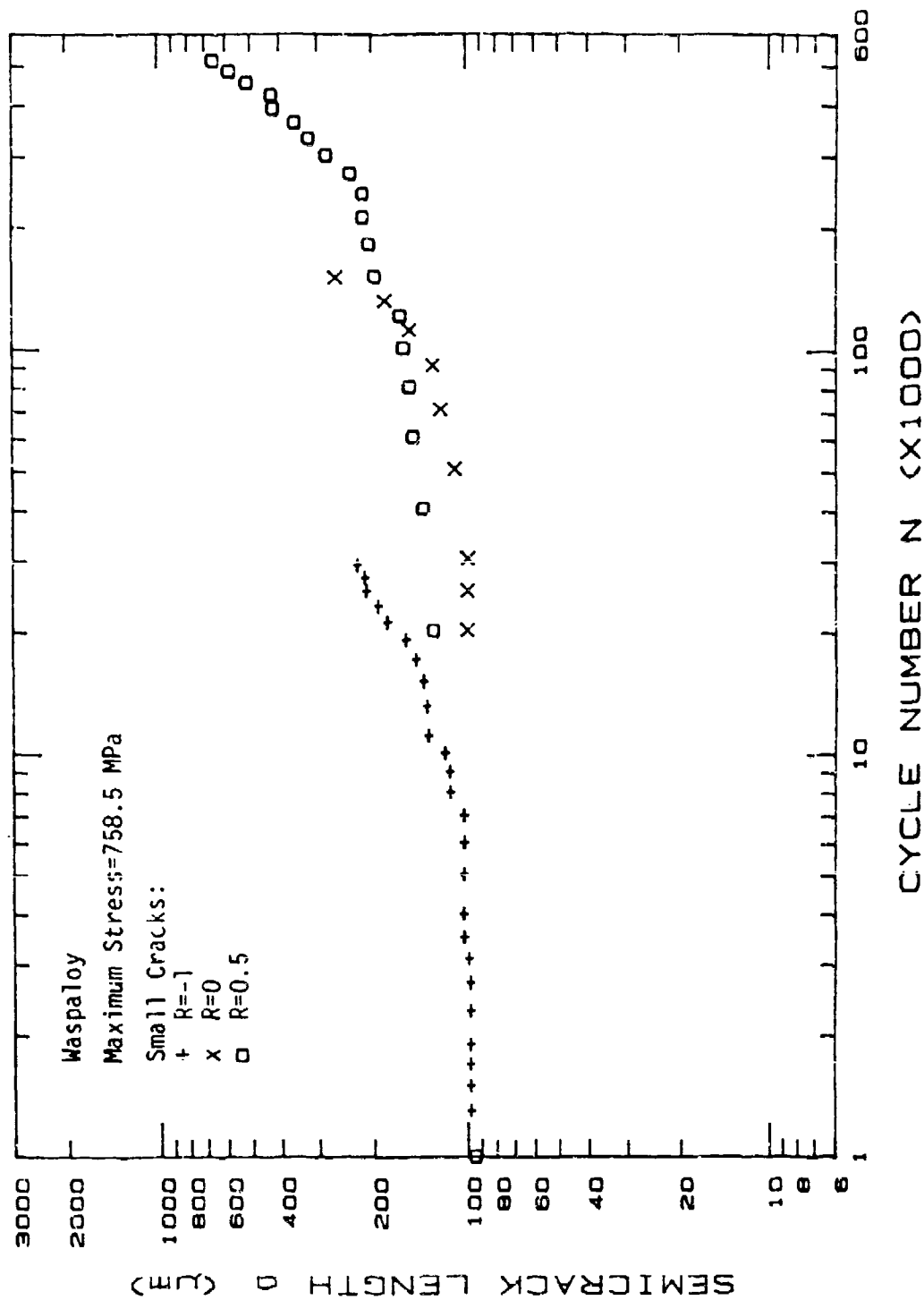
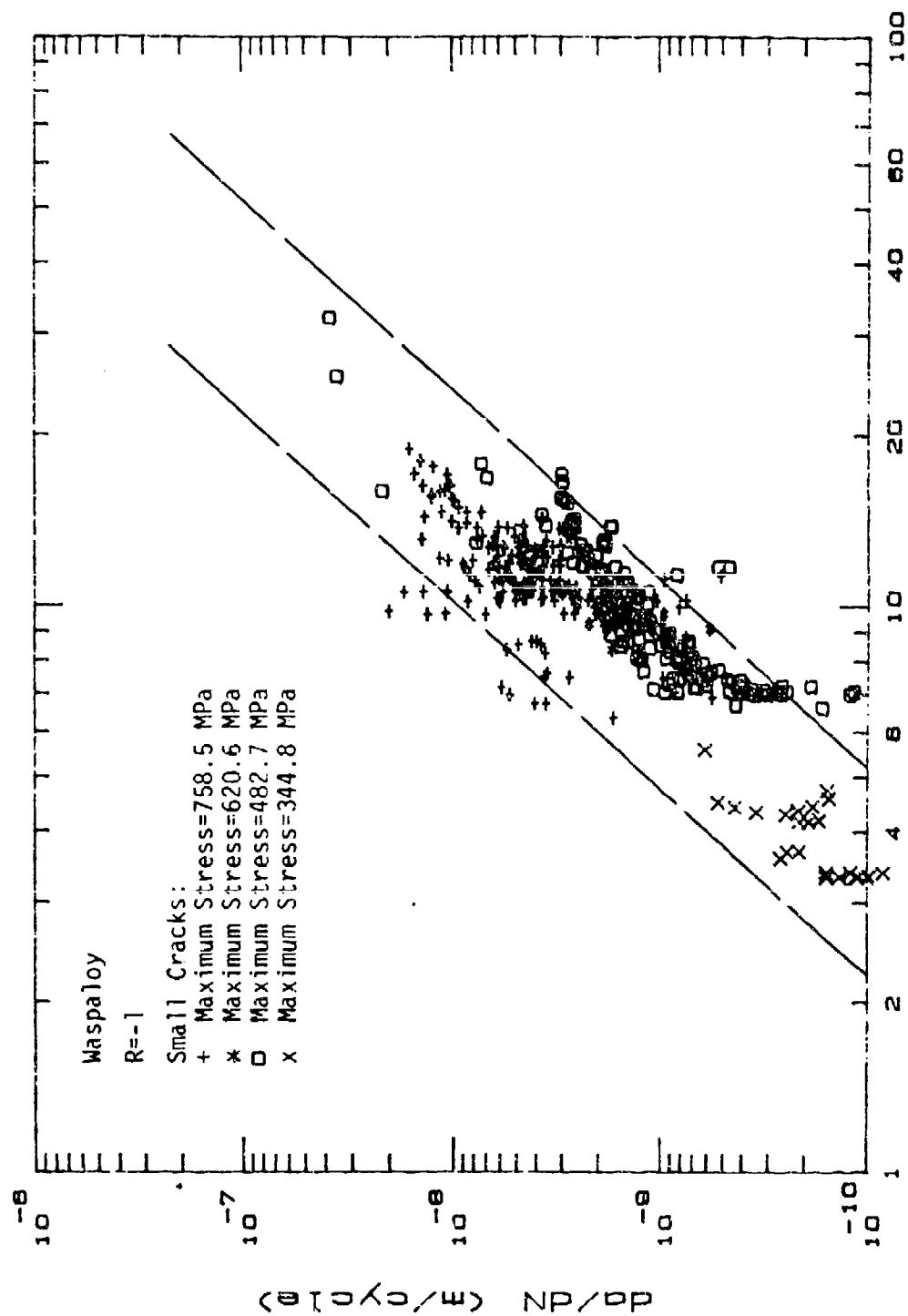
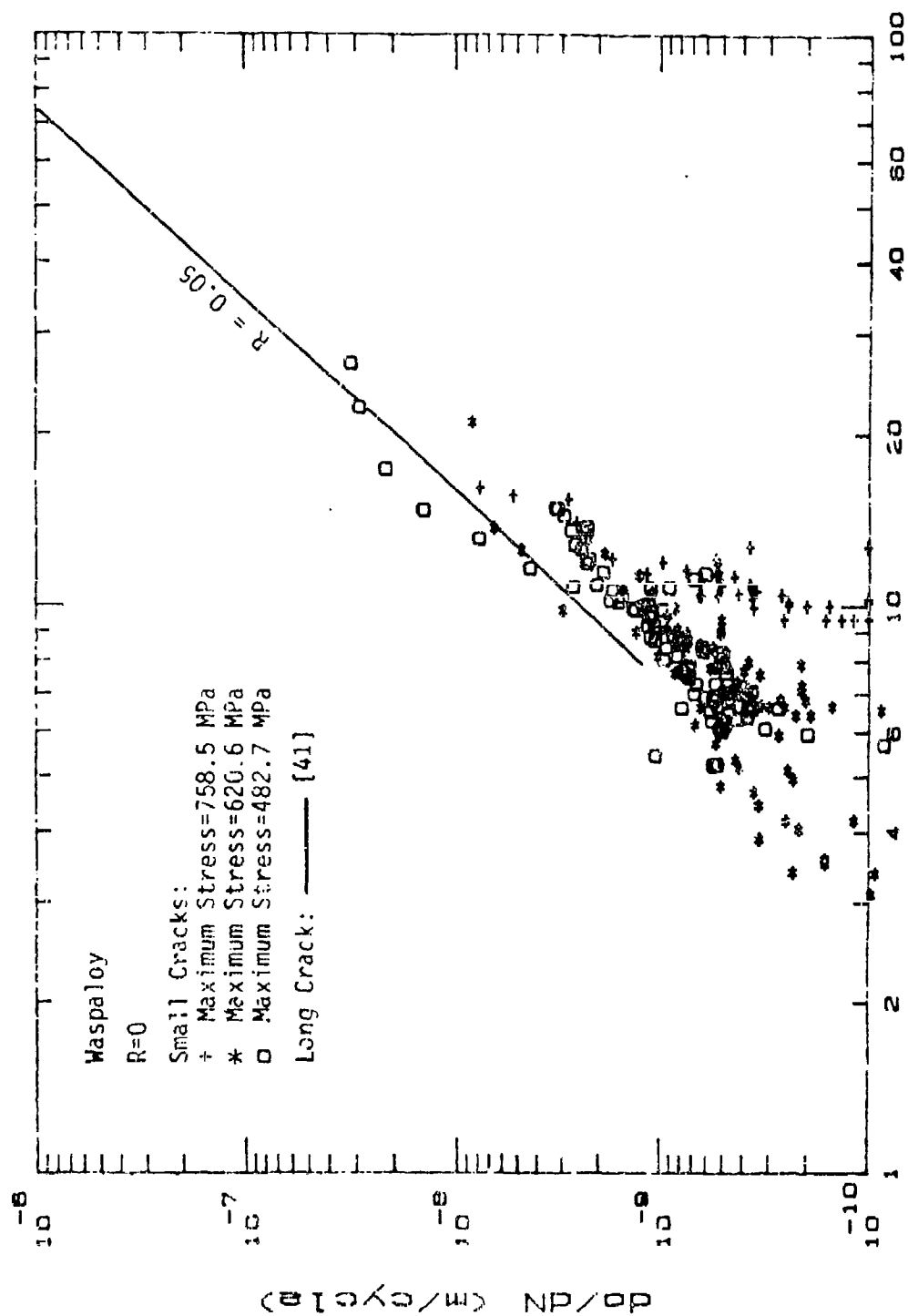


Figure 4.10 Crack length versus cycle number for Waspaloy tested at 25° C, Max. Stress = 758 MPa, R ratio varied.



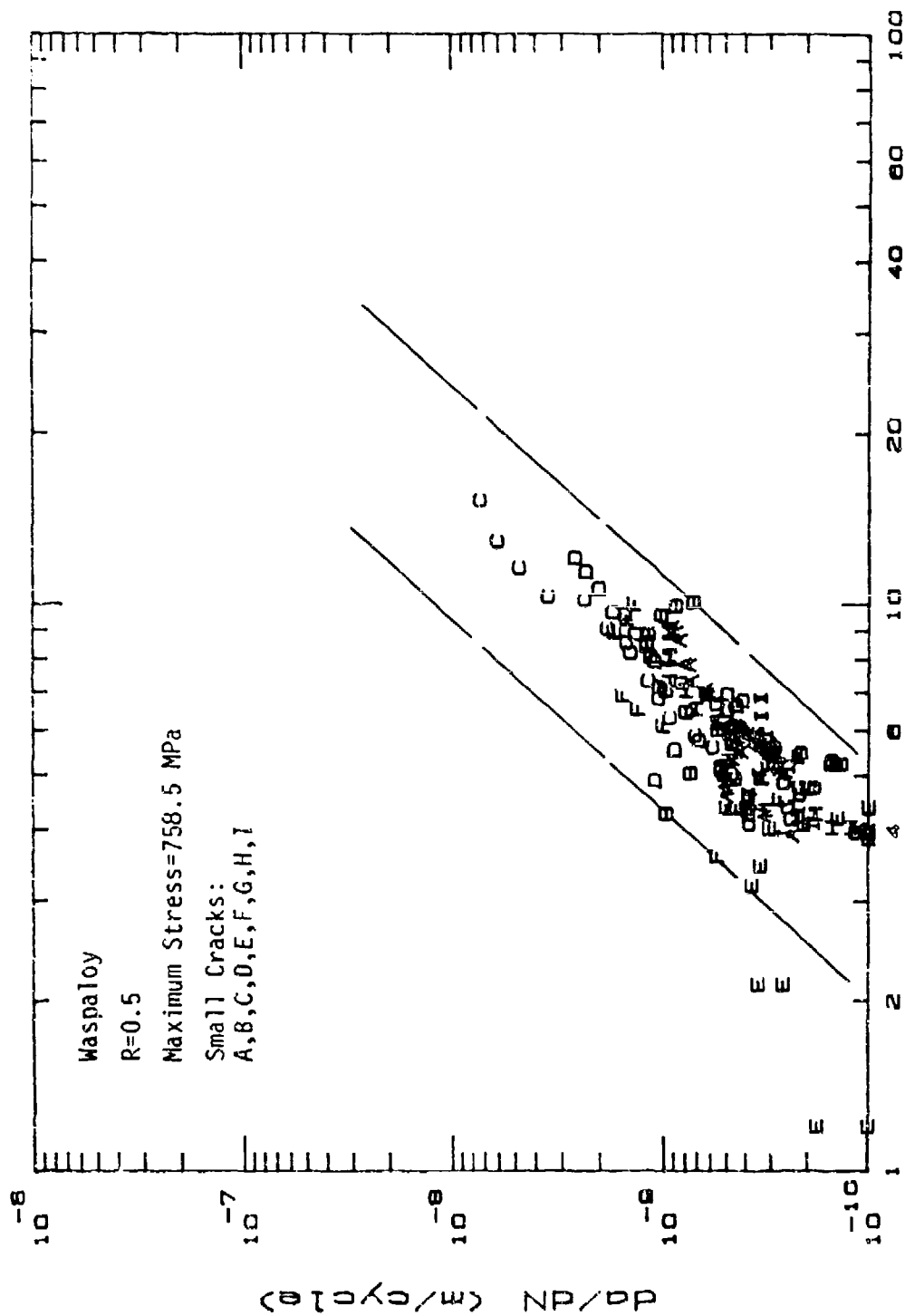
STRESS INTENSITY FACTOR RANGE  $\Delta K$  (MPa $\sqrt{m}$ )

Figure 4.11 Summary of fatigue crack growth rates versus stress intensity factor range for Waspaloy, tested at 25°C, R = -1.



STRESS INTENSITY FACTOR RANGE  $\Delta K$  (MPa $\sqrt{m}$ )

Figure 4.12 Summary of fatigue crack growth rates versus stress intensity factor range for Waspaloy, tested at 25°C, R = 0.



STRESS INTENSITY FACTOR RANGE  $\Delta K$  (MPa $\sqrt{m}$ )

Figure 4.13 Fatigue crack growth rates versus stress intensity factor range for Waspaloy, tested at 25°C, Max. Stress = 758 MPa,  $R = 0.5$ .

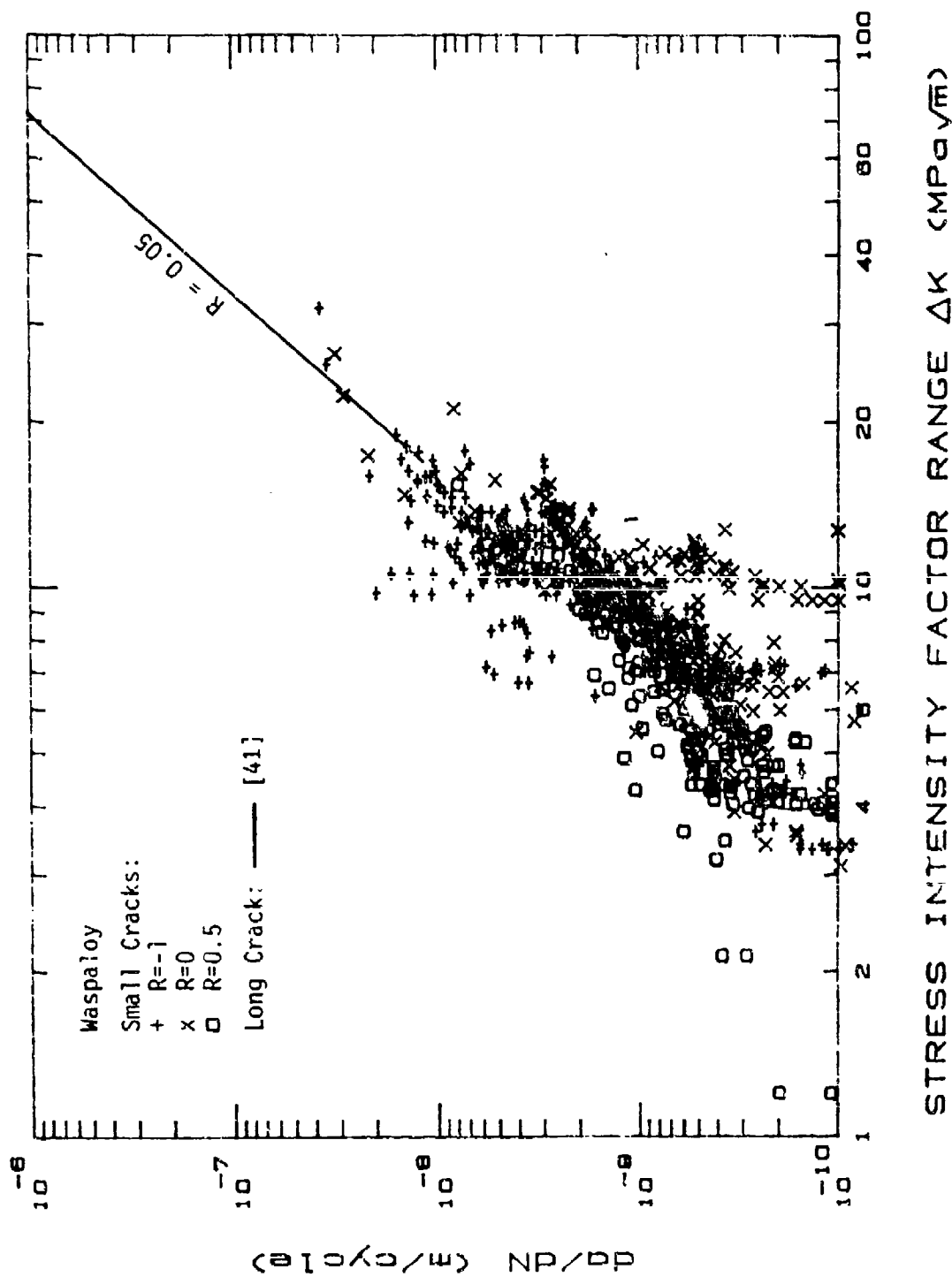


Figure 4.14 Summary of fatigue crack growth rates versus stress intensity factor range for Waspaloy, tested at 25°C, R varied.

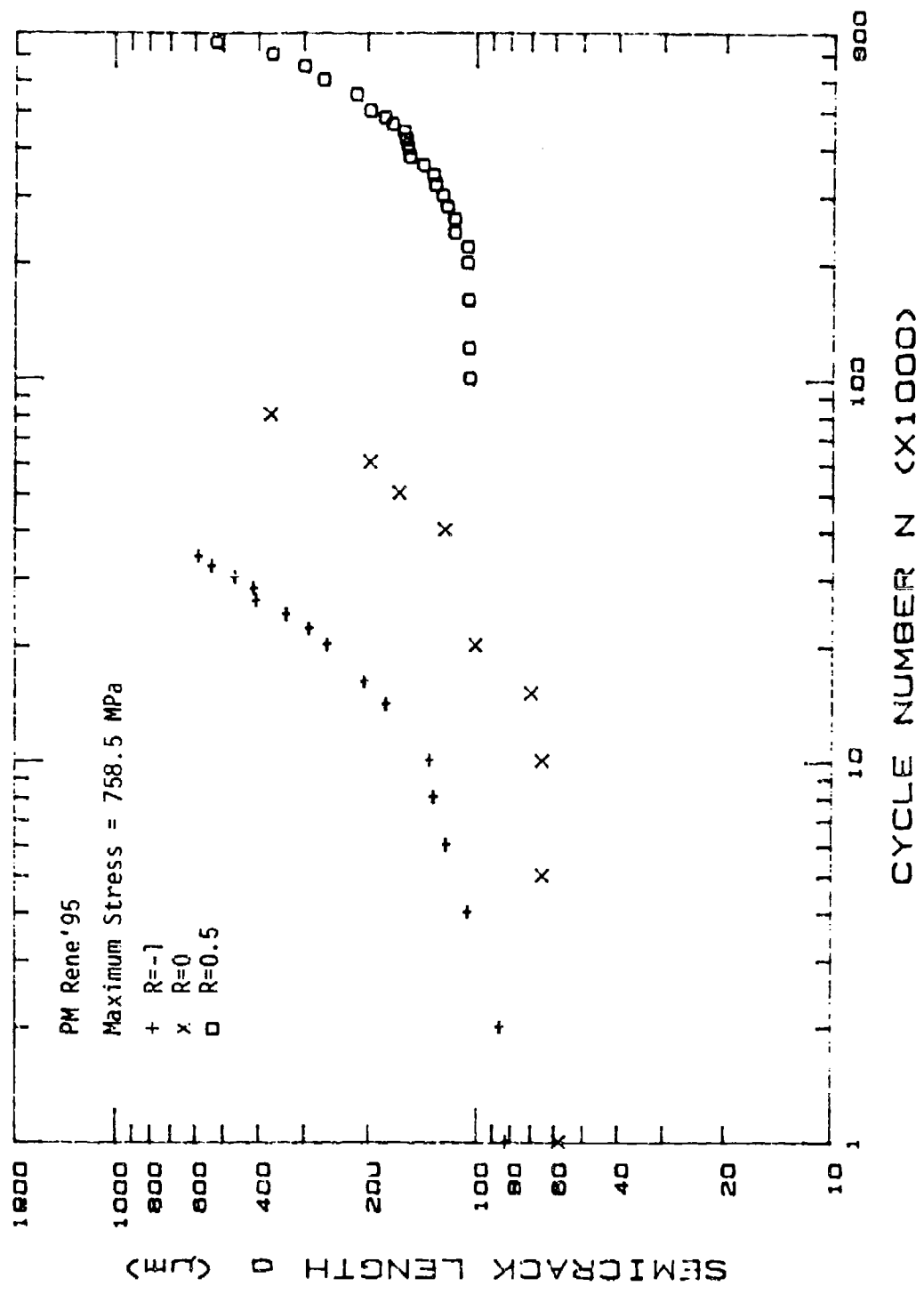


Figure 4.15 Crack length versus cycle number for René 95 (PM) tested at 25° C, Max. Stress = 758 MPa, R varied.



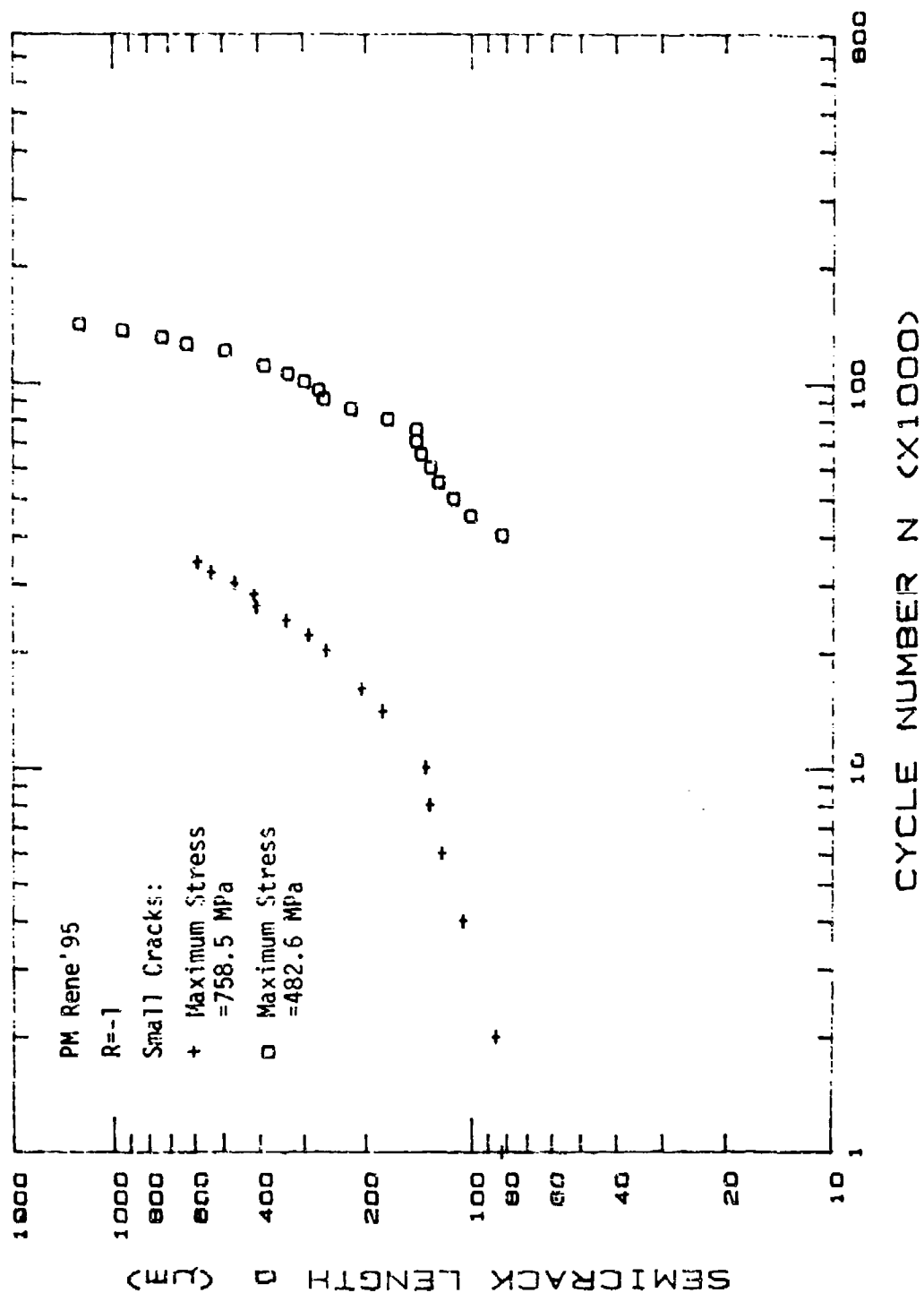


Figure 4.16 Crack length versus cycle number for René 95 (PM) tested at 25° C, Max. Stress was varied, R = -1.

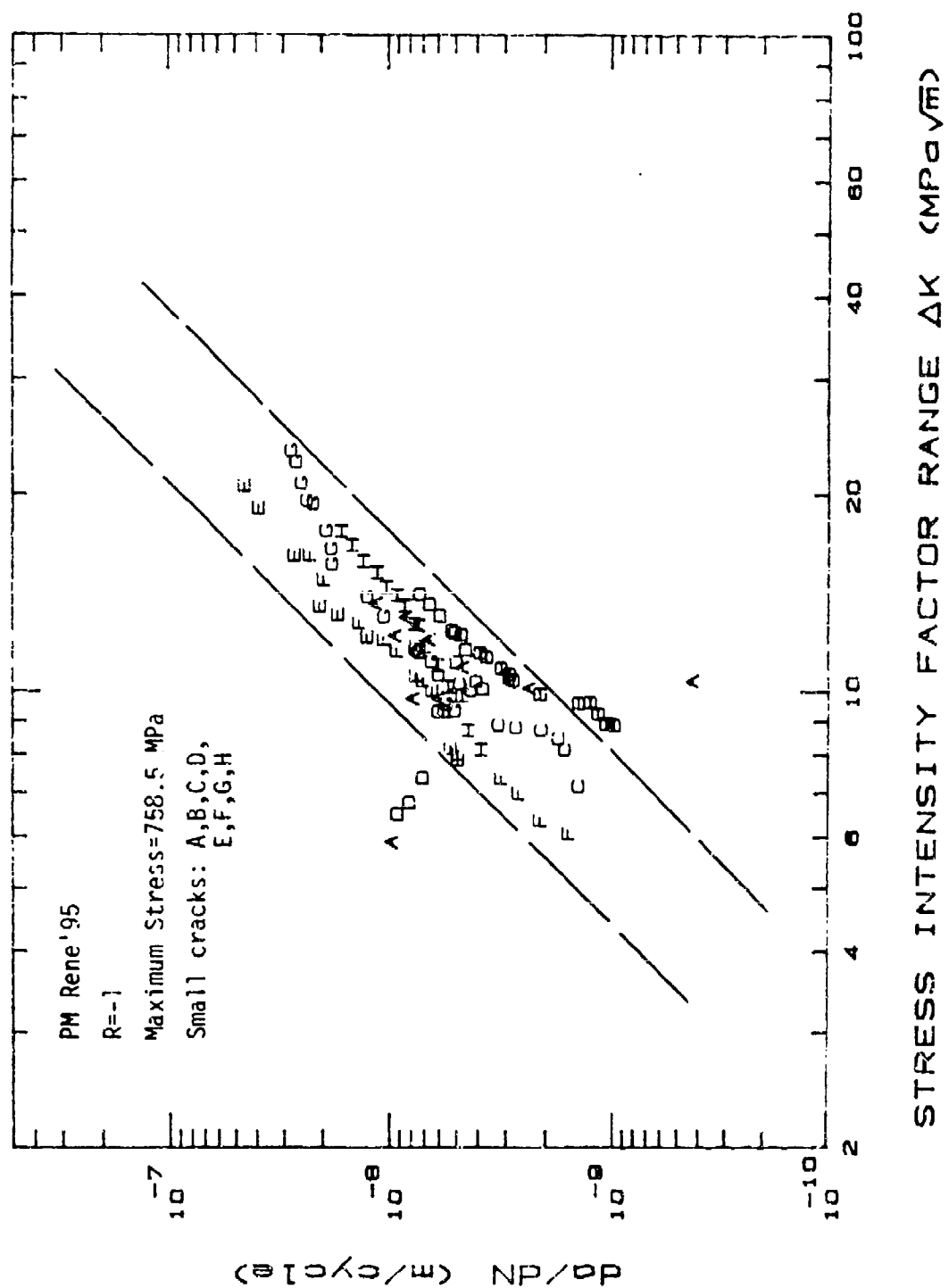


Figure 4.17 Fatigue crack growth rates versus stress intensity factor range for René 95 (PM), tested at 25°C, Max. Stress = 758 MPa,  $R = -1$ .

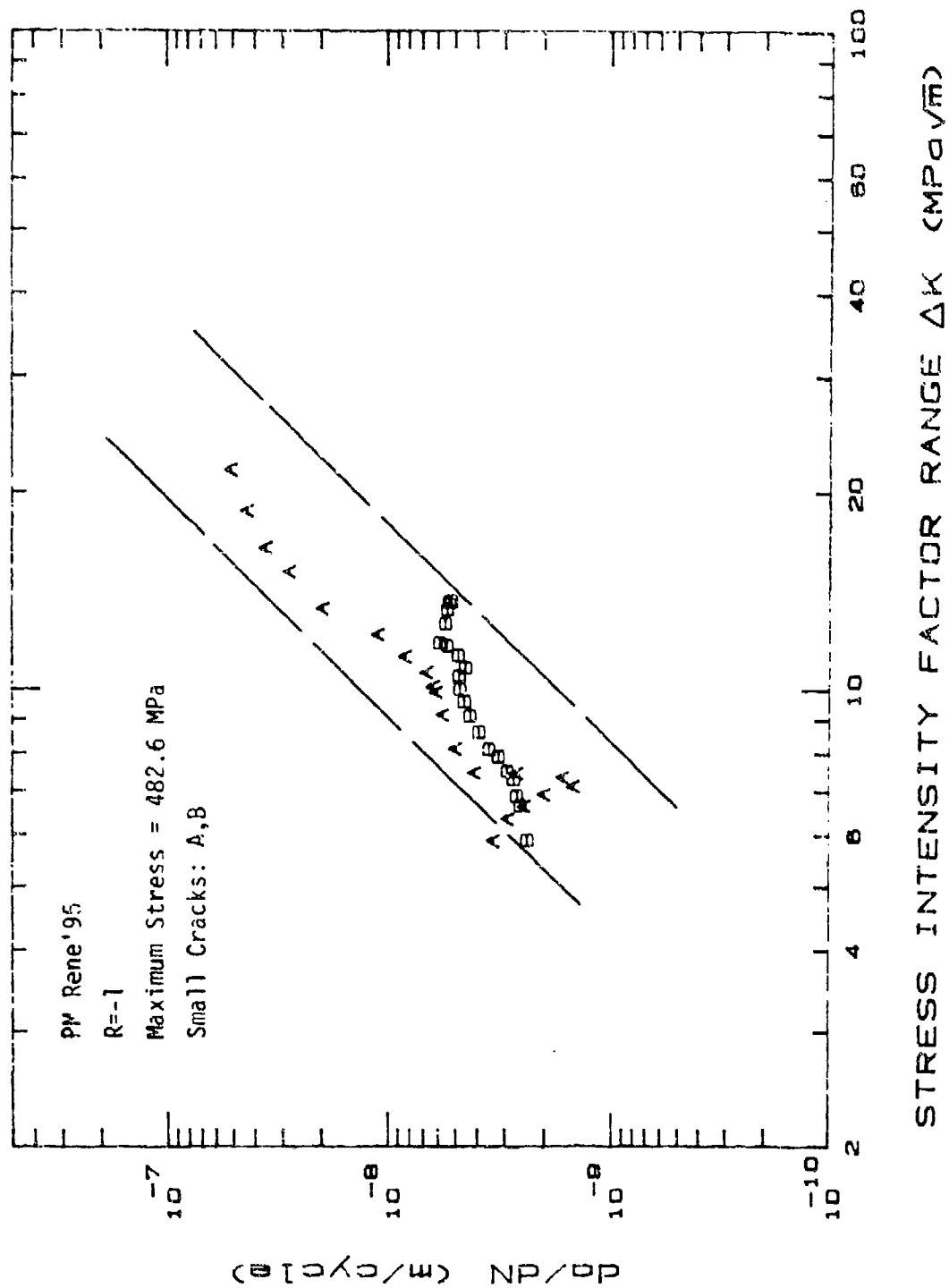
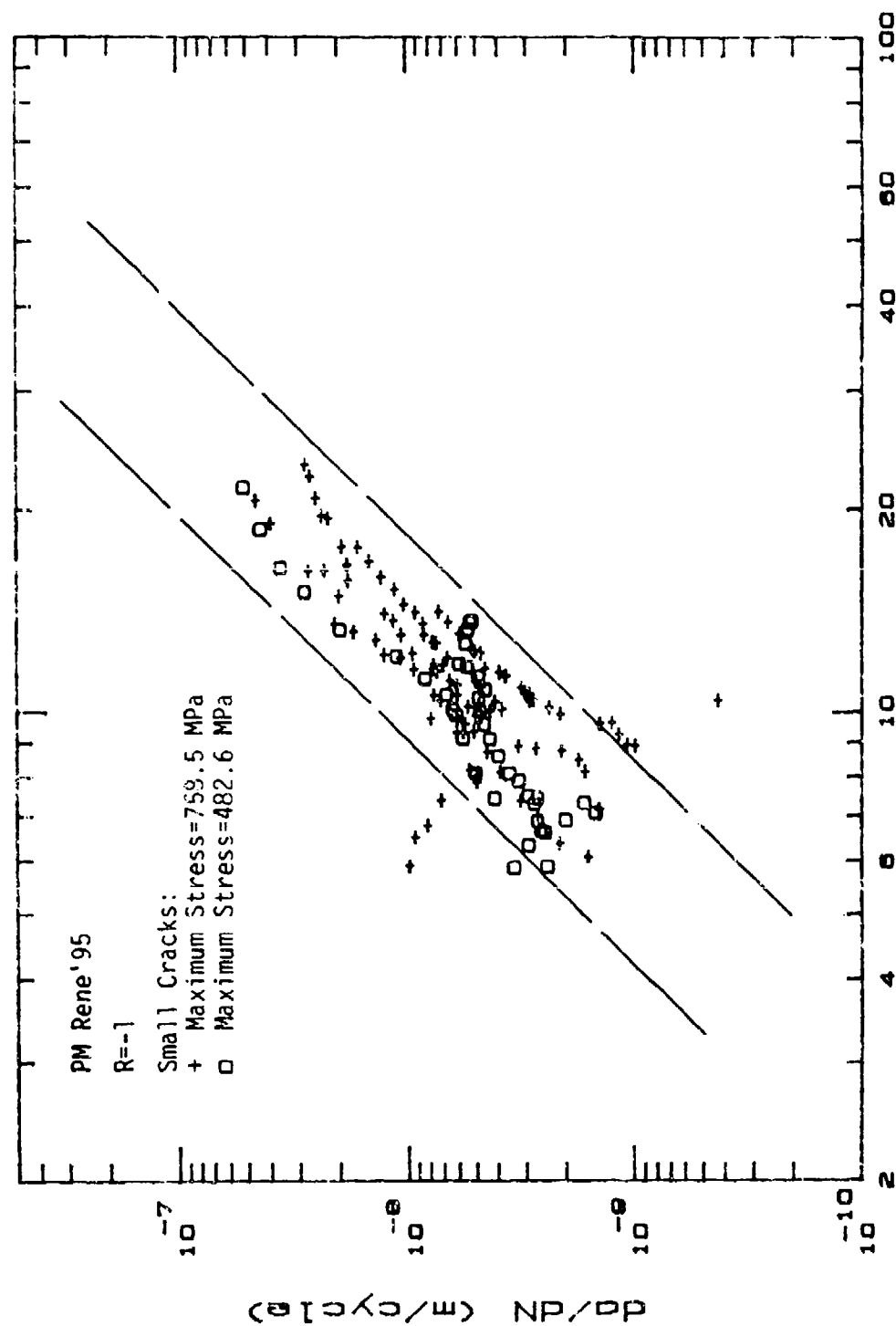
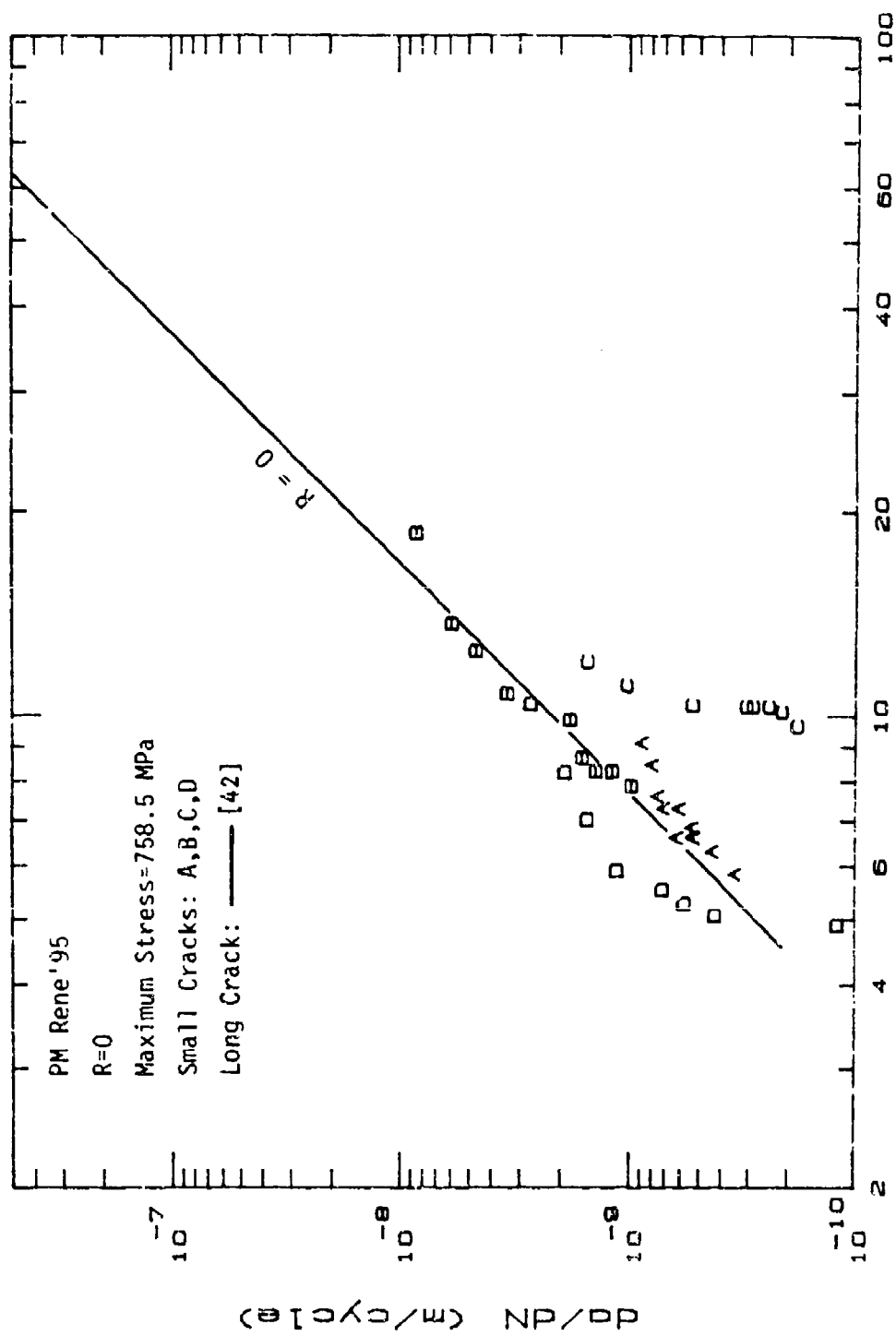


Figure 4.18 Fatigue crack growth rates versus stress intensity factor range for René 95 (PM), tested at 25° C, Max. Stress = 483 MPa,  $R = -1$ .



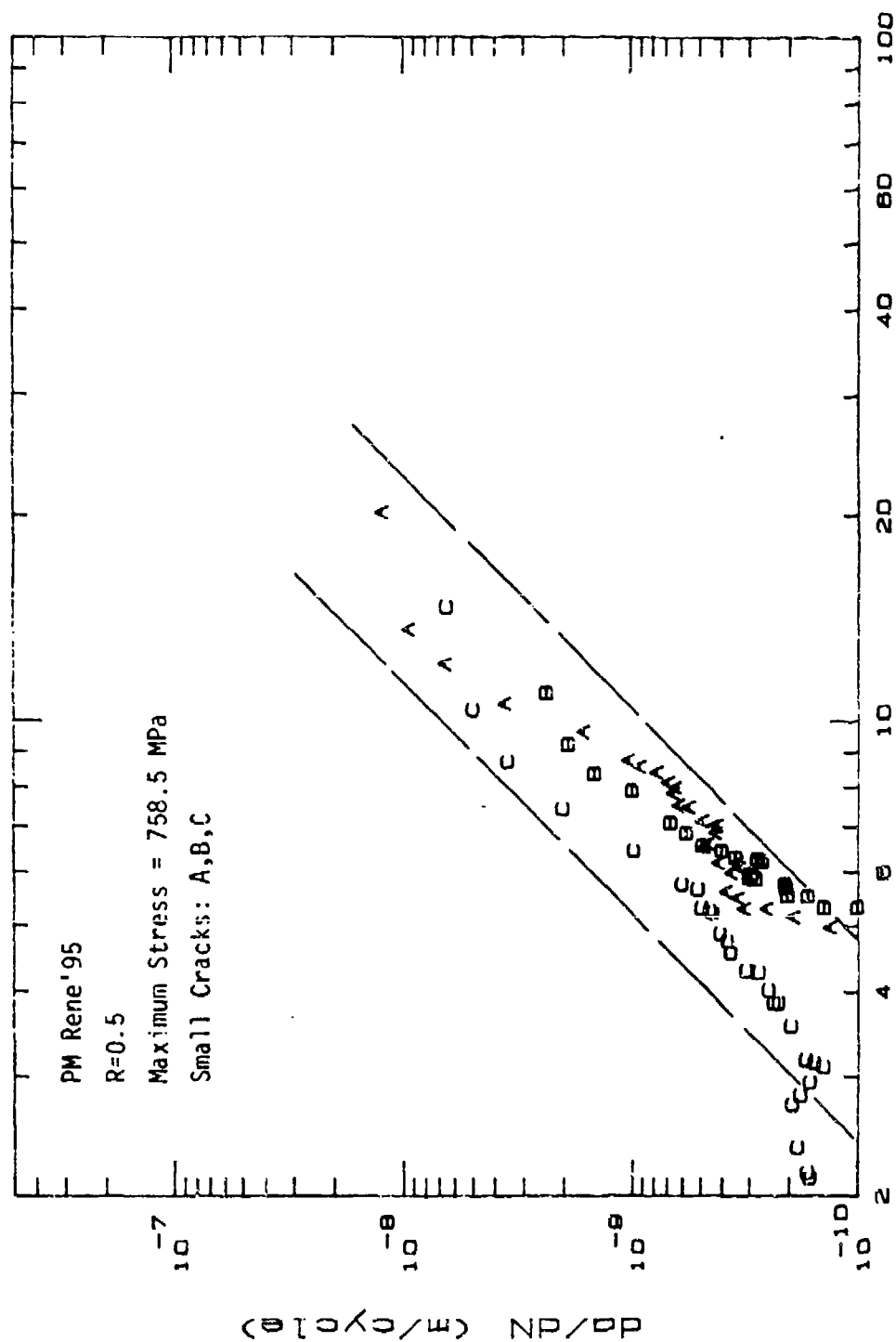
# STRESS INTENSITY FACTOR RANGE $\Delta K$ (MPo $\sqrt{m}$ )

Figure 4.19 Summary of fatigue crack growth rates versus stress intensity factor range for René 95 (PM), tested at 25° C,  $R = -1$ .



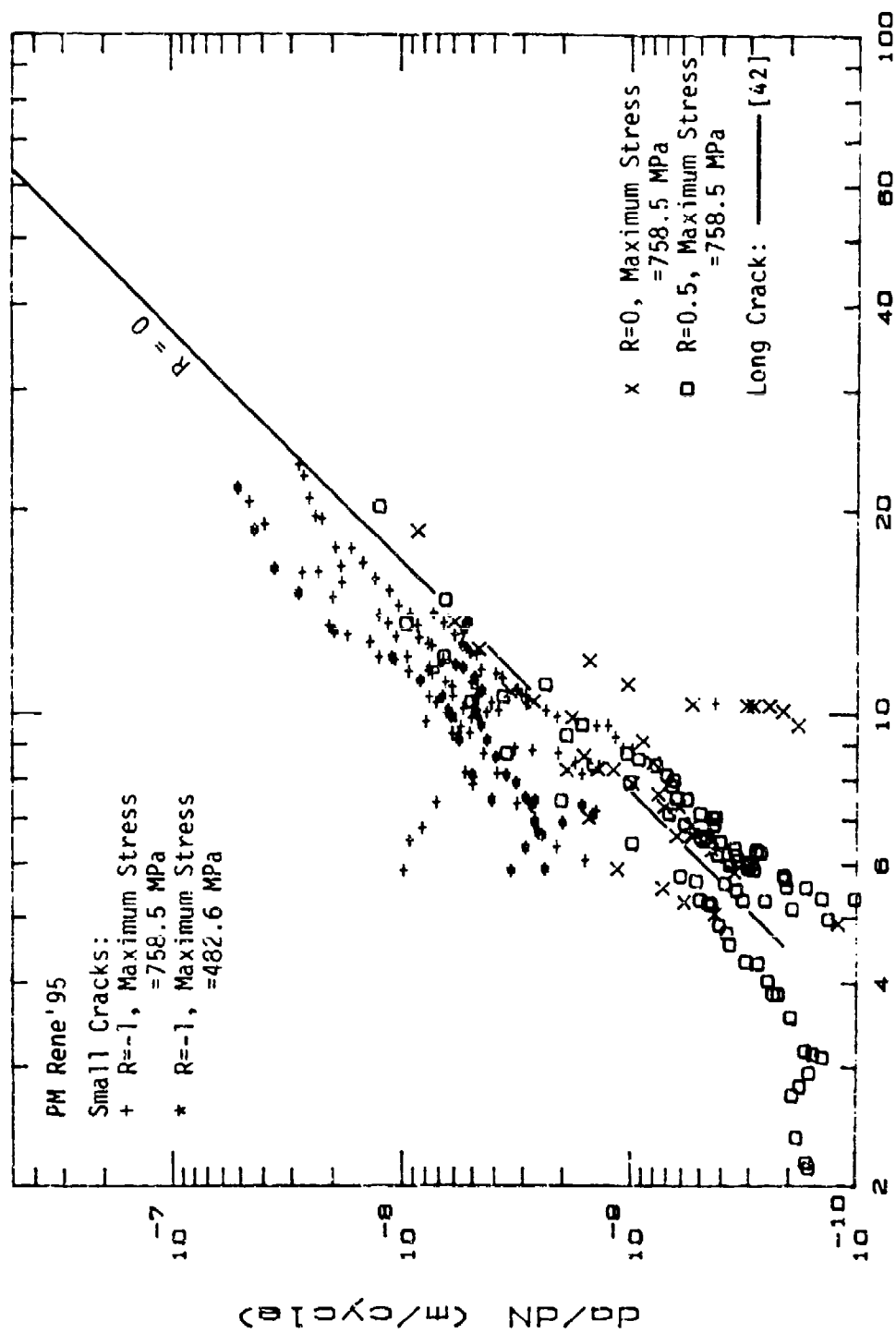
STRESS INTENSITY FACTOR RANGE  $\Delta K$  (MPa $\sqrt{m}$ )

Figure 4.20 Fatigue crack growth rates versus stress intensity factor range for René 95 (PM), tested at 25°C, Max. Stress = 758 MPa,  $R = 0$ .



STRESS INTENSITY FACTOR RANGE  $\Delta K$  (MPa $\sqrt{m}$ )

Figure 4.21 Fatigue crack growth rates versus stress intensity factor range for René 95 (PM), tested at 25°C, Max. Stress = 758 MPa,  $R = 0.5$ .



# STRESS INTENSITY FACTOR RANGE $\Delta K$ (MPa√m)

Figure 4.22 Summary of fatigue crack growth rates versus stress intensity factor range for René 95 (PM), tested at 25° C, Max. Stress and R ratio were varied.



Figure 4.23 Scanning Electron Micrographs of small cracks initiated from an EDM pit in Inconel X-750, tested at 25C

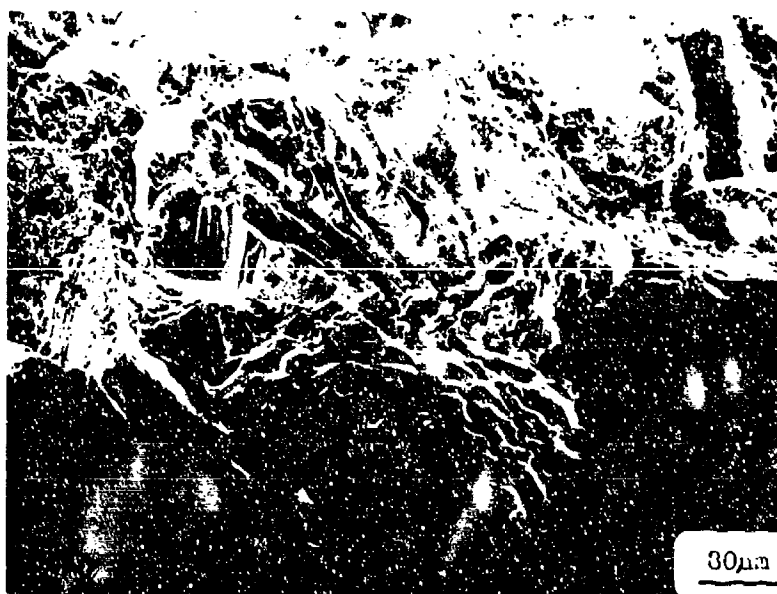


Figure 4.24 Scanning Electron Micrographs of the fracture surface of the small crack in Figure 4.23.





Figure 4.25 Scanning Electron Micrographs of the fracture surface in Inconel X-750 tested at 25° C.

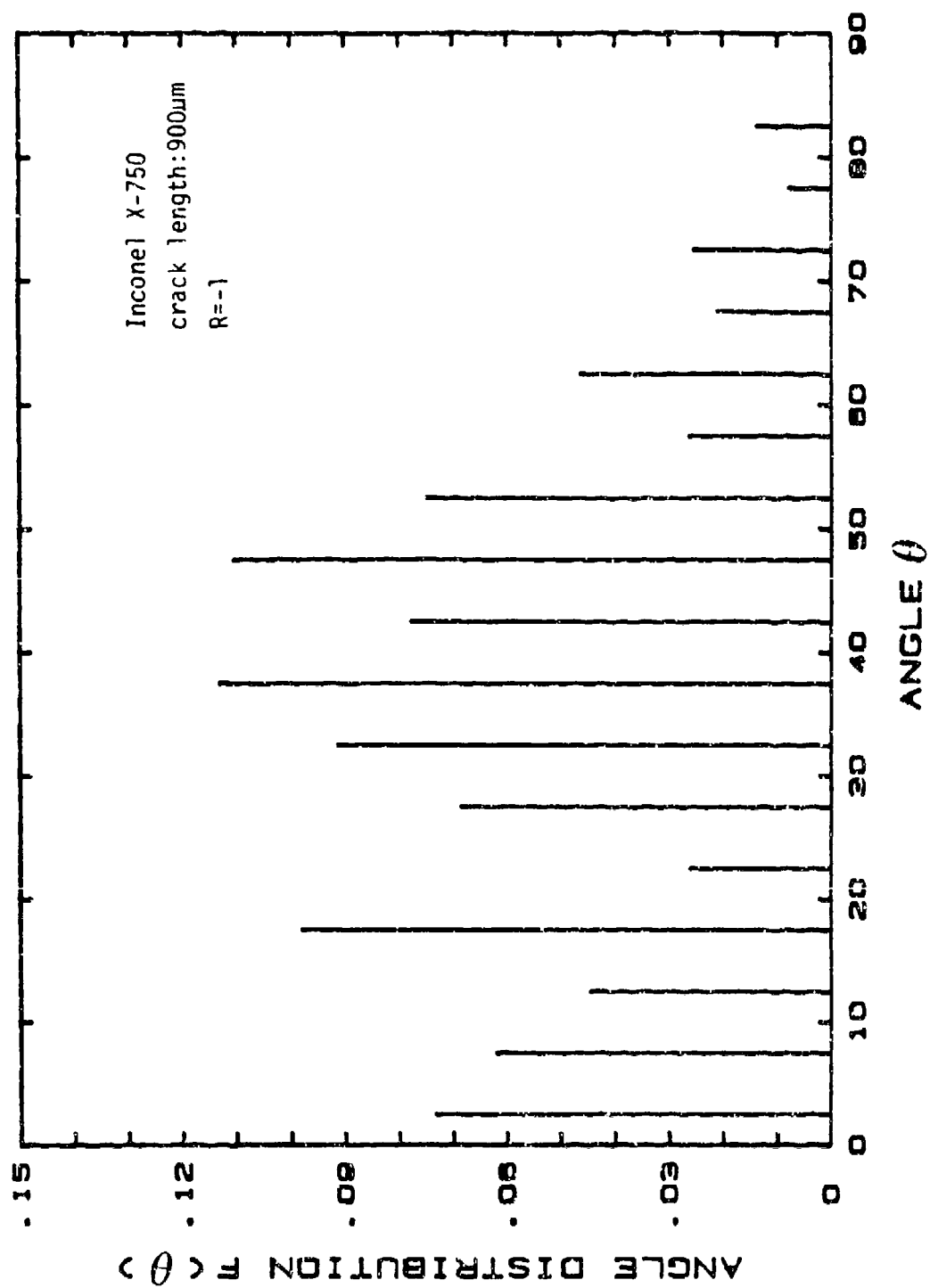
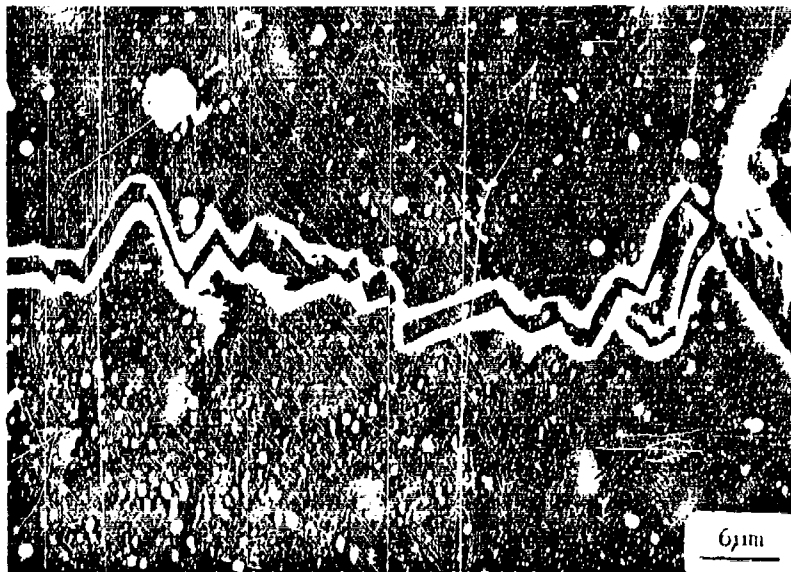
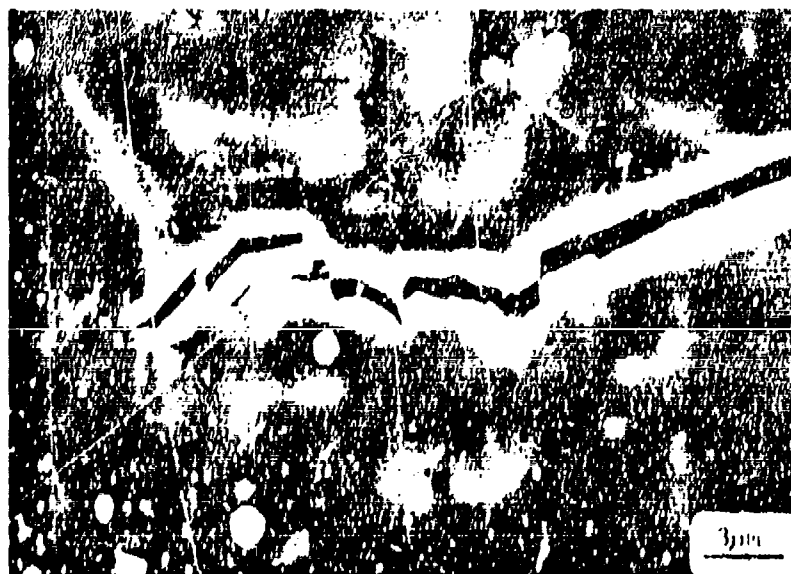


Figure 4.26 Angle distribution spectrum of a small crack with length 900  $\mu\text{m}$  in Inconel X-750, tested at 25°C.



(a)



(b)

Figure 4.27 Scanning Electron Micrographs of a small crack in René 95 (PM) tested at 27°C. a) crack root, b) crack tip



Figure 4.28 Scanning Electron Micrographs of the fracture surface of a small crack in René 95 (PM) tested at 25° C.

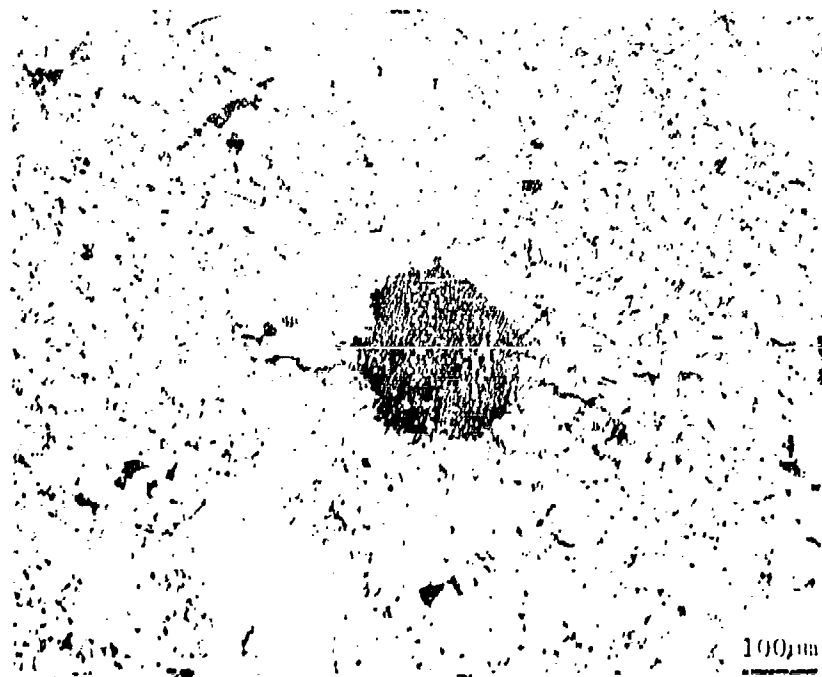


Figure 4.29 Micrograph of small cracks initiated from an EDM pit in Waspaloy tested at 25° C.

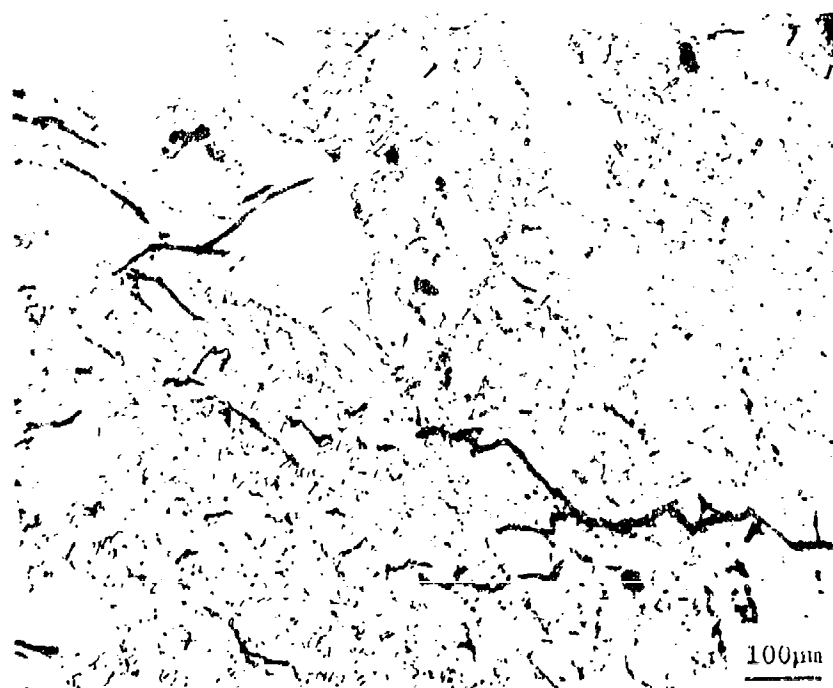


Figure 4.30 Micrographs of fatigue cracks in persistent slip bands in Waspaloy tested at 25° C.

## 4.2 Fatigue Behavior of Small Cracks at Elevated Temperature

Fatigue crack growth rates of small cracks were measured at elevated temperature in Waspaloy, Inconel 718, and IN100 (PM). A summary of testing conditions is given in Table 2.6. Data reductions began with a surface crack length ( $2c$ ) of approximately 200  $\mu\text{m}$ . Based on the determination that  $c/a = 1$  was a valid approximation, data was reported and evaluated in terms of crack depth,  $a$ . Data is presented here as crack depth versus cycle number and crack growth rate versus stress intensity factor range. Crack growth rates were determined using the seven point incremental polynomial method unless otherwise specified.

Trends in long crack data were taken from the literature. Care was taken to consider equivalent materials and testing conditions. Differences in the fatigue behavior of small cracks ( $a > 100 \mu\text{m}$ ) and long crack trends did not justify generating long crack data.

### 4.2.1 Waspaloy, 427° C

The fatigue behavior of small cracks in Waspaloy was investigated at 427° C (800° F). All tests were performed under load control on specimens with round gauge section (Figure 2.5). The principal test variables were maximum stress and R-ratio.

The effect of the maximum stress on small crack growth rates is shown in Figure 4.31 through Figure 4.36. Values of the maximum stress employed were 504 MPa (73 Ksi), 621 MPa (90 Ksi) and 754 MPa (109 Ksi). Crack depth versus cycle number is presented first for each test, then  $da/dN$  versus  $\Delta K$ . The stress ratio was constant at  $R = -1$ . Crack growth rates versus  $\Delta K$  curves are consolidated in Figure 4.37 for these three tests.

The value of maximum stress under fully reversed,  $R = -1$ , elastic cycling was shown to have no effect on the upper bound crack growth rates of small cracks as shown in

Figure 4.37. This upper bound trend is precisely coincident with long crack results taken from the work of Larsen et al [39]. Maximum stresses employed in testing are approximately 50%, 60% and 75% of the 0.2% yield strength. This is a particularly interesting outcome when one considers that the stress intensity factor defines the near-crack-tip elastic stress field. In these experiments, the far field stress is greater than 50% of the magnitude of stresses in the crack tip field.

The only apparent anomalous behavior observed in  $da/dN$  versus  $\Delta K$  curves is crack growth rates which fall notably below the long crack trend. Consider, for example, crack-B in Figure 4.32 for which  $da/dN$  first decreases and then increases below the long crack trend. By examining the  $a$  versus  $N$  curve for crack B in Figure 4.31, this behavior represents only a slight perturbation in crack extension and is attributable to the non-uniform nature of the Waspaloy microstructure.

The effect of R-ratio on small crack growth rates is shown in Figure 4.35 through Figure 4.43. Values of stress ratio employed were:  $R = -1$ ,  $R = 0$ ,  $R = 0.3$  and  $R = 0.5$ . The maximum stress was 758 MPa (110 Ksi) in all tests except the  $R = 0.5$  test where the maximum stress was necessarily increased to 903 MPa (130 Ksi). Crack growth rates versus  $\Delta K$  curves were consolidated in Figure 4.44 for these four tests with the expected results.

For positive R-ratios, the ordering of crack growth rates from high to low corresponded to R values of 0.5, 0.3, and 0, respectively. This R-ratio effect is generally explained in terms of crack closure. The true crack driving force is then  $\Delta K_{eff} = K_{max} - K_{op}$ , where  $K_{op}$  is the stress intensity factor at which the crack flanks are fully open. In this program, the nominal value of  $\Delta K = K_{max} - K_{min}$  (for  $K_{min} \geq 0$ ) was used in presenting data since  $K_{op}$  was not measured directly. For high R-ratios, the nominal value of  $\Delta K$  is approximately equal to  $\Delta K_{eff}$  since crack flanks would be open at

all values of load in the cycle. At low R-ratios, the nominal value of  $\Delta K$  is greater than  $\Delta K_{eff}$ , therefore, crack growth rates for  $R = 0$  are shifted to the right.

The  $R = -1$  results fall closer to the  $R = 0.5$  results than they do to the  $R = 0$  results which have the equivalent nominal value of  $\Delta K$  for any crack length. The maximum stress was 758 MPa in both tests. The higher crack growth rates in the  $R = -1$  tests can be attributed to a greater amount of crack tip strain reversal which promotes crack extension. The same ordering of crack growth rates as a function of R-ratio was found in the Inconel X-750 results.

The effect of temperature (427 C vs. 25C) on the crack growth rates of small cracks can be seen in Figures 4.45 and 4.46 for  $R = -1$  and  $R = 0$ , respectively. In both cases, crack growth rates were higher in the elevated temperature tests. This could be a result of a deleterious environmental interaction or a decrease in the closure stress experienced at 427C. The 427C tests exhibited less crystallographic faceting on fracture surfaces as determined by stereoscopic observations. This would result in less roughness induced closure and, therefore, higher crack growth rates.

Crack growth at lower values of  $\Delta K$  at  $R = 0$  in room temperature tests is a result of a "short crack effect" in the room temperature tests. Crack lengths were  $< 100 \mu m$  in many room temperature tests.

In summary, the fatigue behavior for small cracks ( $a > 100 \mu m$ ) in Waspaloy at 427C exhibited a general absence of a "short crack effect" over a range of test conditions. More specifically, the crack driving force could be characterized in terms of  $\Delta K$  with upper bound crack growth rates coincident with long crack results.



#### 4.2.2. Inconel 718, 427° C

The fatigue behavior of small cracks in Inconel 718 was investigated at 427° C (800° F). All tests were performed under load control on specimens with two flats as shown in Figure 2.6. Unfortunately, this drawing was not strictly followed in the machining of six Inconel 718 specimens. The radii-to-flats were made smaller at 6.35 mm rather than the designated 12.7 mm. Consequently, three tests failed prematurely at this location. An attempt was made to salvage whatever information could be saved from these tests. The principal test variables were maximum stress and R-ratio.

The effect of maximum stress on small crack growth rates can be seen in Figures 4.47 through Figure 4.50. Values of maximum stress were 621 MPa (90 Ksi) and 758 MPa (110 Ksi). The stress ratio was constant at  $R = -1$ . Crack growth rates versus  $\Delta K$  curves are consolidated in Figure 4.51 for these two tests. There is good correlation of  $da/dN$  with  $\Delta K$  at high values of  $\Delta K$  (longer crack lengths). However, a tendency towards nearly constant crack growth rates occurs at low values of  $\Delta K$ . This behavior is more clearly evident in the  $a$  versus  $N$  curves for these tests shown in Figure 4.47 and Figure 4.49. These  $a$  versus  $N$  curves could be fitted with a straight line ( $da/dN = \text{constant}$ ) for all values of  $a < 300 \mu\text{m}$ .

The  $R = 0.05$  test results for small cracks (Figures 4.52 and 4.53) were found to be nearly coincident with the long crack trend as seen in Figure 4.53. The long crack results were taken from the work of Knueger [40]. The deviation from long crack behavior may be attributed to the coarse heterogeneous microstructure which offers a variable resistance to crack extension or to a lack of mechanical similitude at small crack sizes.

The effect of R-ratio on small crack growth rates is shown in Figure 4.49 through Figure 4.43. Values of the stress ratio employed were  $R = -1$  and  $R = 0.05$ . The maximum stress was 753 MPa (110 Ksi). Crack growth rates versus  $\Delta K$  curves were

consolidated in Figure 4.54 for the two tests. Similar to the Inconel X-750 and Waspaloy results, the general trend for higher crack growth rates at  $R = -1$  versus  $R = 0.05$  was also seen in Inconel 718.

In summary, the fatigue behavior of small cracks in Inconel 718 exhibited an absence of a "short crack" effect when the maximum stress was low. The crack driving force could be characterized in terms of  $\Delta K$ . When the maximum stress was high, constant crack growth rates were observed over the initial regime (100  $\mu\text{m}$  to 300  $\mu\text{m}$ ) of crack extension.

#### 4.2.3 IN100 (PM), 649° C

The fatigue behavior of small cracks in powder metallurgy IN100 was investigated at 649° C (1200° F). All tests were performed on the modified specimen shown in Figure 2.6. Test results on Waspaloy and Inconel 718 established the basic conclusion that ; for small cracks (  $a > 100 \mu\text{m}$ ) the upper bound of crack growth rates could generally be characterized in terms of  $\Delta K$  and consolidated with long crack data. The only suggestion of anomolous behavior occurred when crack depth was small ( $100 \mu\text{m} < a < 300 \mu\text{m}$ ) and the maximum stress approached the cyclic yield strength of the material.

Therefore, it was decided that the IN100 investigation would focus on the fatigue behavior of small cracks under elastic-plastic cycling conditions which are relevant to cracking in notch locations of turbine disks such as bolt holes and blade attachments. The aim of the IN100 study is to develop baseline data under fully reversed, continuous cycling conditions ( $\epsilon_{\text{min}}/\epsilon_{\text{max}} = -1$ ) as well as consider disk relevant strain ranges with hold times. A few results from this ongoing study are reported here. Tests were performed in load control and strain control.

One load control test was performed under nominally elastic conditions. The maximum stress was 758 MPa (110 Ksi) and  $R = 0.1$ . Results are reported in Figure 4.55 and Figure 4.56. The fatigue crack growth rates of small cracks ( $a > 100 \mu\text{m}$ ) in IN100 were coincident with the long crack trend as shown in Figure 4.56. Long crack results were taken from the work of Larsen et al [29].

Under strain controlled cycling, one condition considered was a total strain range of 0% to 0.80%. The first hysteresis loop is shown in Figure 4.57. After an initial plastic yielding, the cycling was nominally elastic. The average maximum stress was 1100 MPa. The test was maintained in strain control throughout. The results are presented in Figures 4.58 and 4.59. Crack growth rate is correlated with  $\Delta K$  in Figure 4.59. Similar to other

tests where the maximum stress was high, the crack growth rate was nearly constant up to a crack depth of 300  $\mu\text{m}$  beyond which results merge with the long crack trend.

A fully reversed strain controlled test with  $\epsilon_{\text{min}}/\epsilon_{\text{max}} = -1$  was performed. The total strain range was  $\pm 0.55\%$ . A typical hysteresis loop is shown in Figure 4.60. A plastic strain range of 0.08% was measured at zero load. The average value of the maximum stress was 1026 MPa. The results are presented in Figure 4.61 and Figure 4.62. Although linear elastic fracture mechanics is invalid under these conditions, crack growth rates are plotted in terms of  $\Delta K$  in Figure 4.62 for the sake of comparison.  $\Delta K$  was calculated using the average value of the maximum stress. Representing the crack driving force in terms of  $\Delta J$  would be more appropriate for this test. However, at this time, we have an insufficient characterization of the cyclic stress-strain response to make an accurate estimate of  $\Delta J$ .

The results for the above three tests are plotted together in Figure 4.63. Crack growth rates under elastic-plastic cycling are approximately three times greater than the long crack trend. It is interesting to note a convergence of the two strain control test results at the lower range of  $\Delta K$  where  $a \approx 100 \mu\text{m}$  in both tests. This result suggests that near-surface elements in the 0 - 0.80% test specimen may have experienced elastic-plastic cycling due to a lack of constraint at the free surface. This may also have been true in some of the Inconel 718 tests where the maximum stress was high.

#### 4.2.4 Fractography, Elevated Temperature Tests

As previously discussed, specimen separation was achieved by high frequency cycling at room temperature after surface crack lengths exceed 2 mm. Fracture surfaces were first examined and photographed using an optical stereoscopic microscope to characterize crack front profiles and general macroscopic features. Fracture surfaces were

further examined by scanning electron microscopy. Sides of specimen gauge sections were also examined by SEM and optical microscopy.

#### Waspaloy, 427° C

An optical fractograph of a typical Waspaloy specimen is shown in Figure 4.64a. The fracture path is nominally perpendicular to the specimen axis with the exception of near surface regions beyond a surface crack length of  $\sim 600 \mu\text{m}$  where the crack deflects out of plane. This was suspected to be related to the curvature of the specimen surface. Consequently, the specimen geometry was modified (Figure 2.6) to include two flats from which cracks were initiated. This solved the crack deflection problem. This crack deflection is believed to have caused some deviation from  $c/a = 1$ . Although accounting for this slight change in geometry may be tractable, it did not manifest itself in the crack growth behavior. Therefore, data reduction was carried out in the manner described in a previous section.

Typical fracture surface features for Waspaloy can be seen in Figure 4.64b. The fracture path is transgranular and similar to that observed for room temperature tests. However, fatigue fracture paths in room temperature tests exhibited greater deviation from the nominal fracture plane than was observed in 427° C tests.

#### Inconel 718, 427° C

The fatigue fracture path for small cracks in Inconel 718 are shown in Figure 4.65. Figure 4.65a is an optical micrograph of a laser defect and crack trace at the gauge section surface. Figure 4.65b. is an SEM micrograph of the fracture surface. Both exhibit a transgranular fracture path. Fatigue striations are evident on the fracture surface.

IN100 (PM) 649° C

A SEM micrograph of a typical fracture surface for IN100 is shown in Figure 4.66a. The fracture path is transgranular with crystallographic facets often terminating at grain boundaries.

Figure 4.66b. is an SEM micrograph of the surface of a specimen gauge section after 150 cycles of strain controlled cycling at a total strain range of 0% to 0.80%. A microcrack is emanating from a 10  $\mu\text{m}$  diameter pore, typical of many found in gauge section surfaces in this alloy. Crack propagation from these sites is responsible for the fatigue failure of smooth specimens. Future efforts will be directed at measuring crack growth rates from these pores.

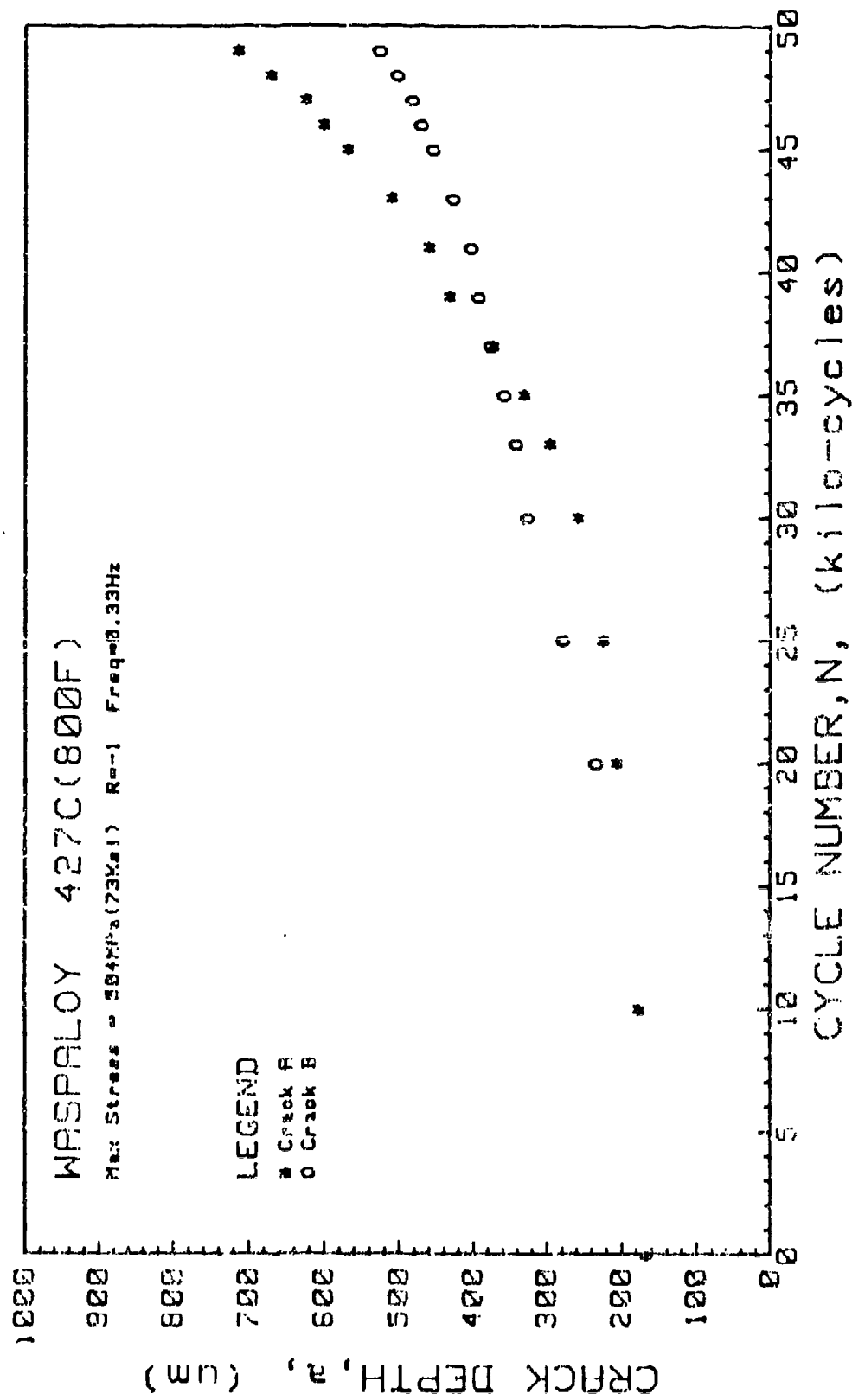


Figure 4.31 Crack depth versus cycle number for Waspalloy tested at 427C,  
Max. stress = 504 MPa, R = -1, Freq. = 0.33 Hz

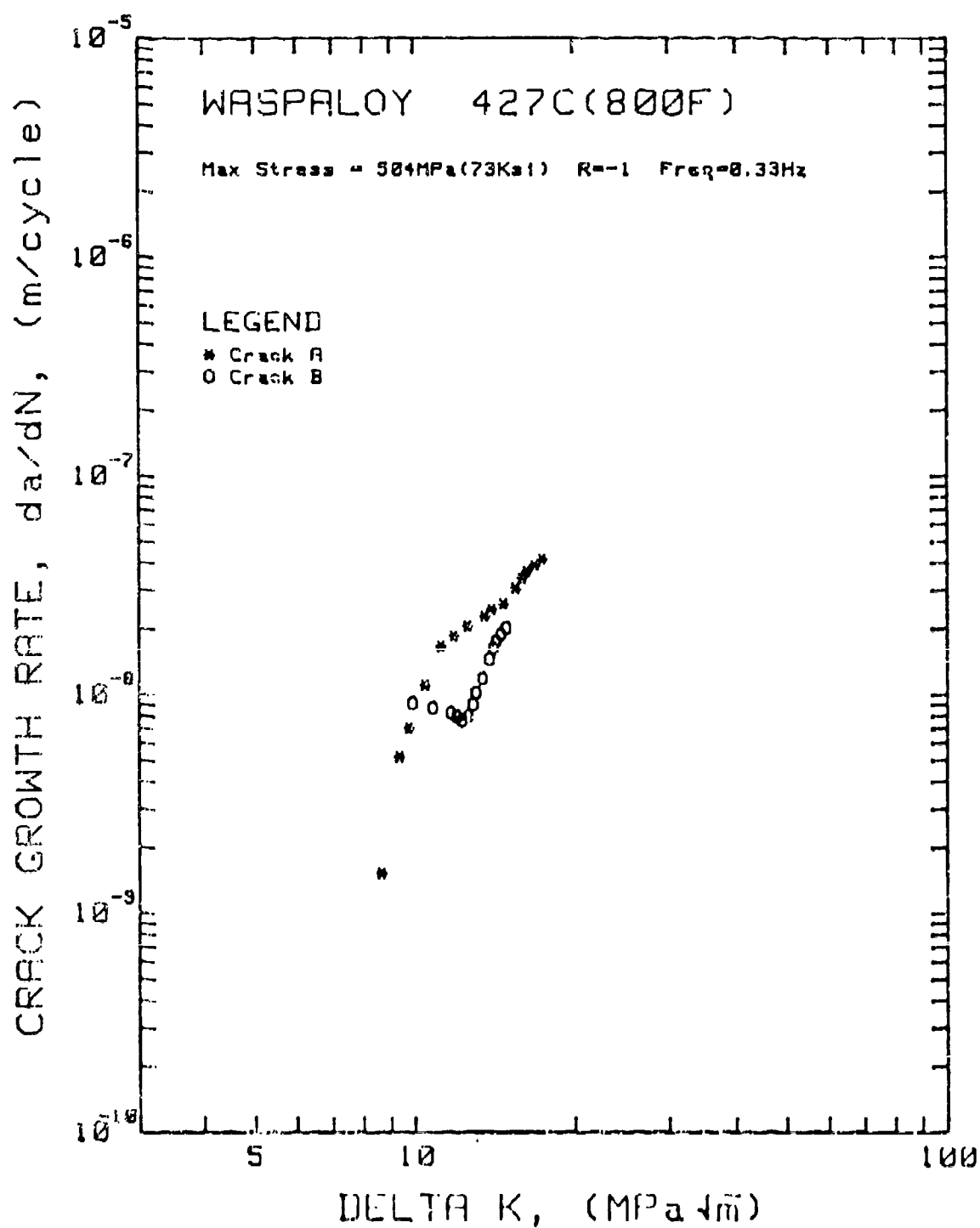


Figure 4.32 Crack growth rate versus stress intensity factor range for Waspaloy tested at 427° C, Max. Stress = 504 MPa, R = -1, Freq. = 0.33 Hz.



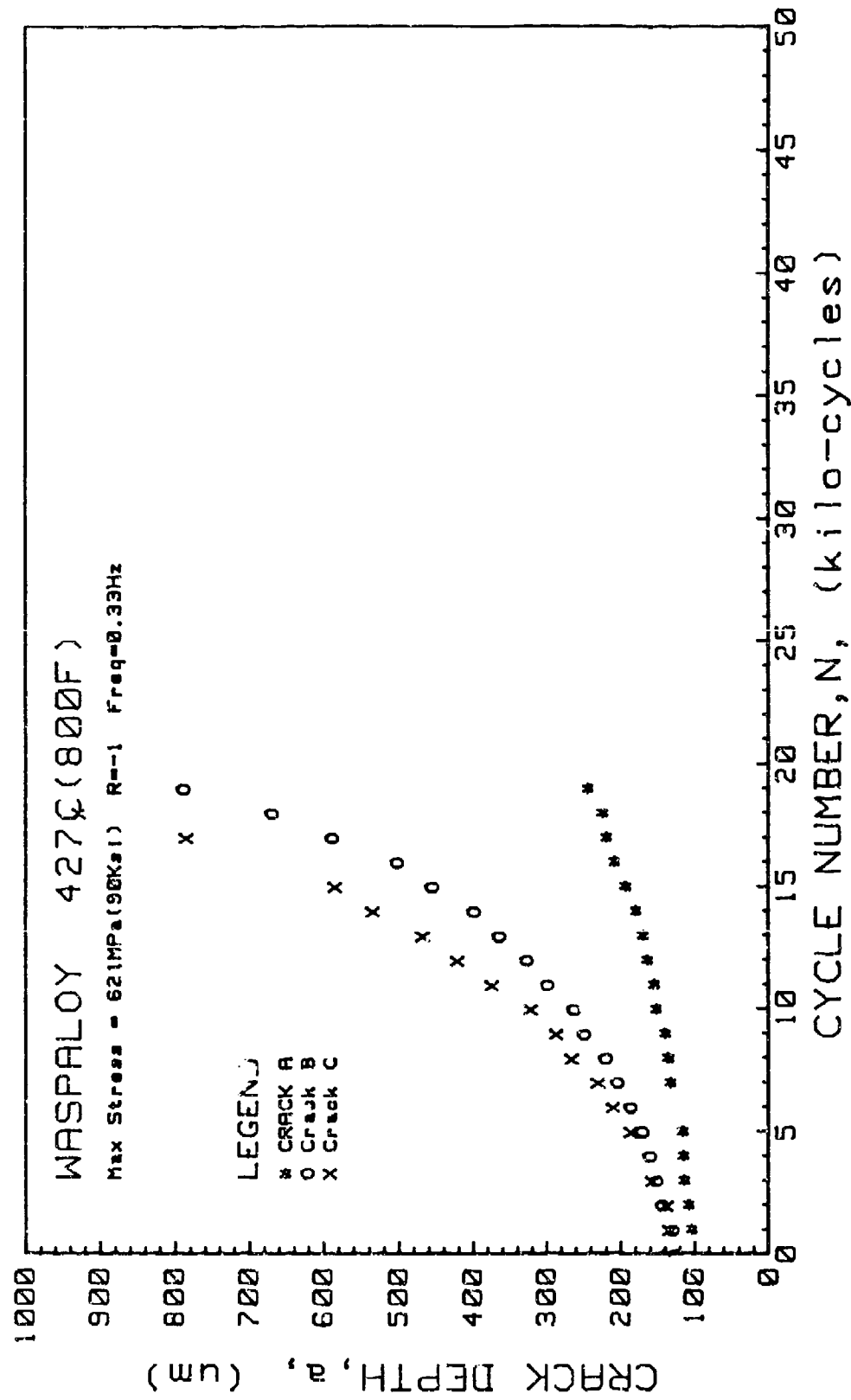


Figure 4.33 Crack depth versus cycle number for Waspalloy tested at 427° C, Max. Stress = 621 MPa, R = -1, Freq. = 0.33 Hz.

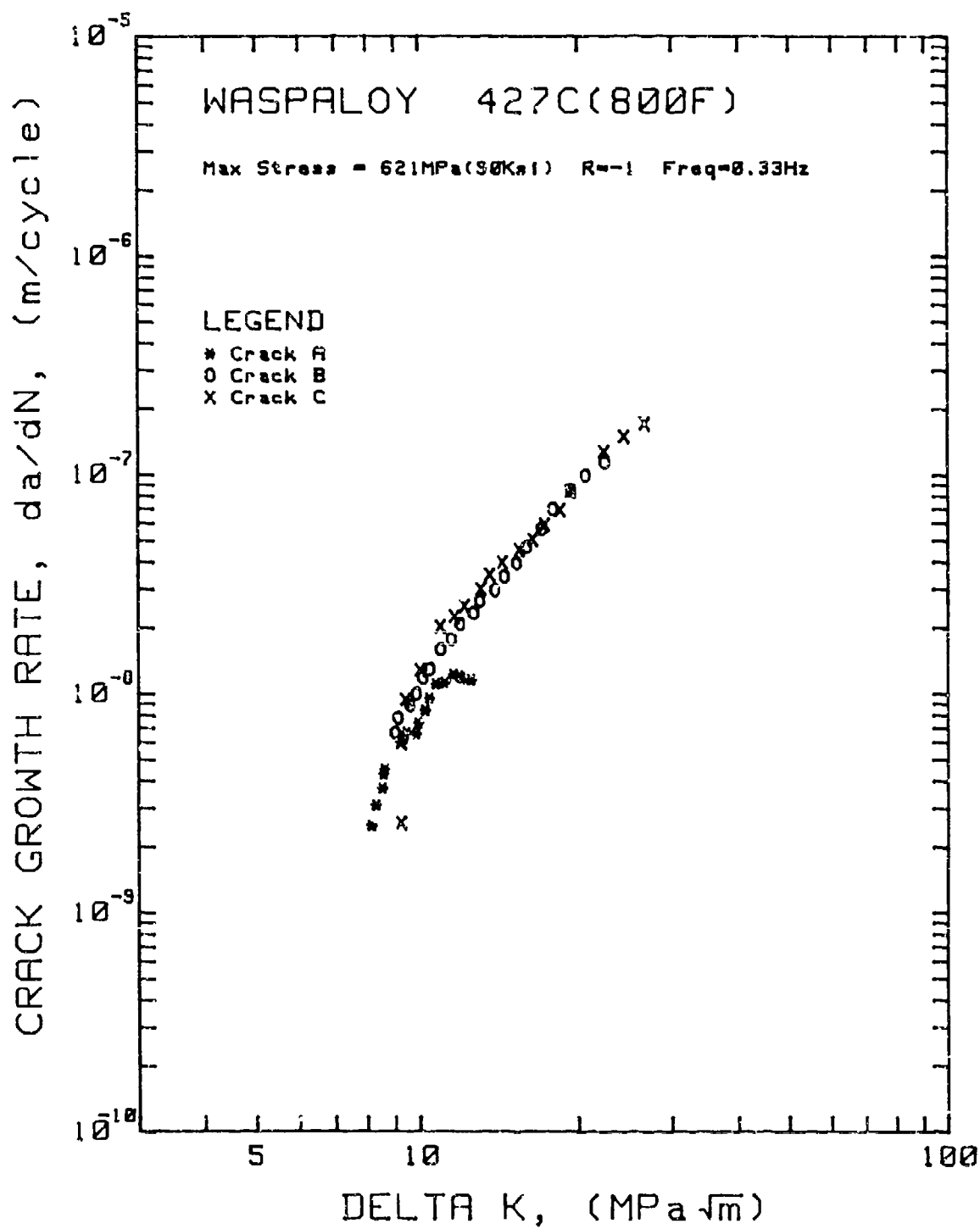


Figure 4.34 Crack growth rate versus stress intensity factor range for Waspaloy tested at 427°C, Max. Stress = 621 MPa, R = -1, Freq. = 0.33 Hz.

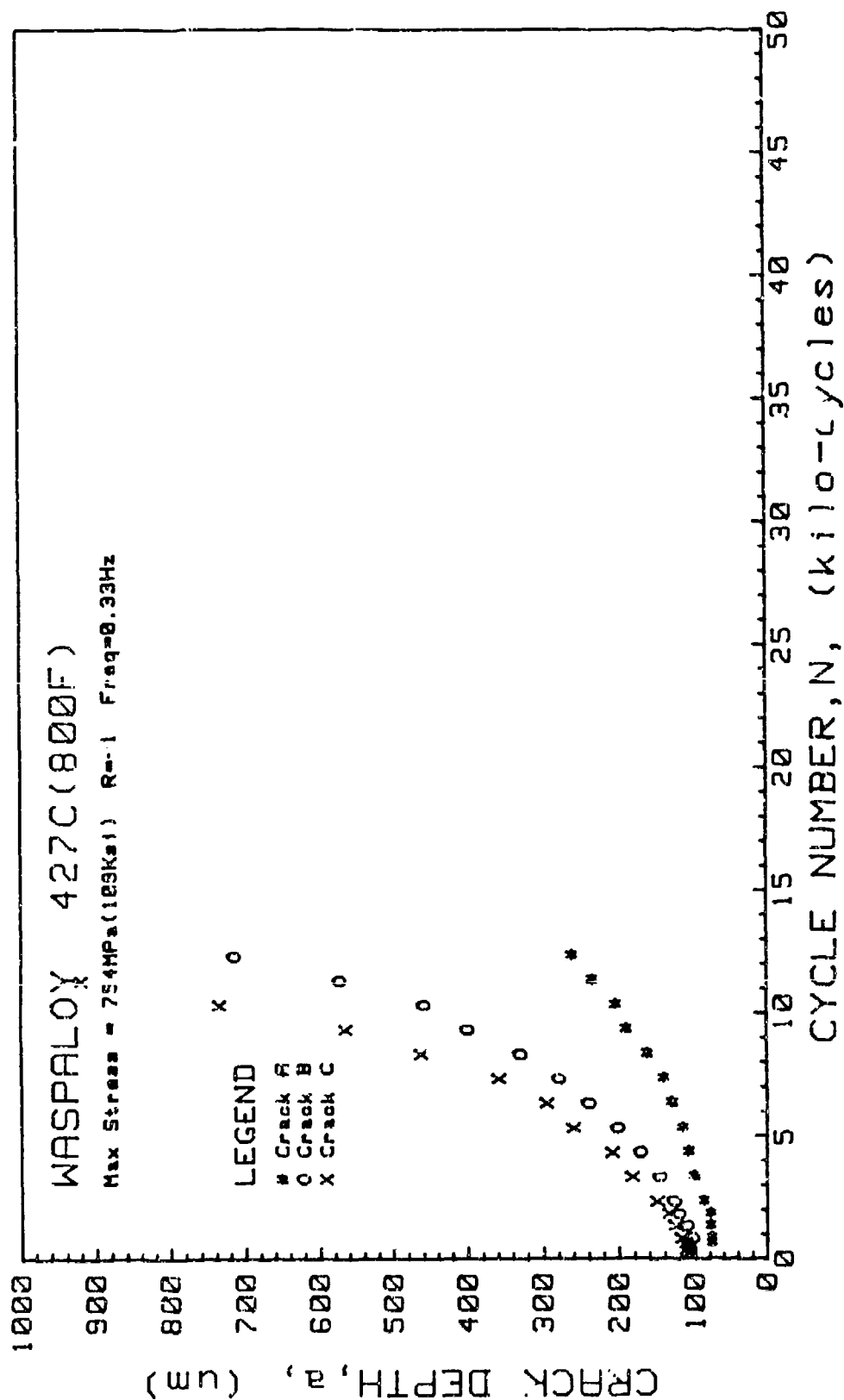


Figure 4.35 Crack depth versus cycle number for Waspaloy tested at 427° C, Max. Stress = 754 MPa, R = -1, Freq. = 0.33 Hz.

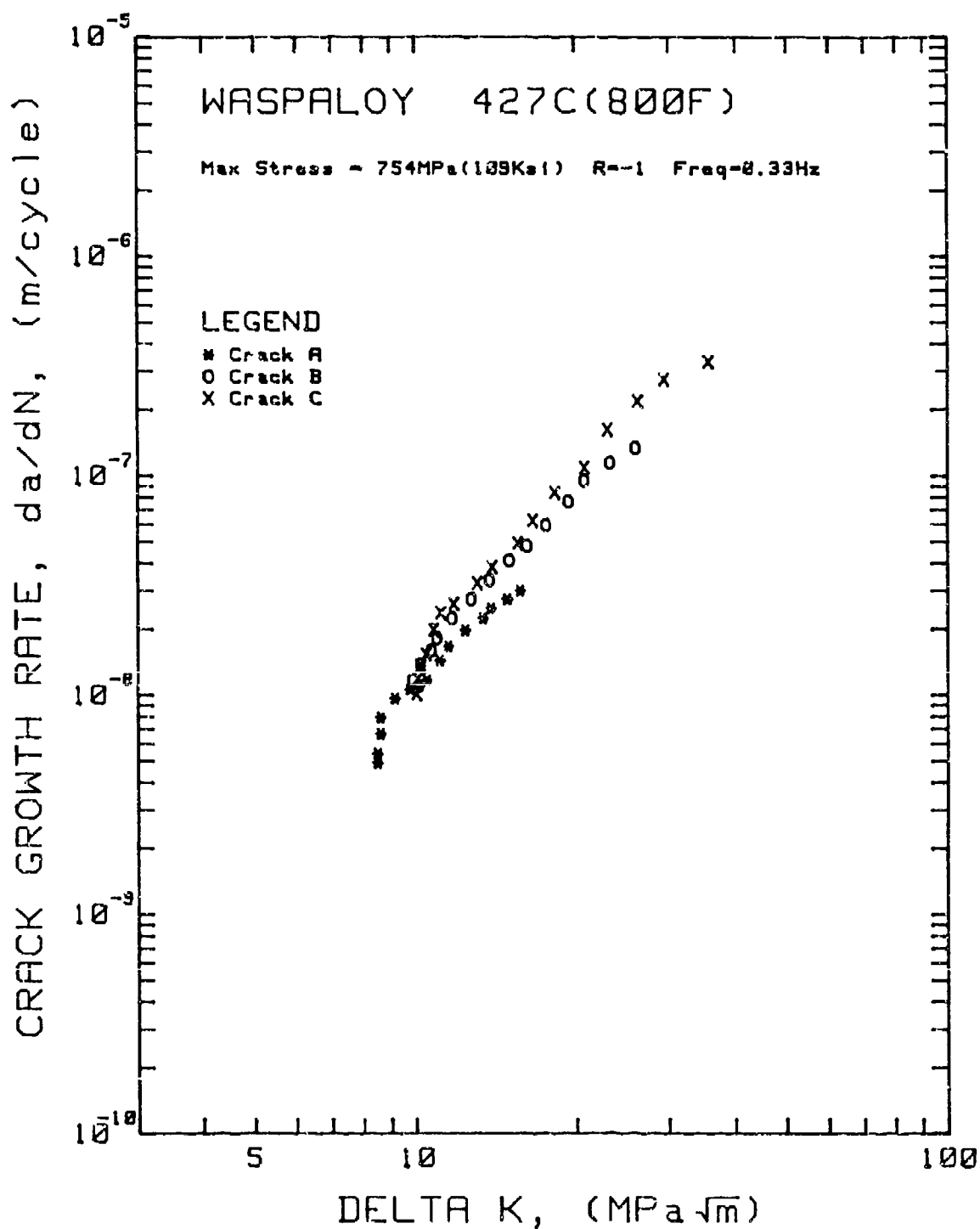


Figure 4.36 Crack growth rate versus stress intensity factor range for Waspaloy tested at 427° C, Max. Stress = 754 MPa, R = -1, Freq. = 0.33 Hz.

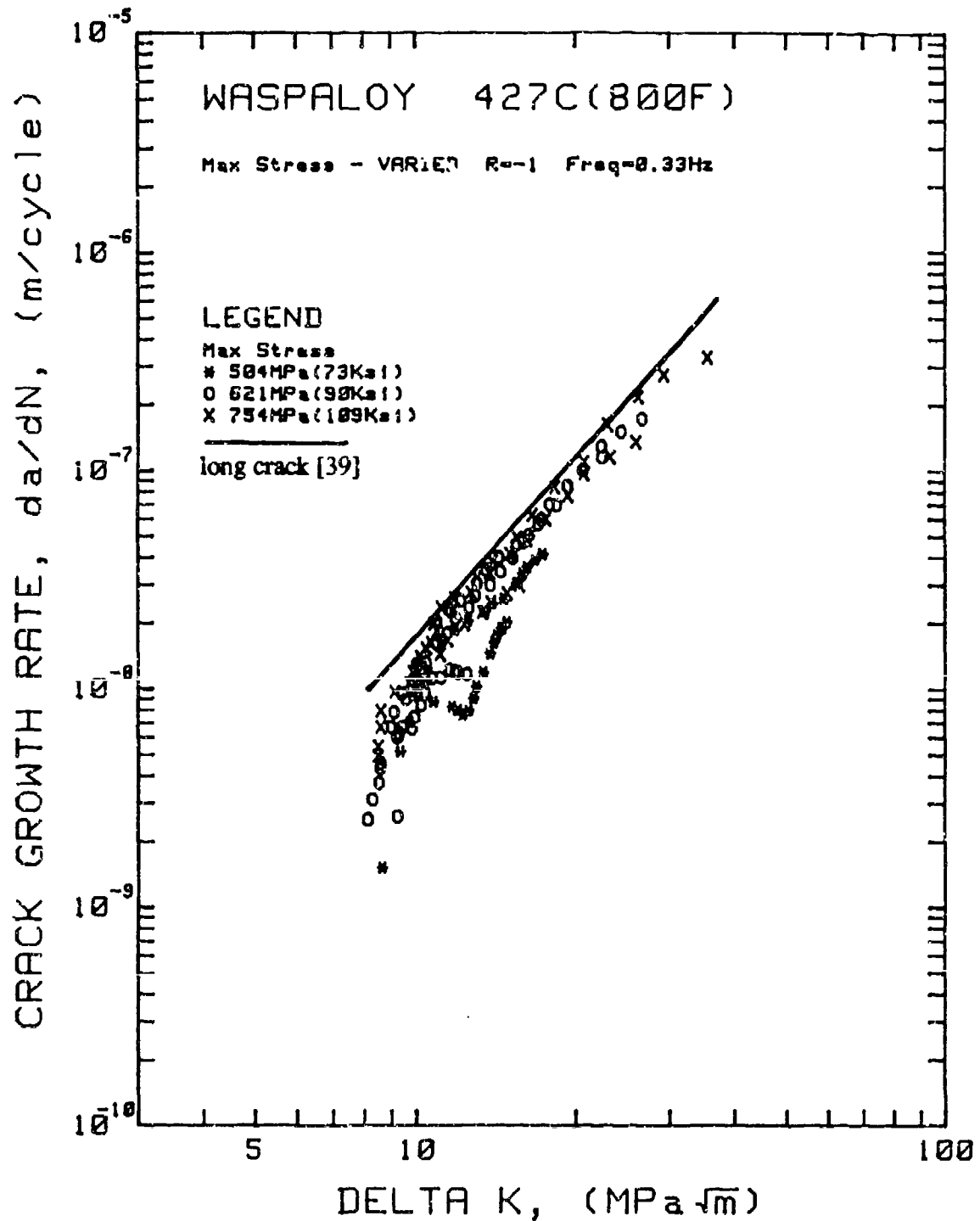


Figure 4.37 Summary of crack growth rate versus stress intensity factor range for Waspaloy tested at 427° C, Max. Stress was varied with R = -1, Freq. = 0.33 Hz.

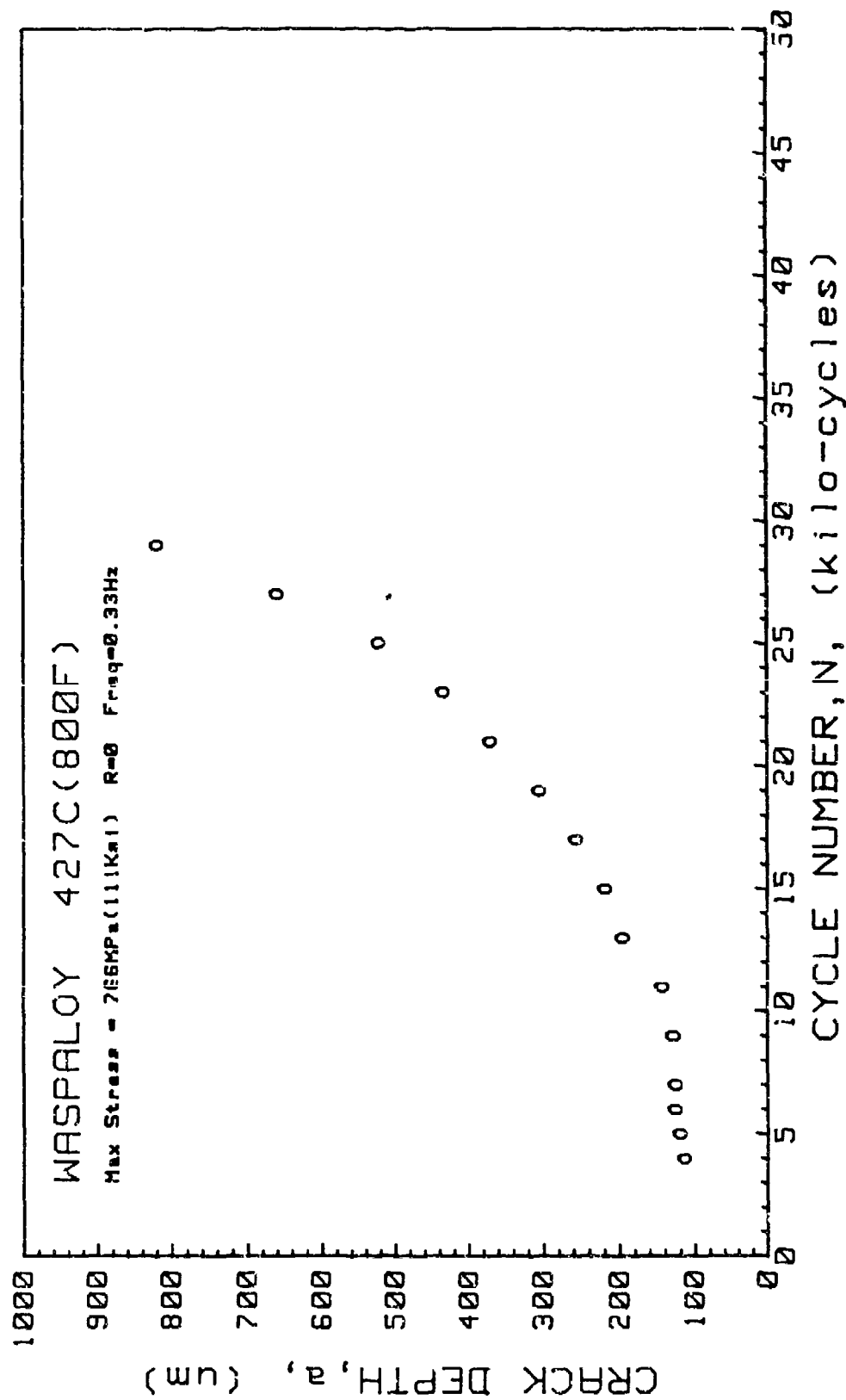
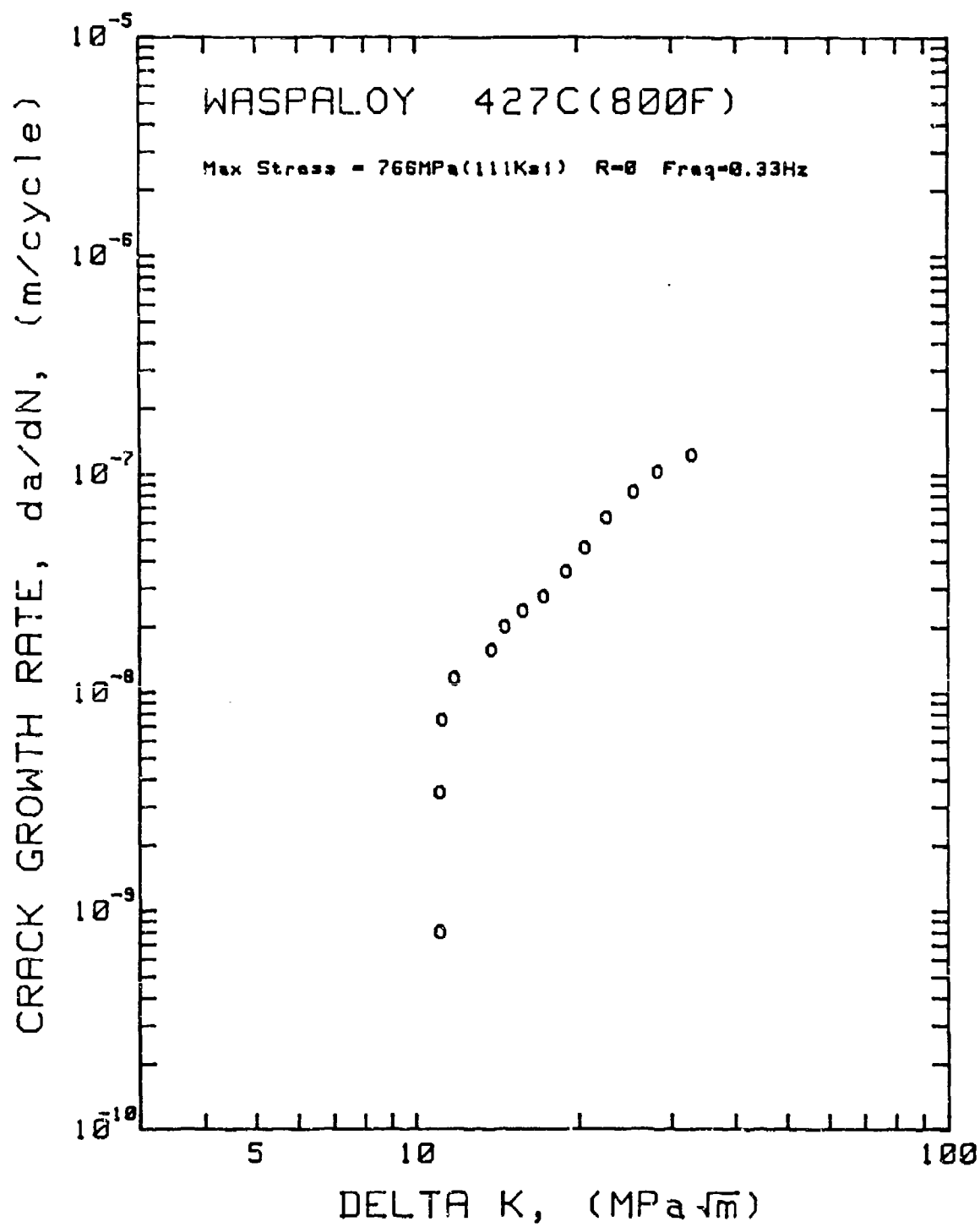


Figure 4.38 Crack depth versus cycle number for Waspalloy tested at 427° C, Max. Stress = 766 MPa, R = 0, Freq. = 0.33 Hz.



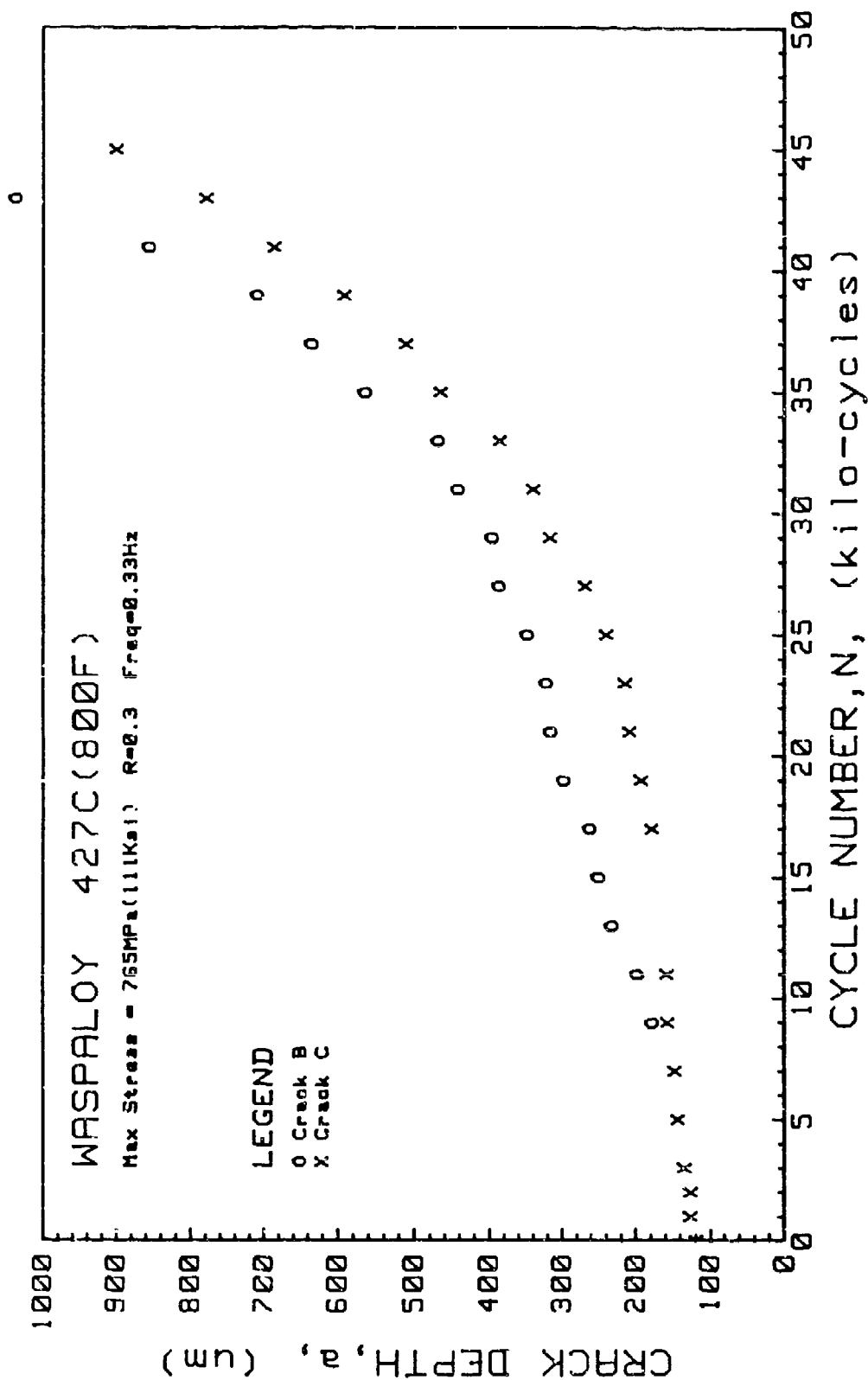


Figure 4.40 Crack depth versus cycle number for Waspalloy tested at 427° C, Max. Stress = 765 MPa, R = 0.3, Freq. = 0.33 Hz.



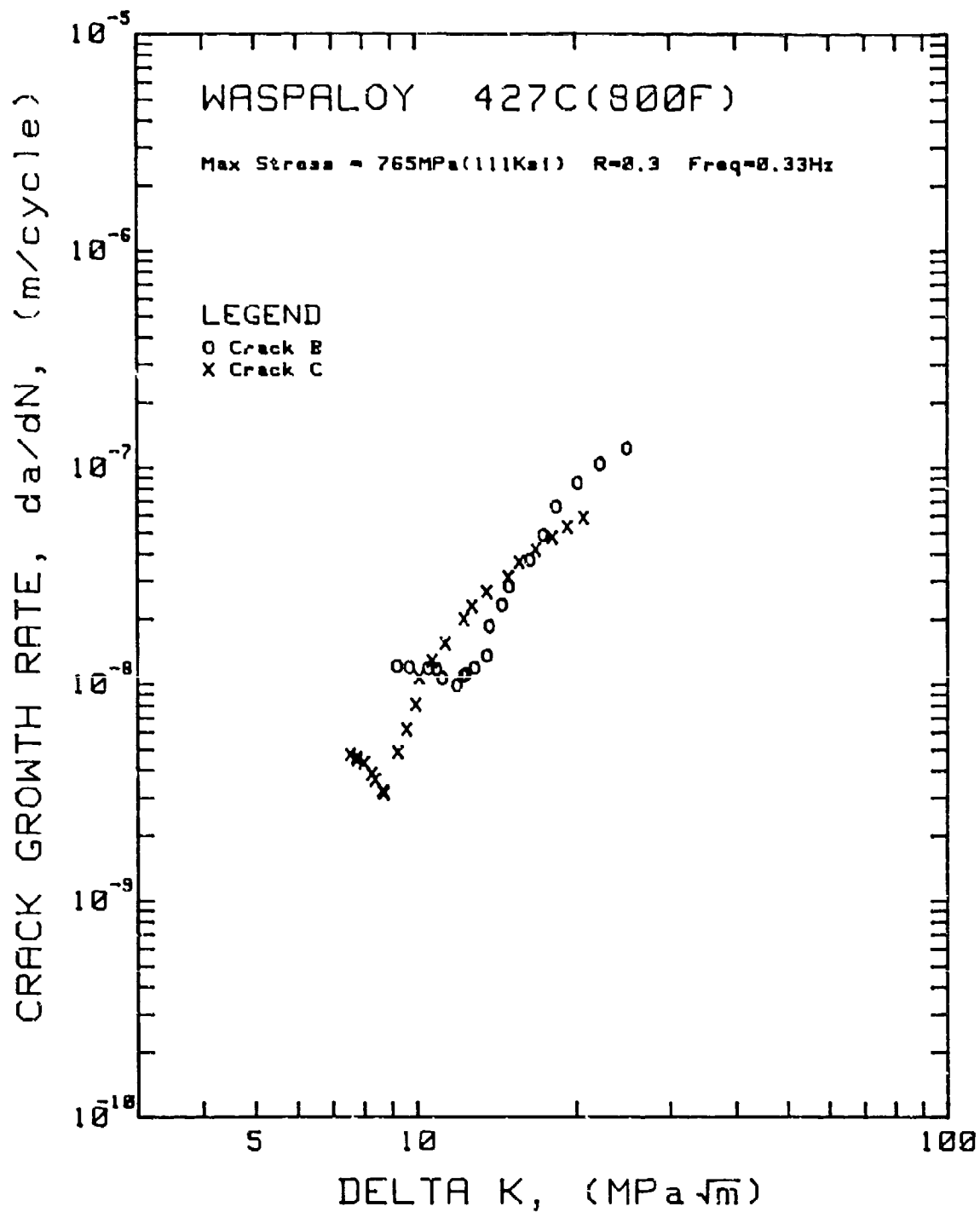


Figure 4.41 Crack growth rate versus stress intensity factor range for Waspaloy tested at 427° C, Max. Stress = 765 MPa, R = 0.3, Freq. = 0.33 Hz.

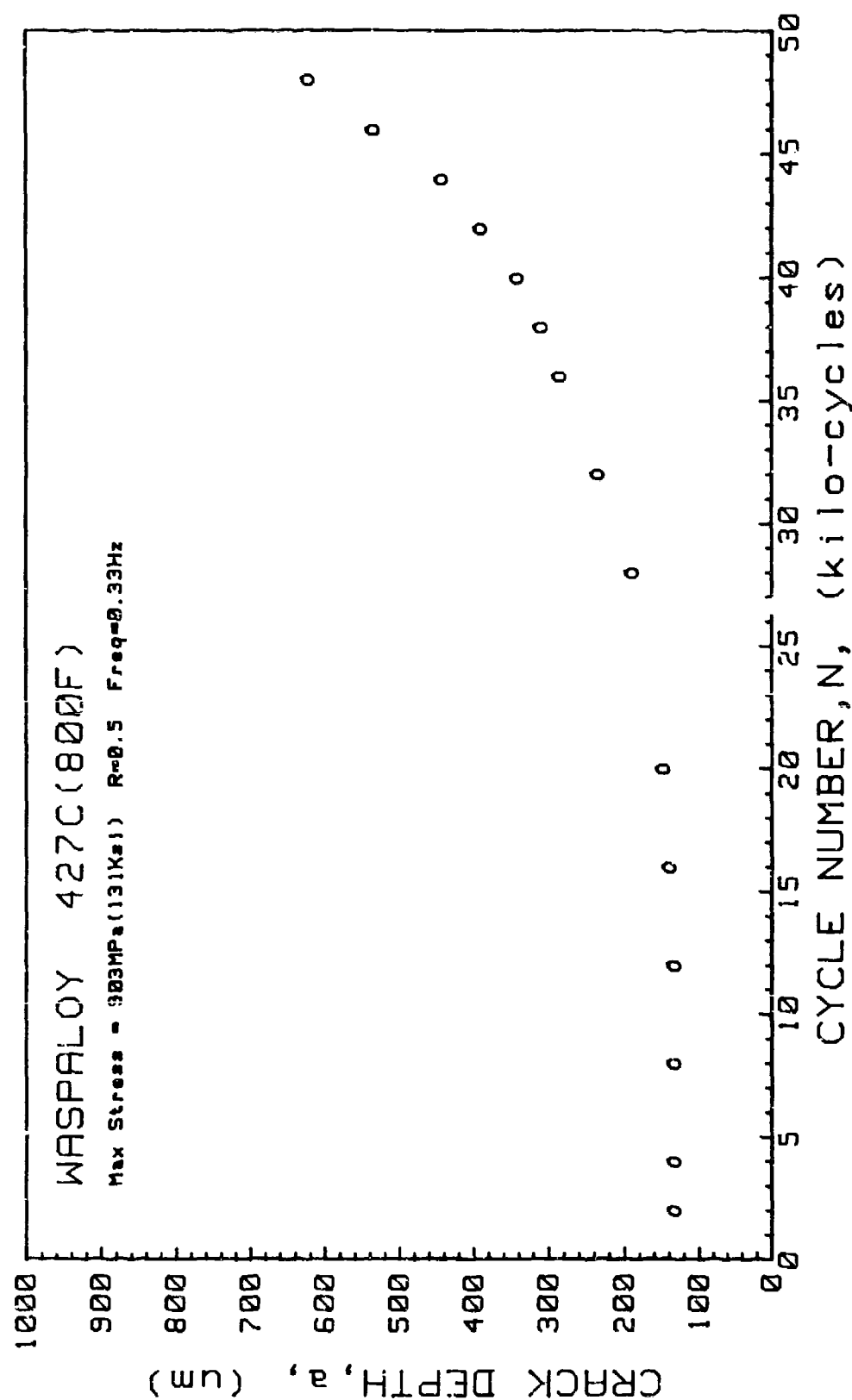


Figure 4.42 Crack depth versus cycle number for Waspalloy tested at 427° C, Max. Stress = 903 MPa, R = 0.5, Freq. = 0.33 Hz.

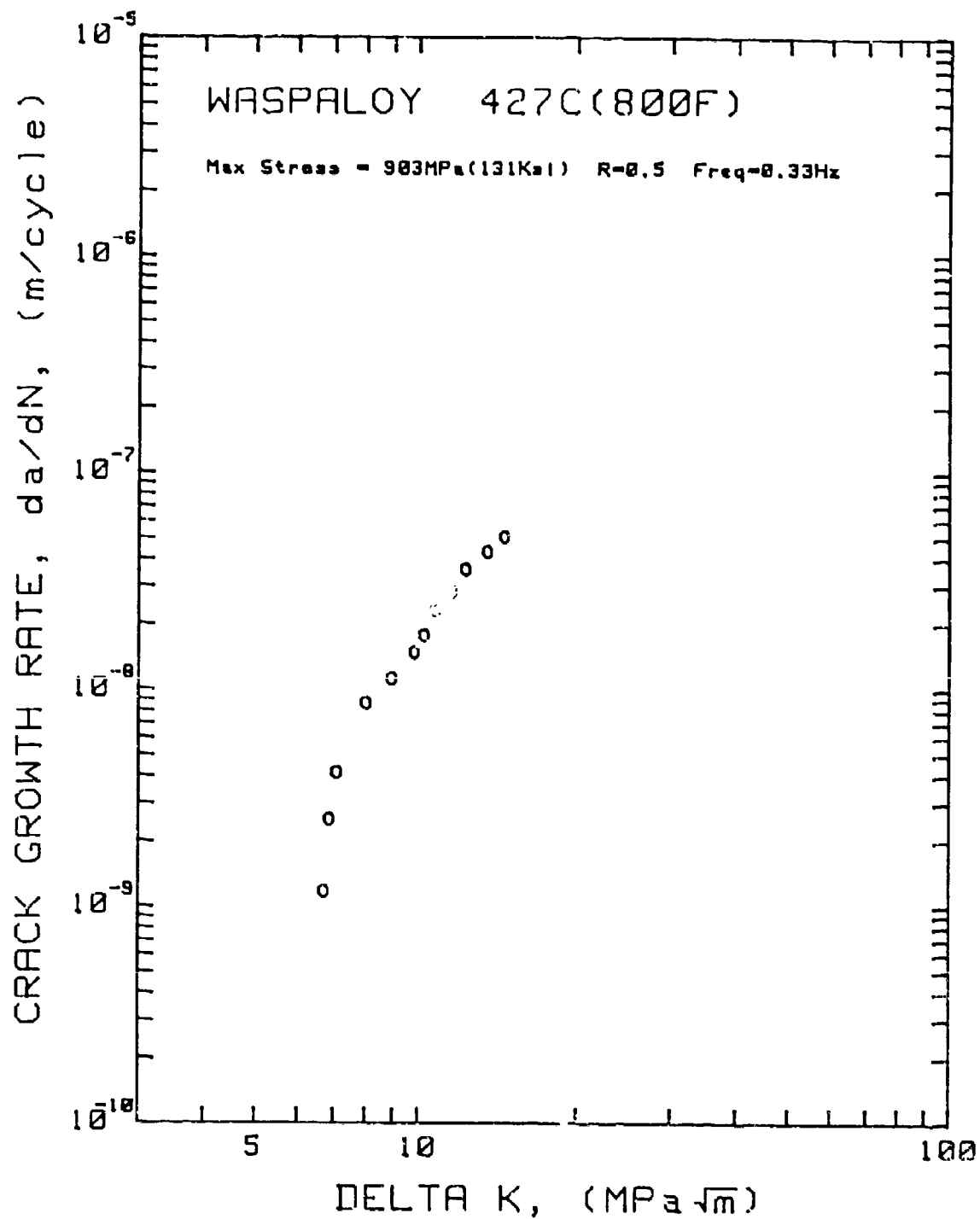


Figure 4.43 Crack growth rate versus stress intensity factor range for Waspaloy tested at 427° C, Max. Stress = 903 MPa, R = 0.5, Freq. = 0.33 Hz.

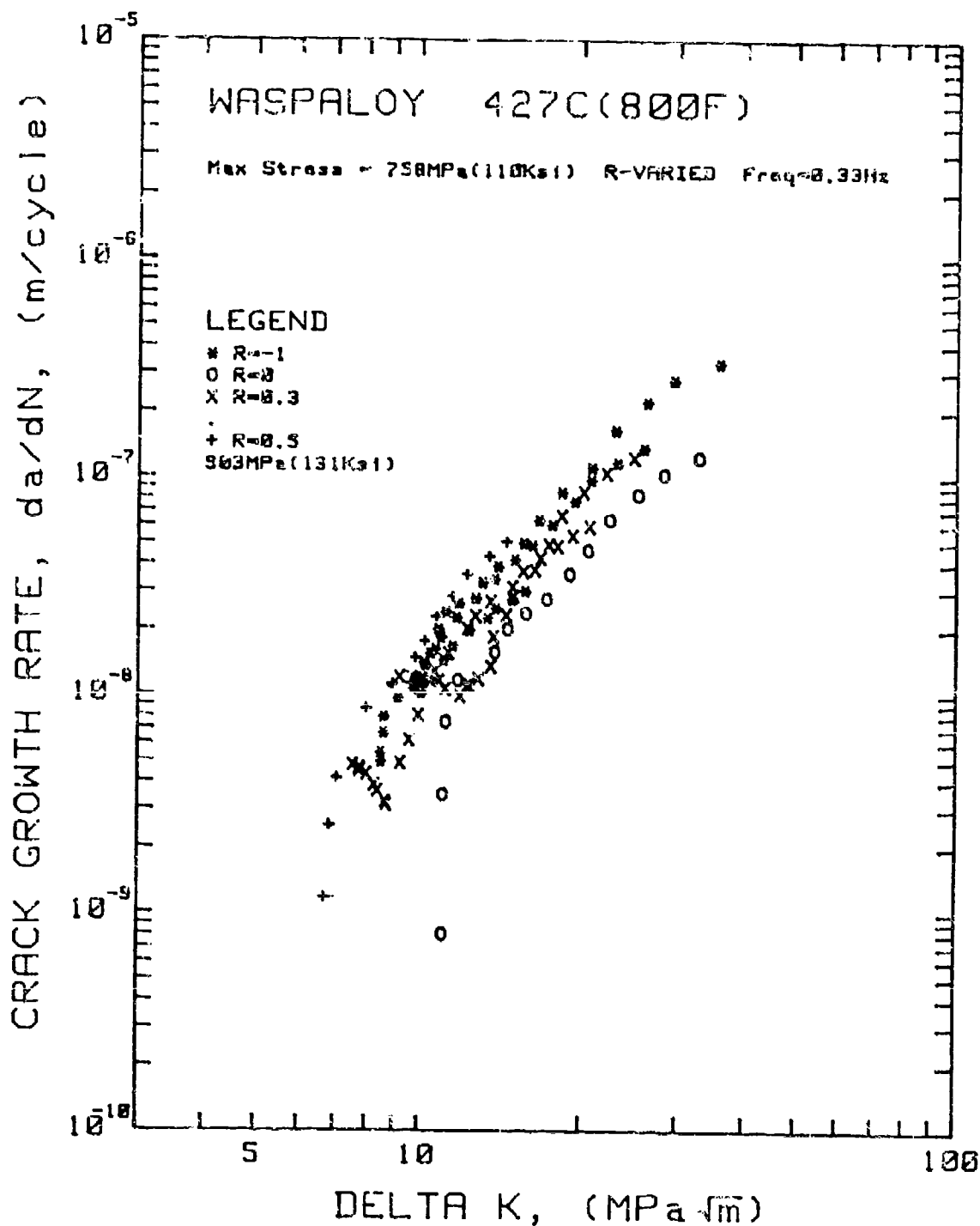


Figure 4.44 Summary of crack growth rate versus stress intensity factor range for Waspaloy tested at 427° C, Max. Stress 758 MPa & 903 MPa, R ratio was varied Freq. = 0.33 Hz.

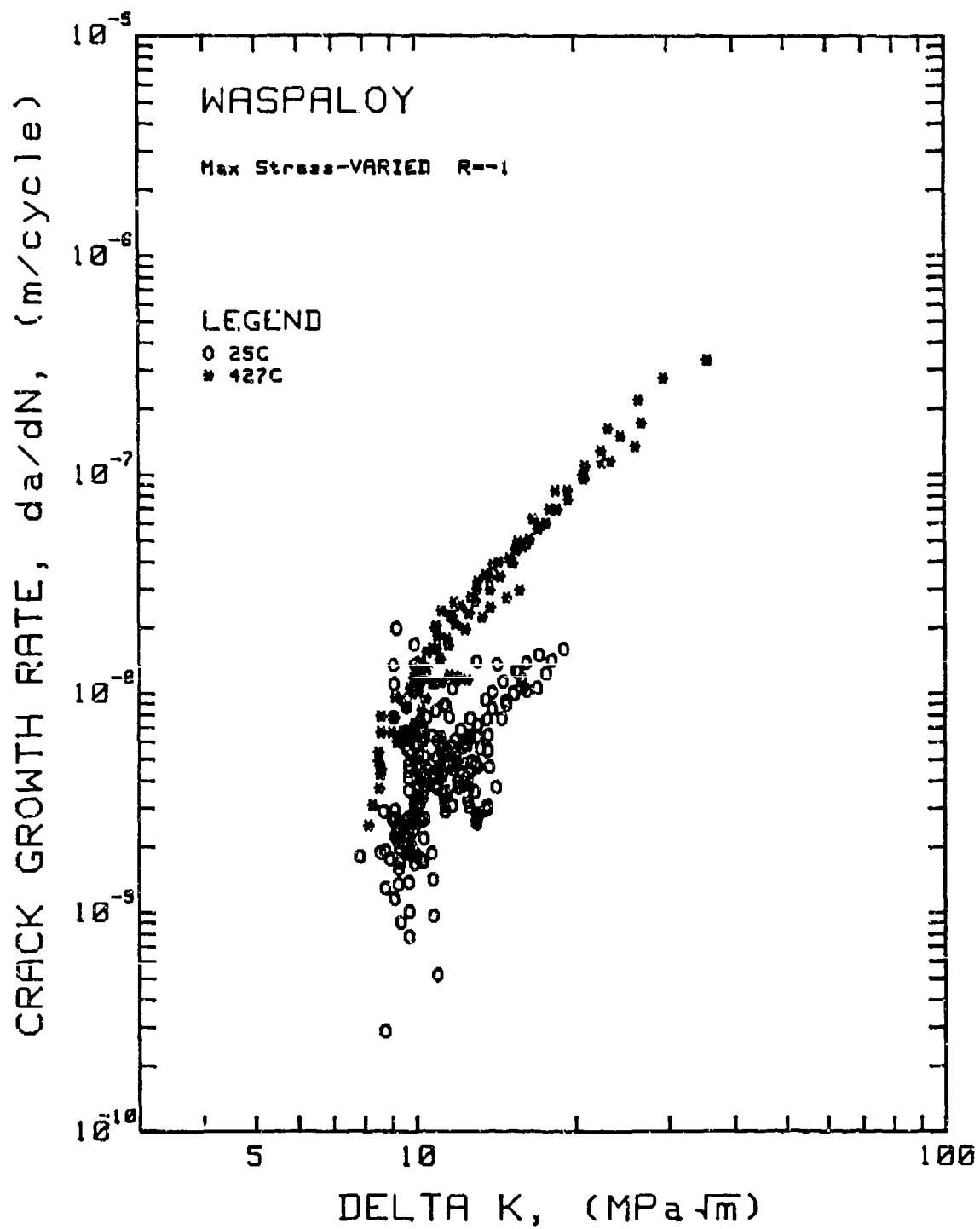


Figure 4.45 Comparison of crack growth rates versus stress intensity factor range for Waspaloy tested at 25° C and 427° C, R = -1.

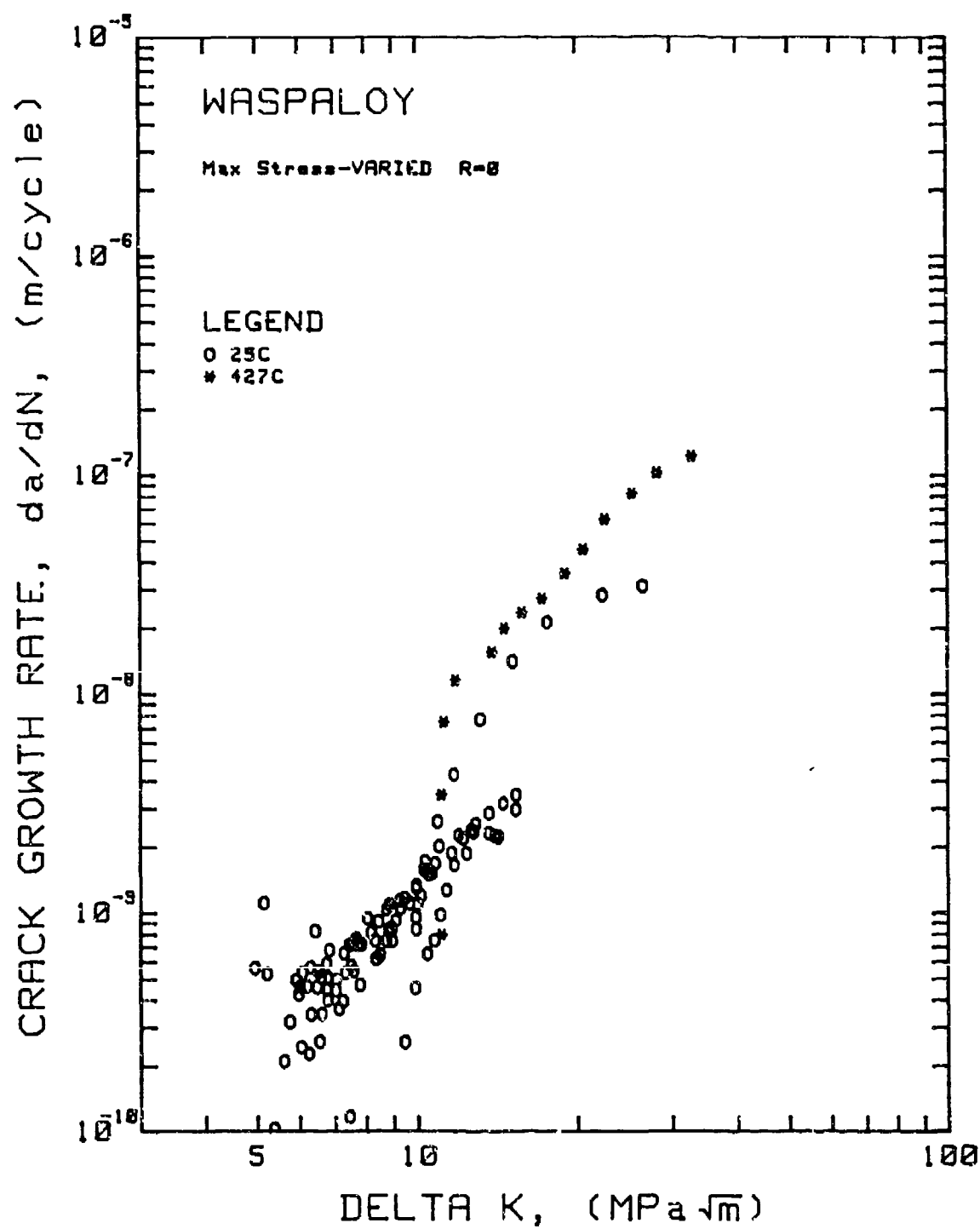


Figure 4.46 Comparison of crack growth rates versus stress intensity factor range for Waspaloy tested at 25° C and 427° C, R = 0.

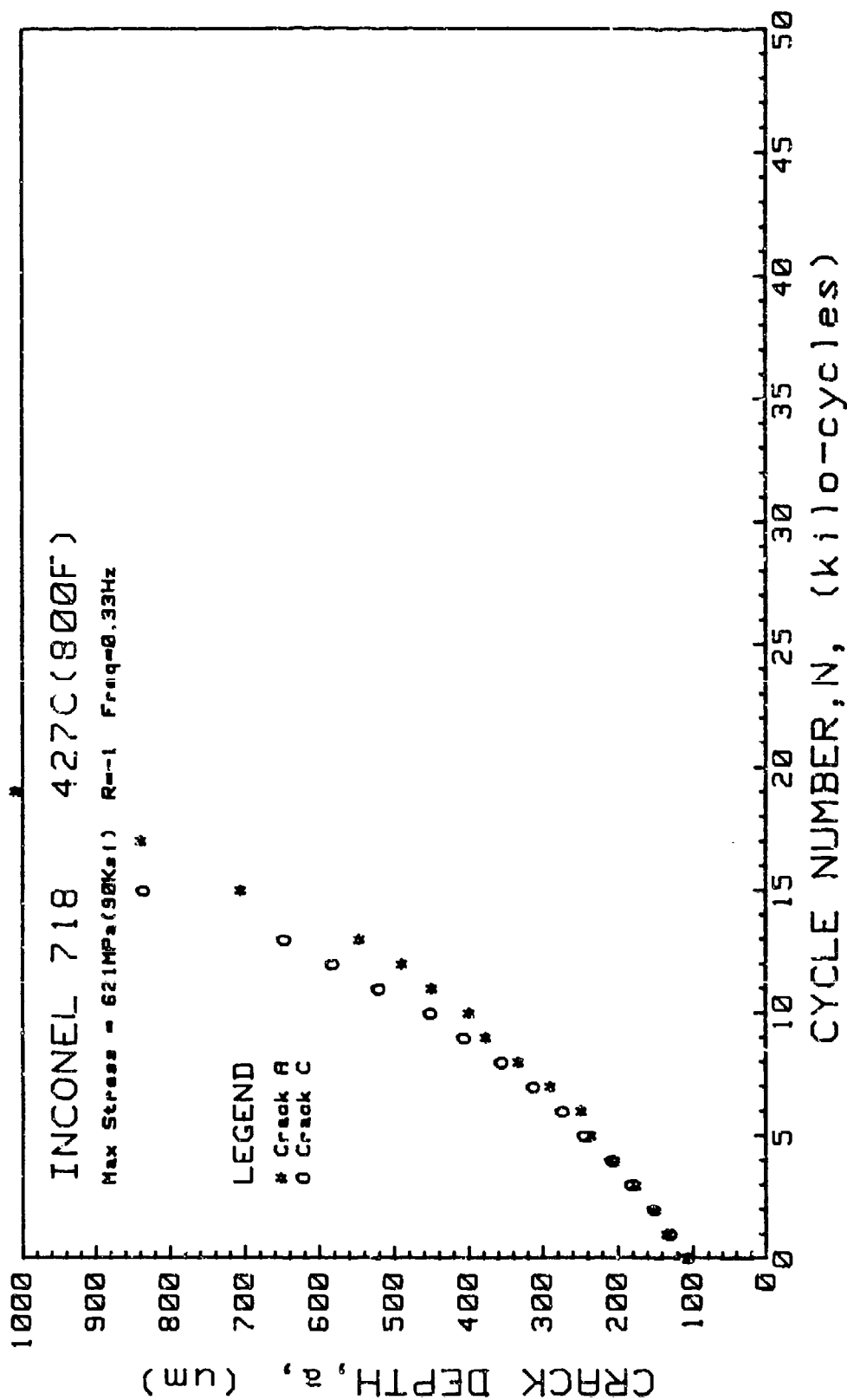


Figure 4.47 Crack depth versus cycle number for Inconel 718 tested at 427° C, Max.  
Stress = 621 MPa, R = -1, Freq. = 0.33 Hz.

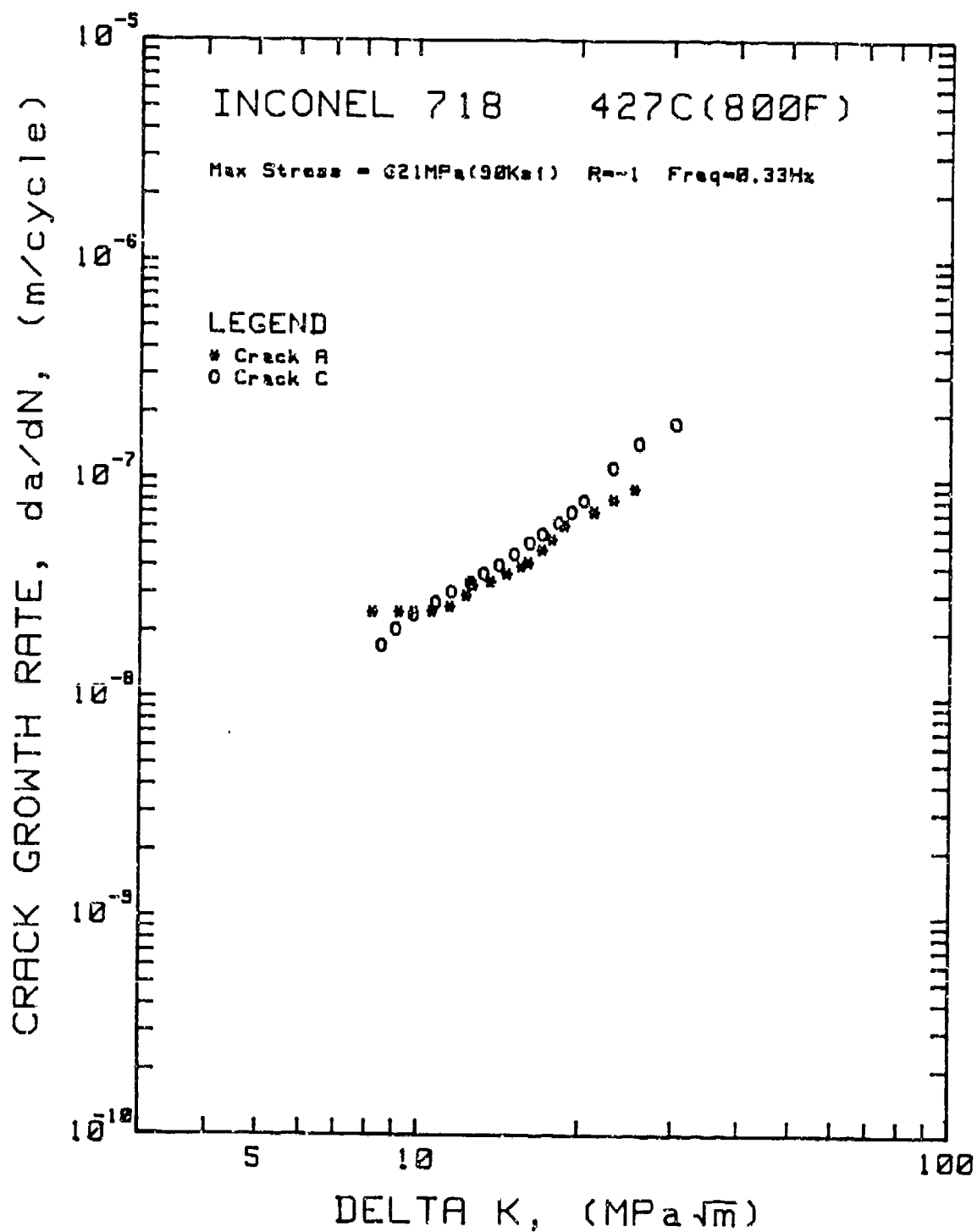


Figure 4.48 Crack growth rate versus stress intensity factor range for Inconel 718 tested at 427°C, Max. Stress = 621 MPa, R = -1, Freq. = 0.33 Hz.



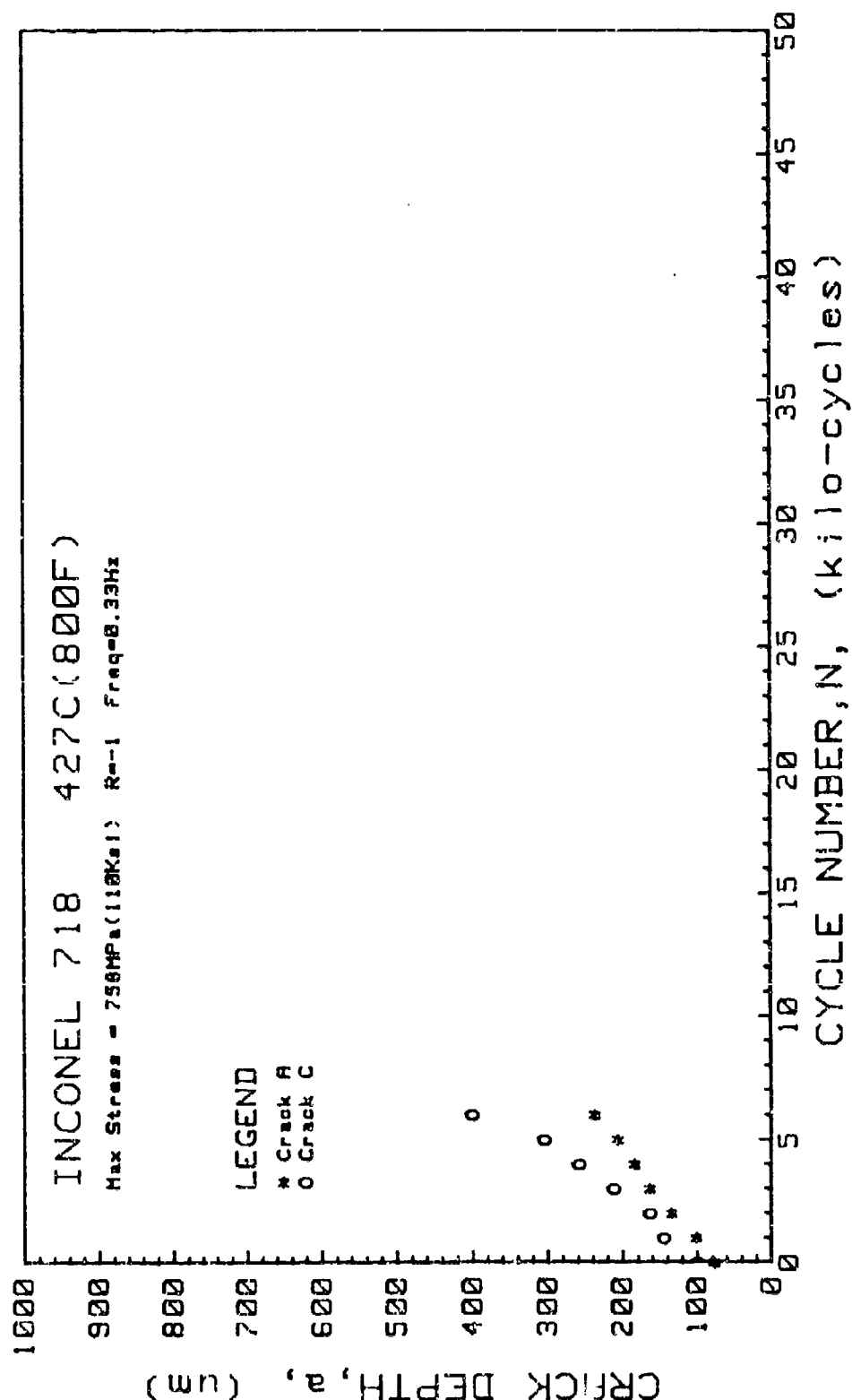


Figure 4.49 Crack depth versus cycle number for Inconel 718 tested at 427° C, Max. Stress = 758 MPa, R = -1, Freq. = 0.33 Hz.

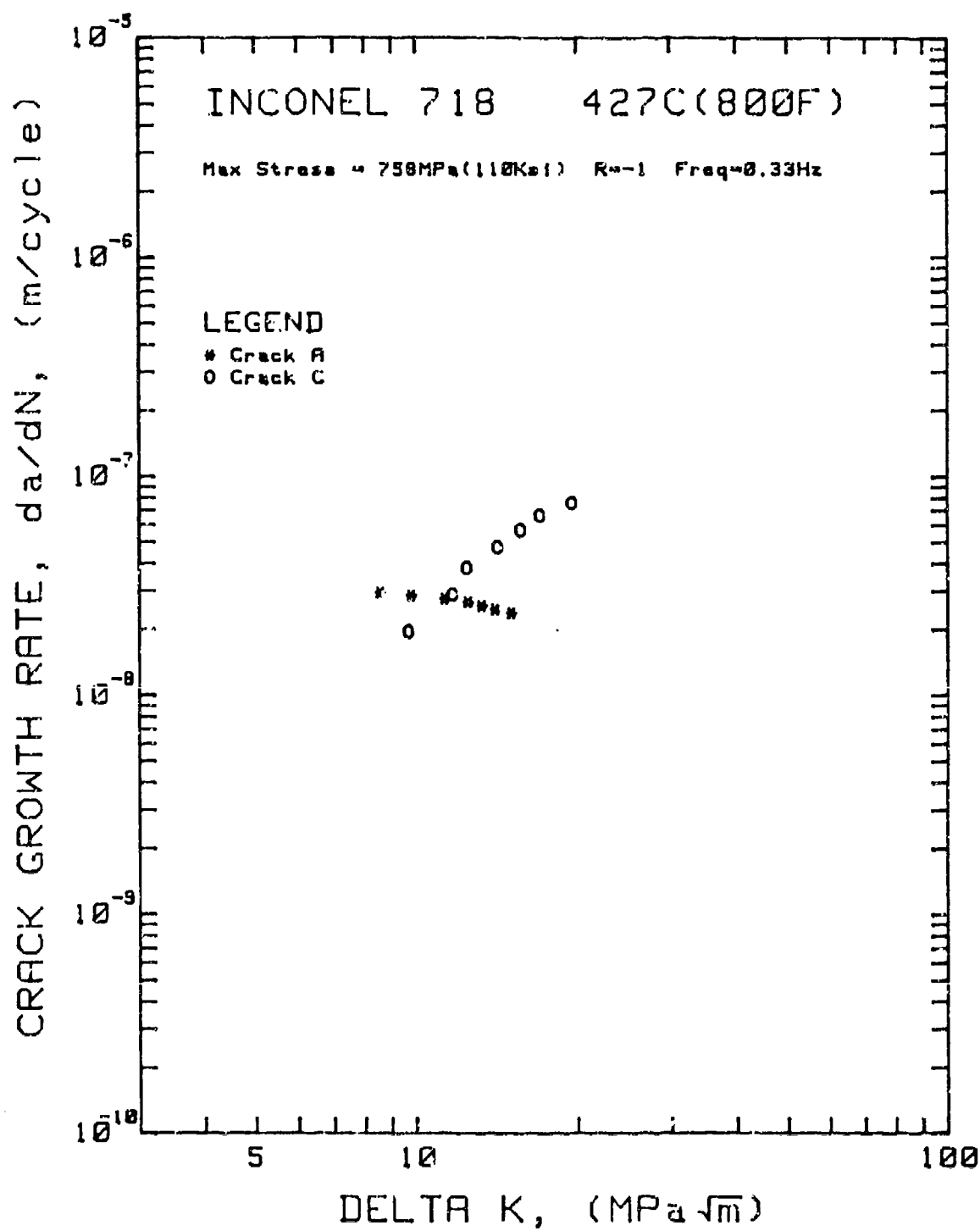


Figure 4.50 Crack growth rate versus stress intensity factor range for Inconel 718 tested at 427°C, Max. Stress = 758 MPa, R = -1, Freq. = 0.33 Hz.

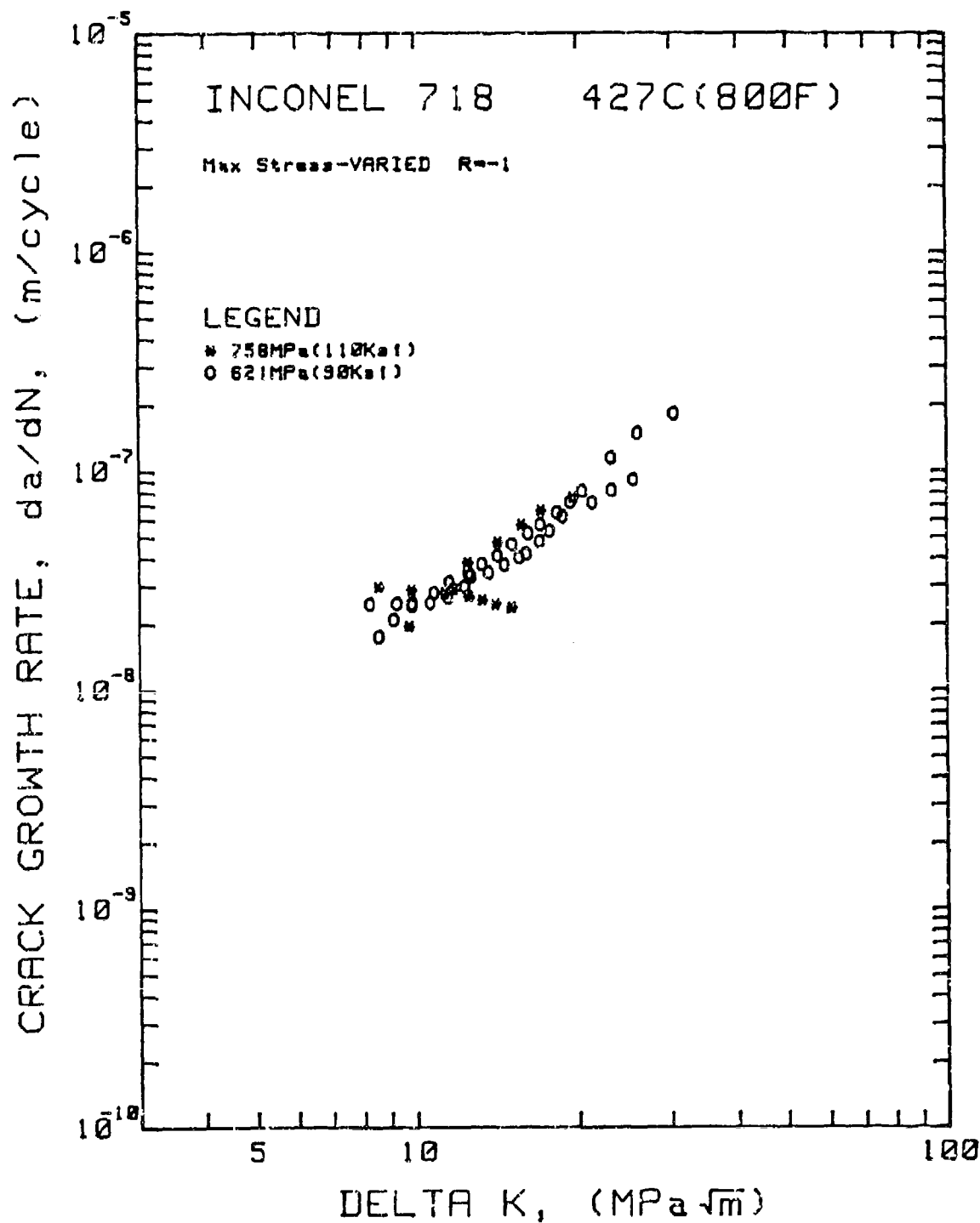


Figure 4.51 Summary of crack growth rate versus stress intensity factor range for Inconel 718 tested at 427° C, Max. Stress was varied, R = -1, Freq. = 0.33 Hz.

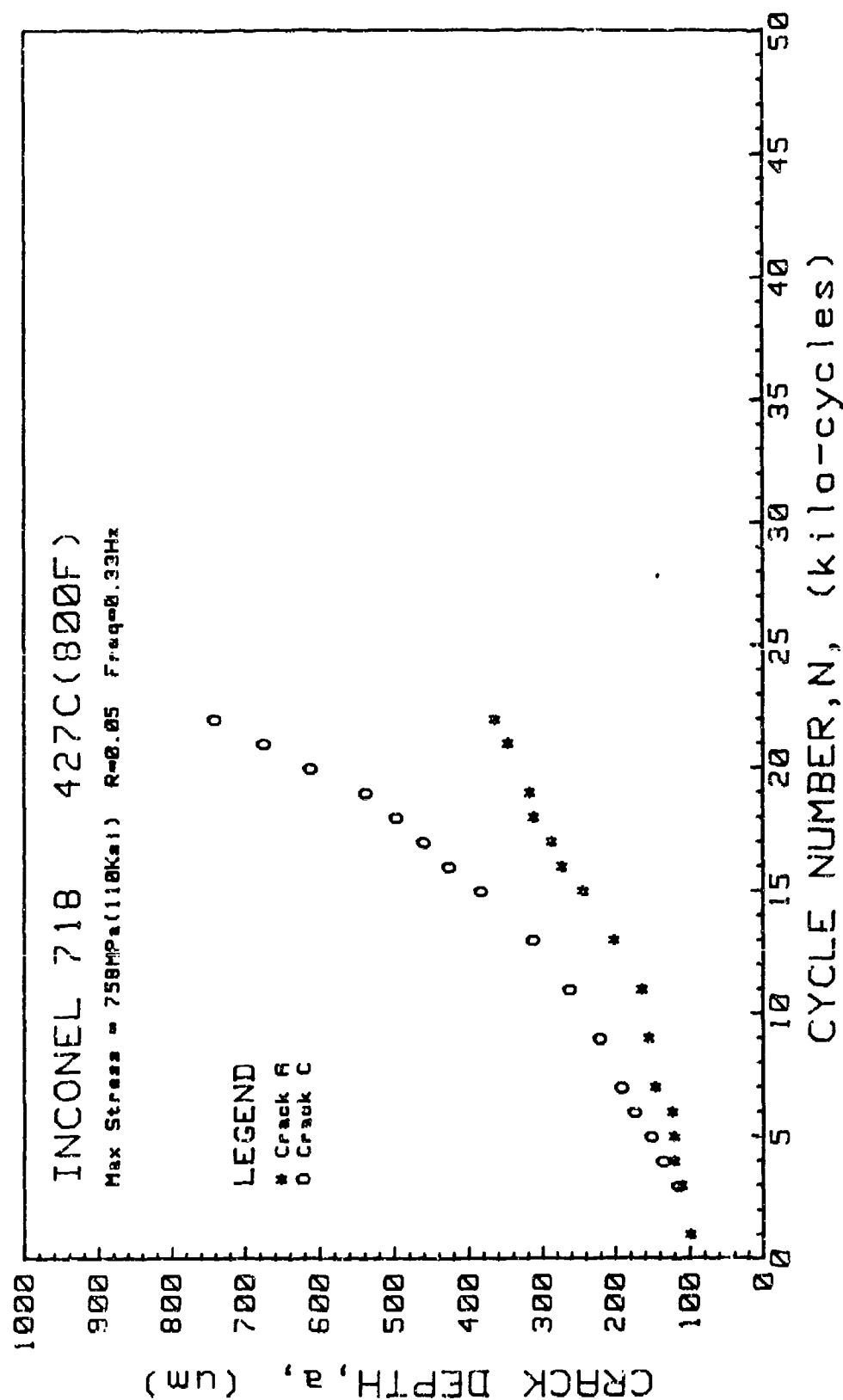


Figure 4.52 Crack depth versus cycle number for Inconel 718 tested at 427° C, Max.  
Stress = 758 MPa, R = 0.05, Freq. = 0.33 Hz.

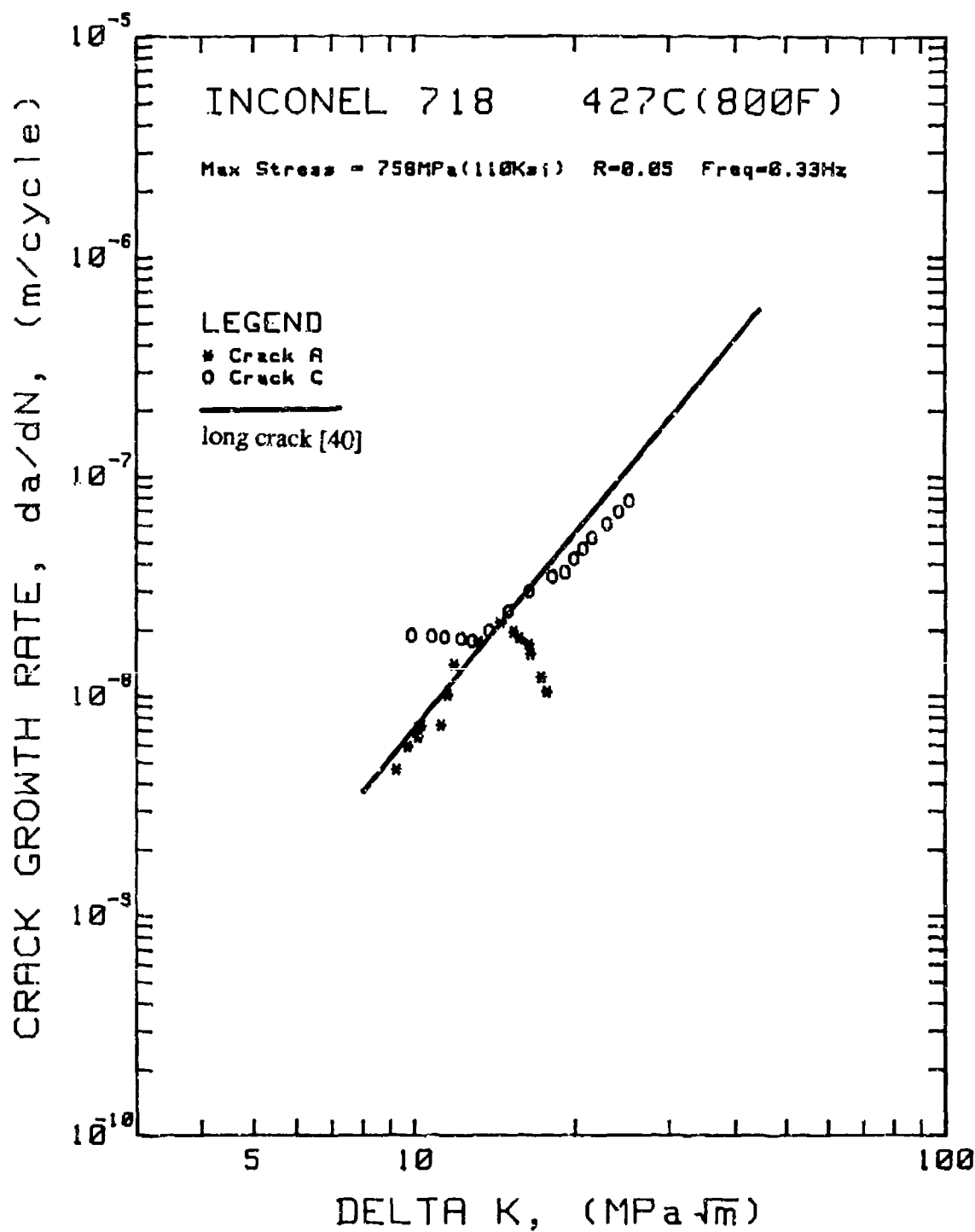


Figure 4.53 Crack growth rate versus stress intensity factor range for Inconel 718 tested at 427C, Max. stress = 758 MPa, R = 0.05, Freq. = 0.33 Hz

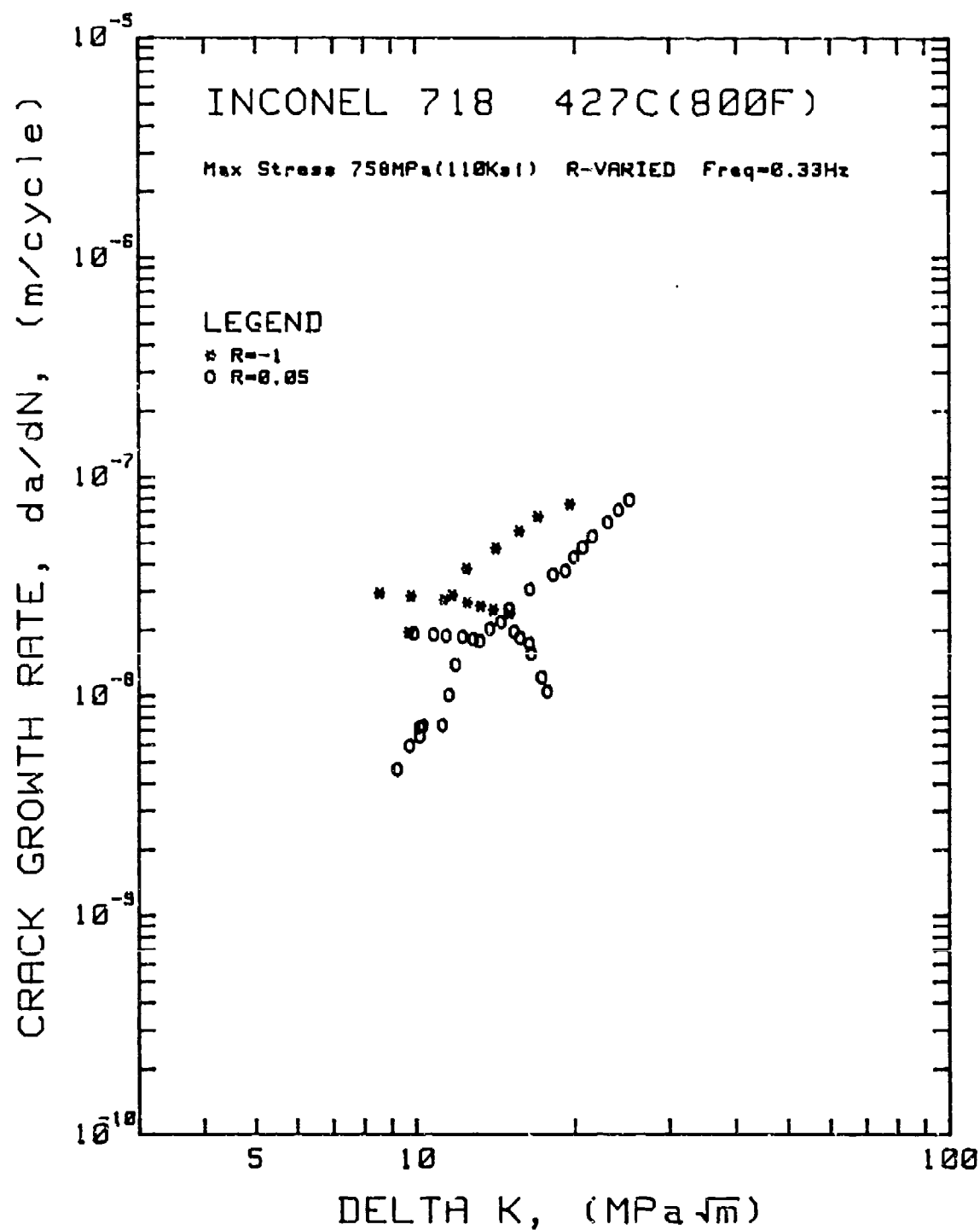


Figure 4.54 Summary of crack growth rate versus stress intensity factor range for Inconel 718 tested at 427° C, Max. Stress = 758 MPa , R ratio was varied, Freq. = 0.33 Hz.

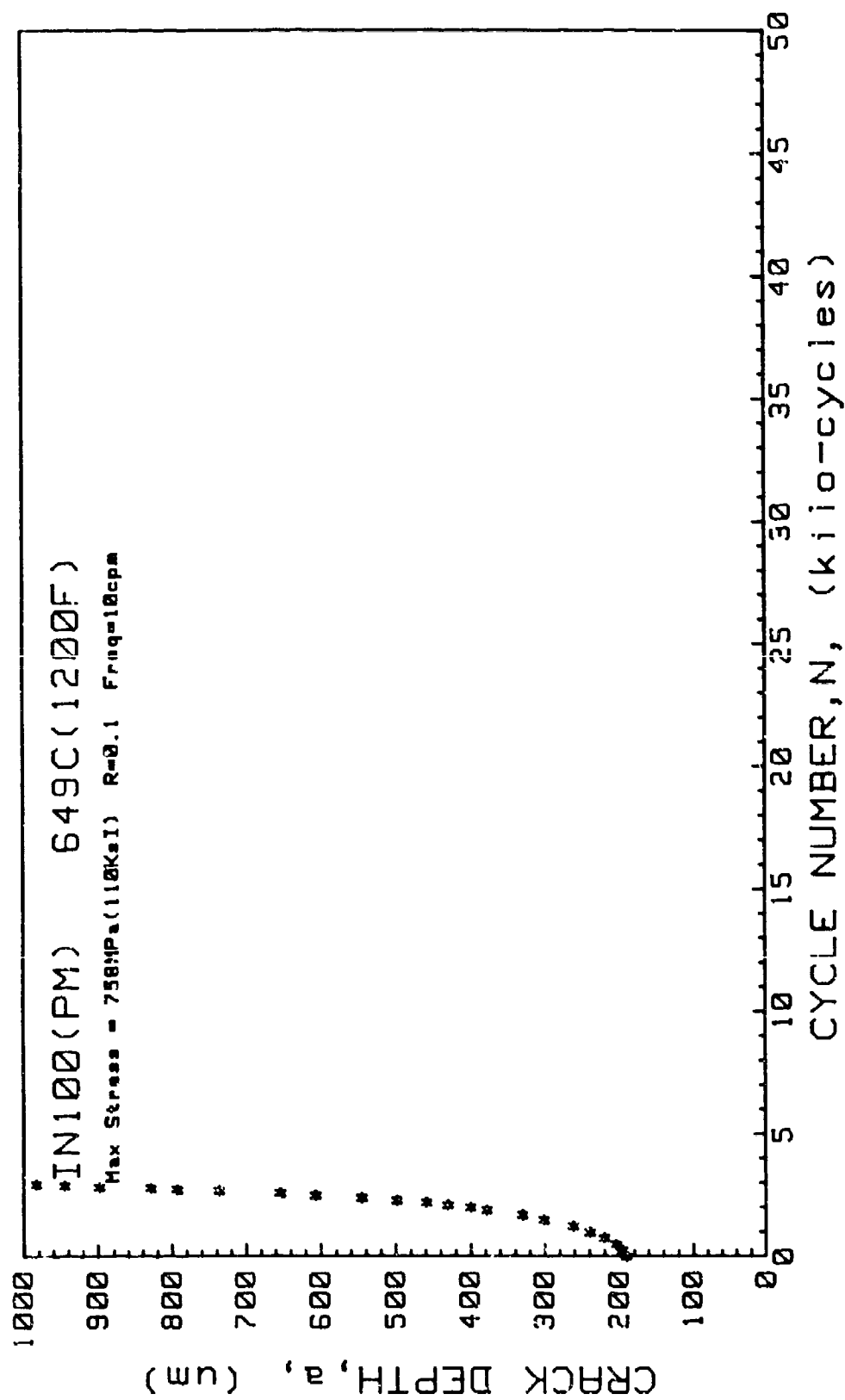


Figure 4.55 Crack depth versus cycle number for IN100 (PM) tested at 649° C, Max. Stress = 758 MPa, R = 0.1, Freq. = 10 cpm.

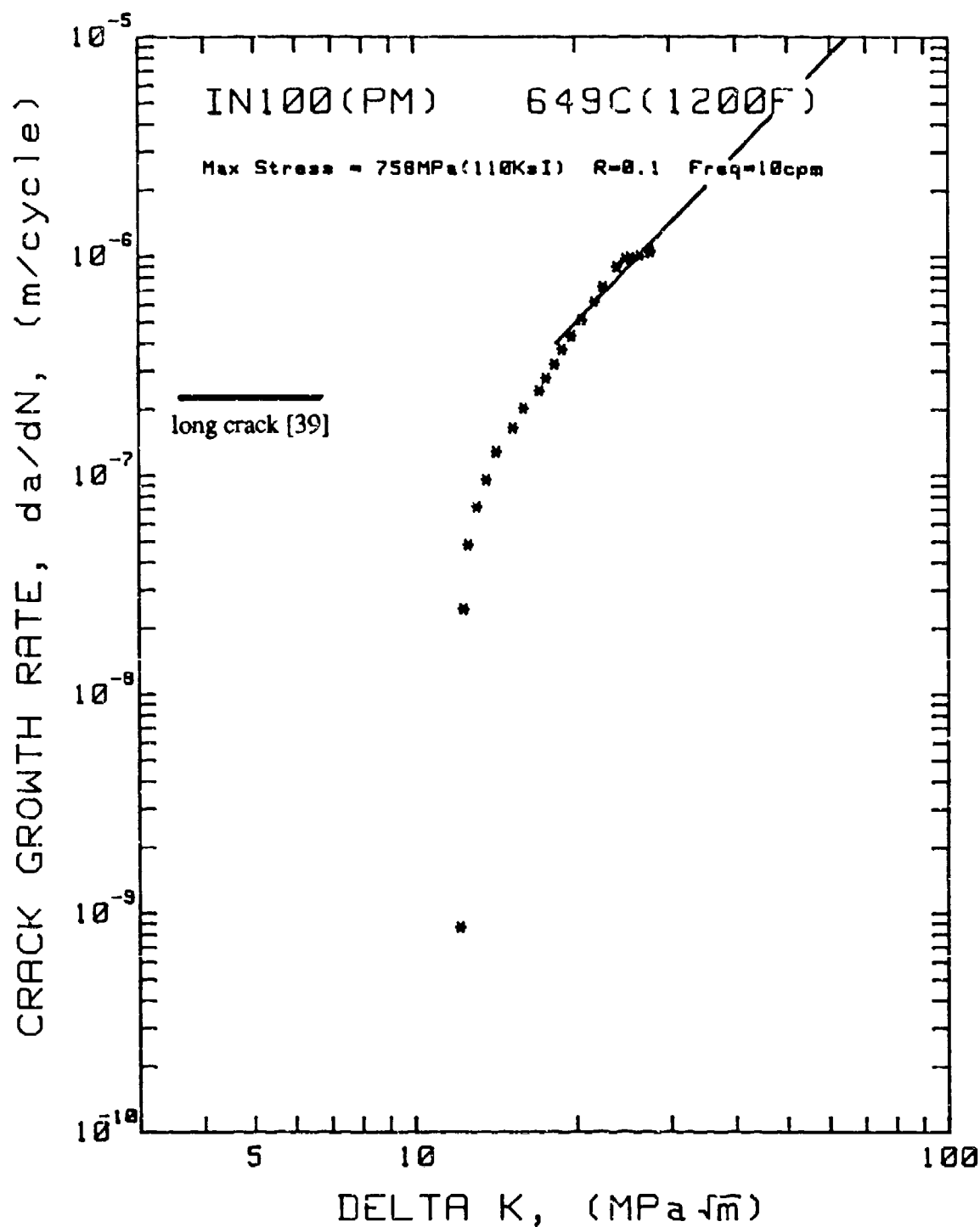


Figure 4.56 Crack growth rate versus stress intensity factor range for IN100 (PM) tested at 649°C, Max. Stress = 758 MPa, R = 0.1, Freq. = 10 cpm.



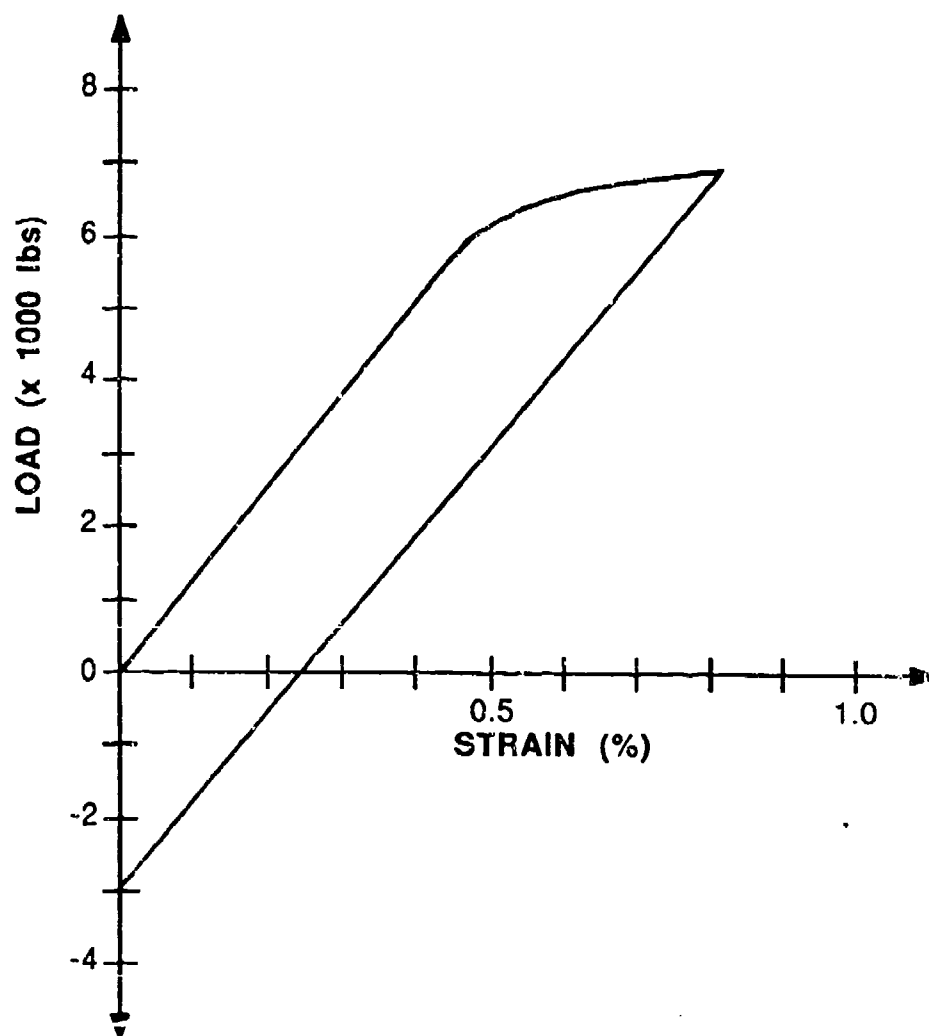


Figure 4.57 First hysteresis loop for IN100 (PM) tested under strain control at 649° C, Average Max. Stress = 1100 MPa, Total Strain Range = 0 to 0.80%.

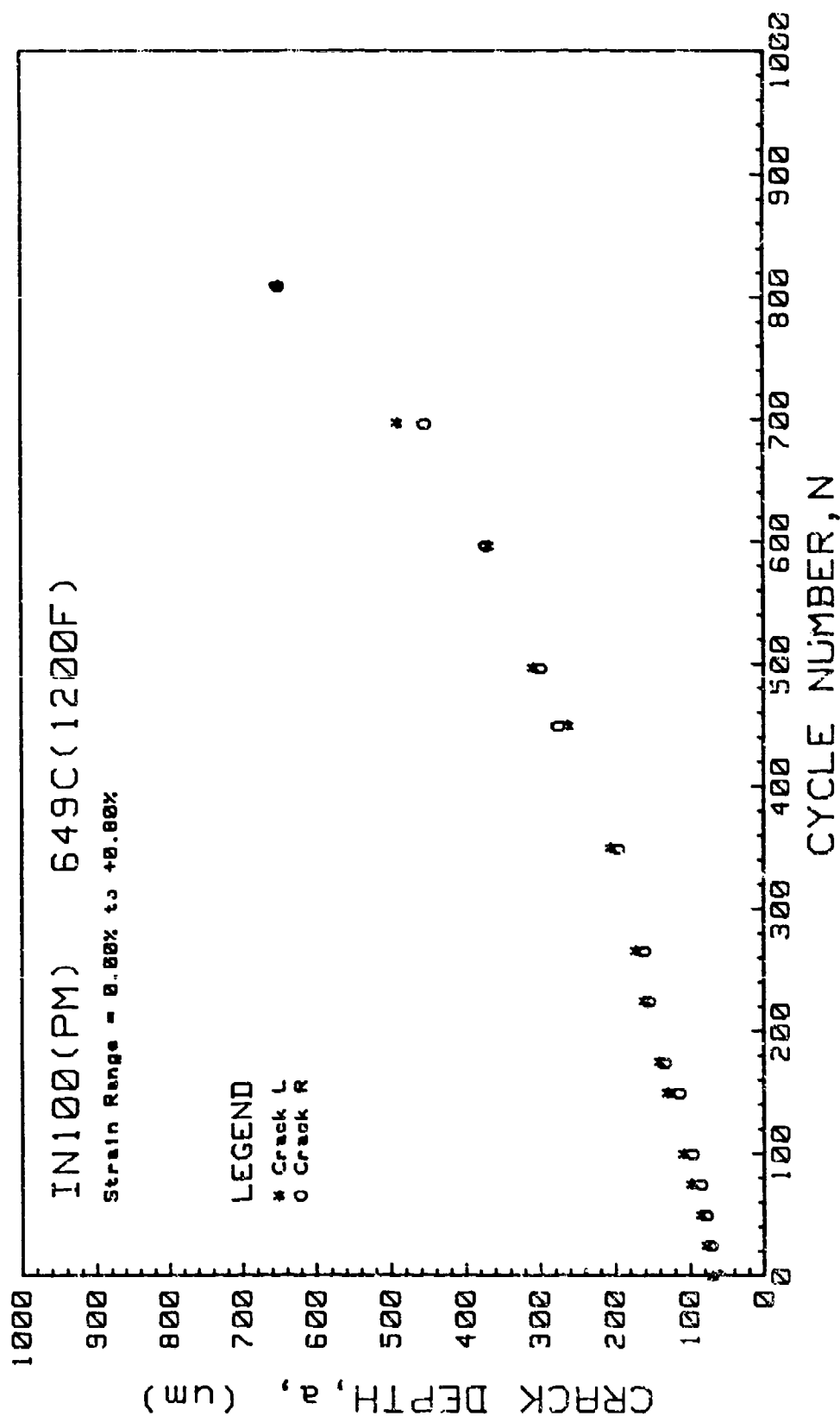


Figure 4.58 Crack depth versus cycle number for IN100 (PM) tested under strain control at 645° C, Average Max. Stress = 1100 MPa, Total Strain Range = 0 to 0.80%.

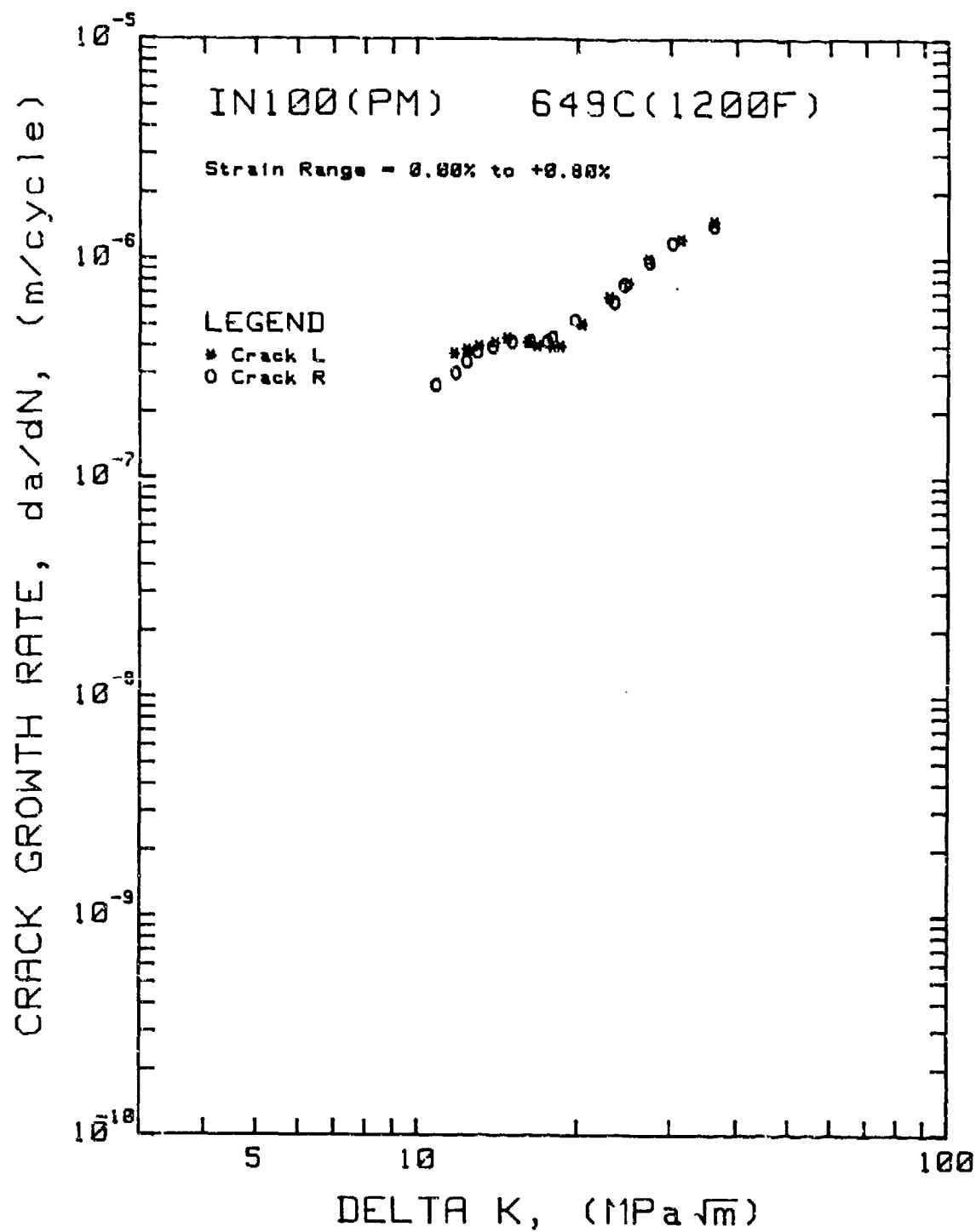


Figure 4.59 Crack growth rate versus stress intensity factor range for IN100 (PM) tested under strain control at 649° C, Average Max. Stress = 1100 MPa, Total Strain Range = 0 to 0.80%.

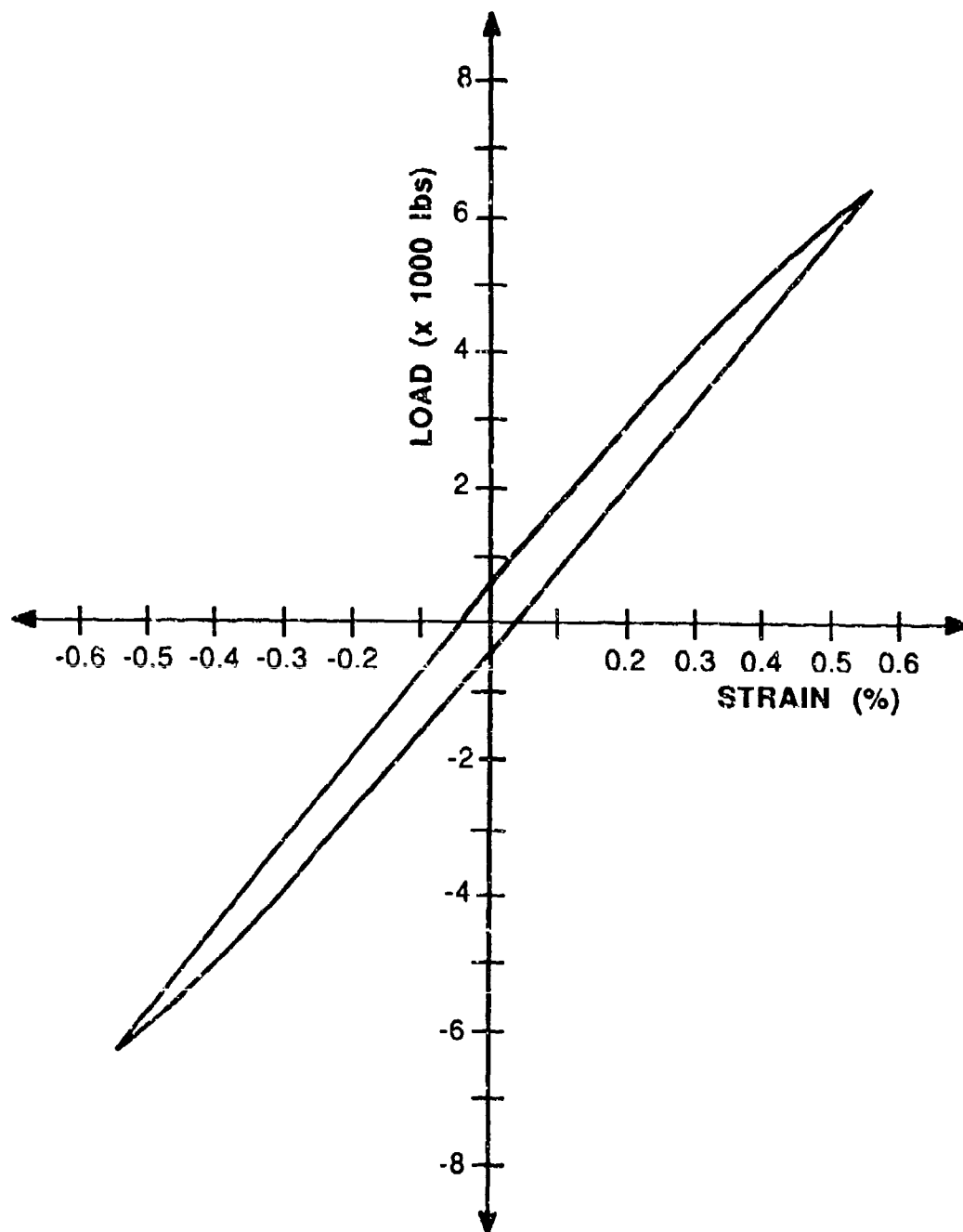


Figure 4.60 Typical hysteresis loop for IN100 (PM) tested under strain control at 649°C, Average Max. Stress = 1026 MPa, Total Strain Range =  $\pm 0.55\%$ .

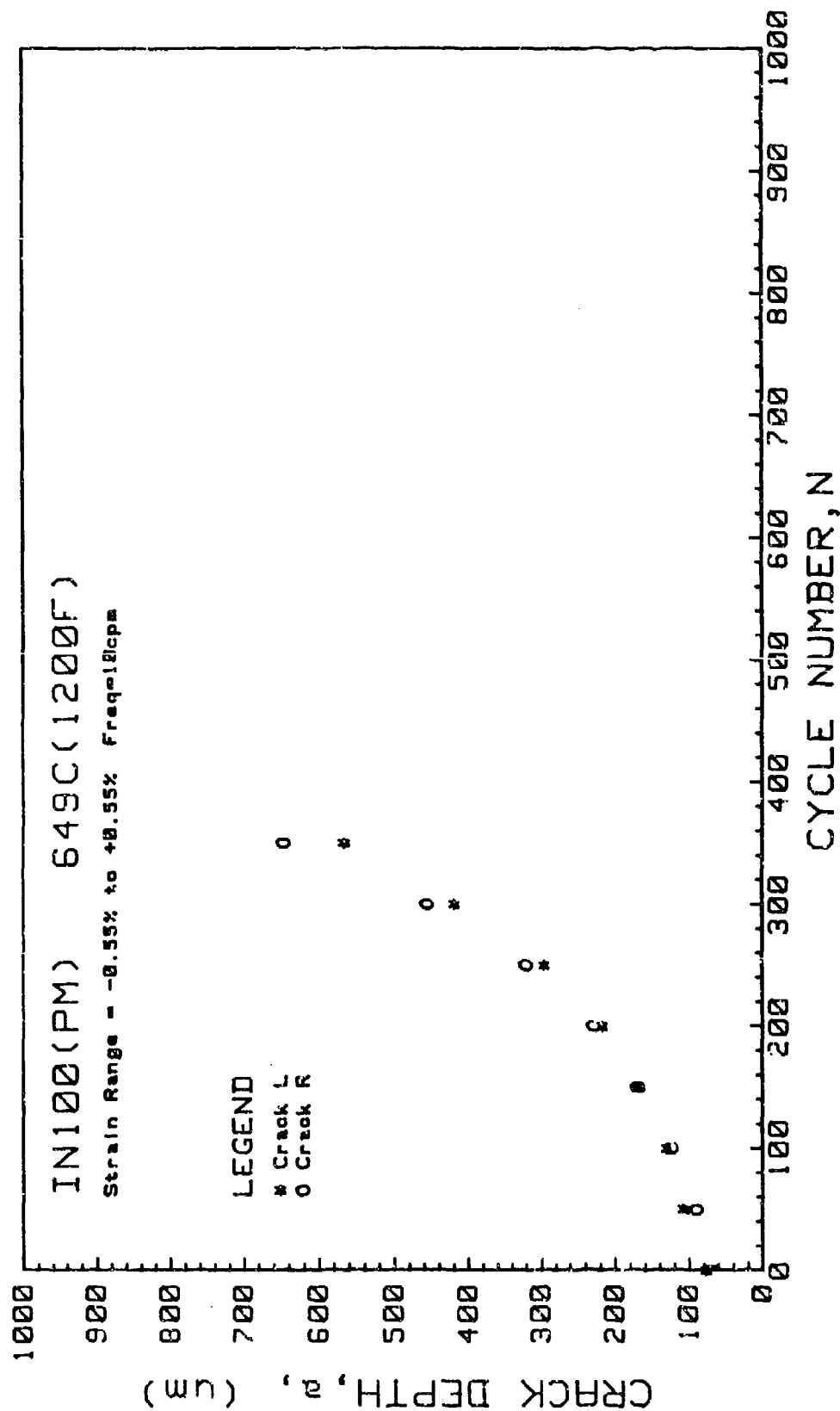


Figure 4.61 Crack depth versus cycle number for IN100 (PM) tested under strain control at 649°C, Average Max. Stress = 1026 MPa, Total Strain Range =  $\pm 0.55\%$ .

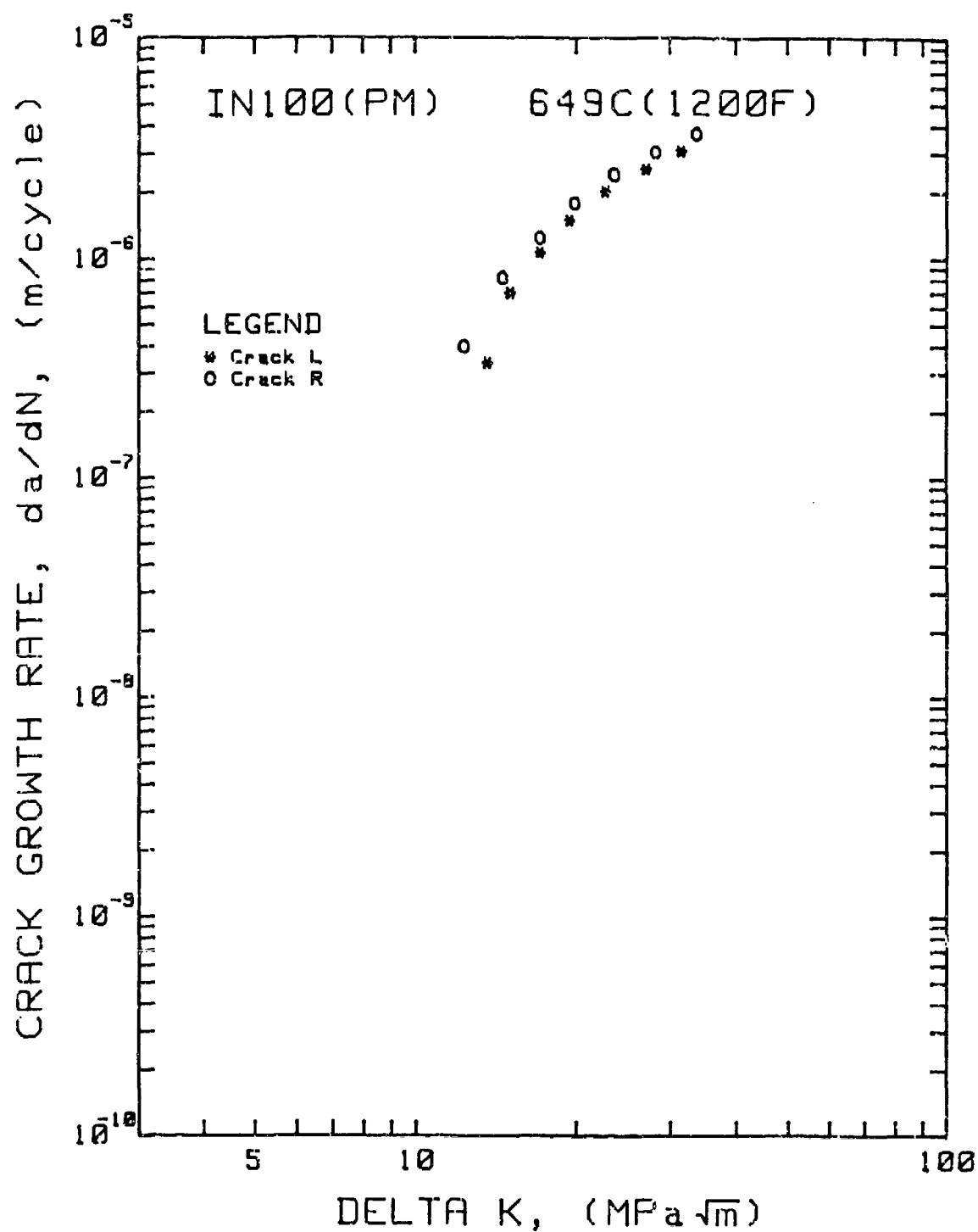


Figure 4.62 Crack growth rate versus stress intensity factor range for IN100 (PM) tested under strain control at 649°C, Average Max. Stress = 1026 MPa, Total Strain Range =  $\pm 0.55\%$ .

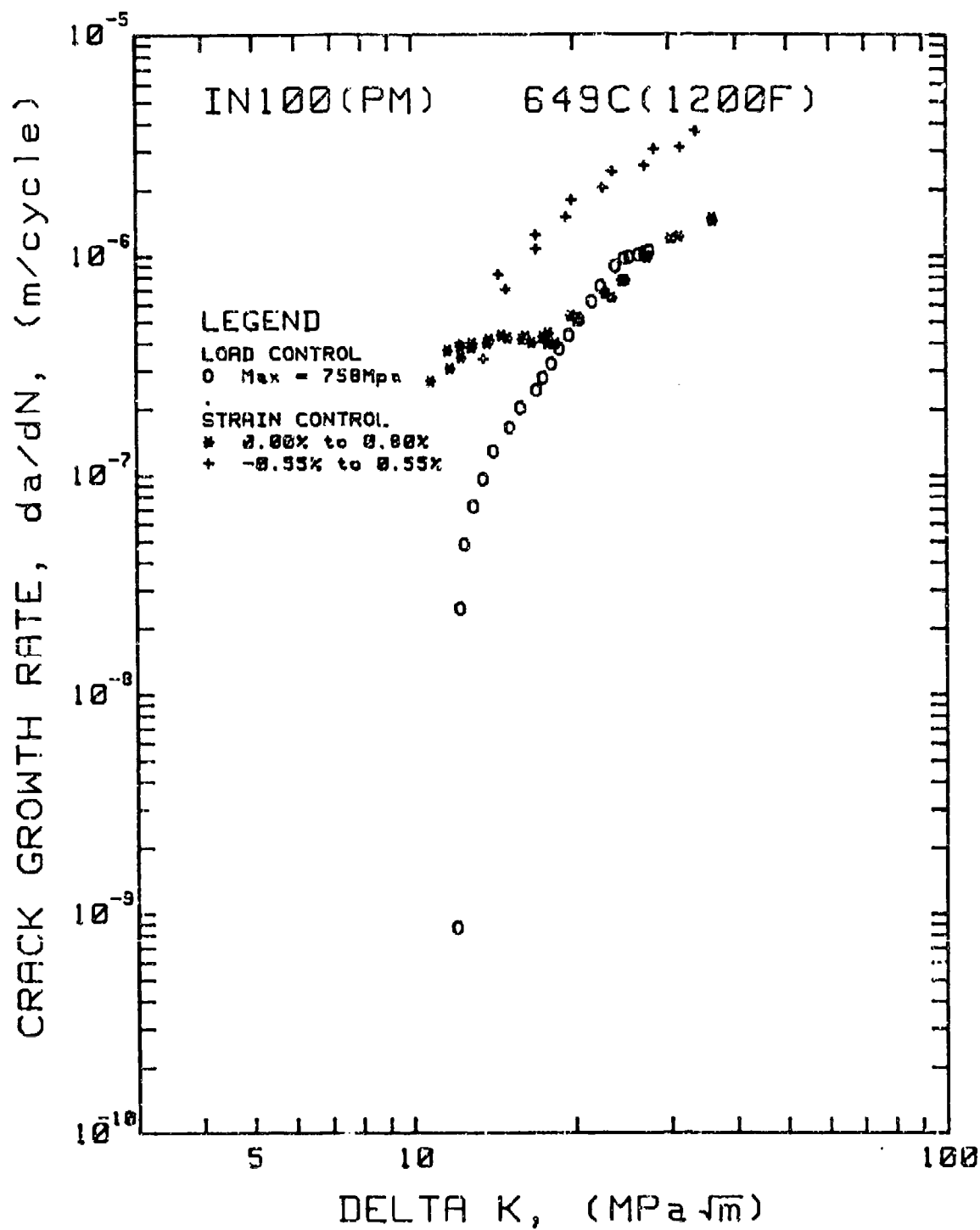
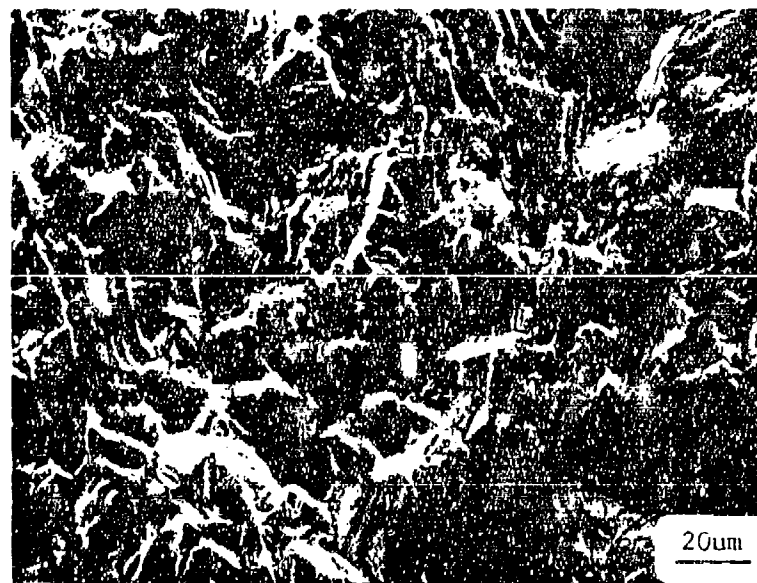


Figure 4.63 Summary of crack growth rate versus stress intensity factor range for IN100 (PM) tested under load control and strain control at 649° C.



(a)



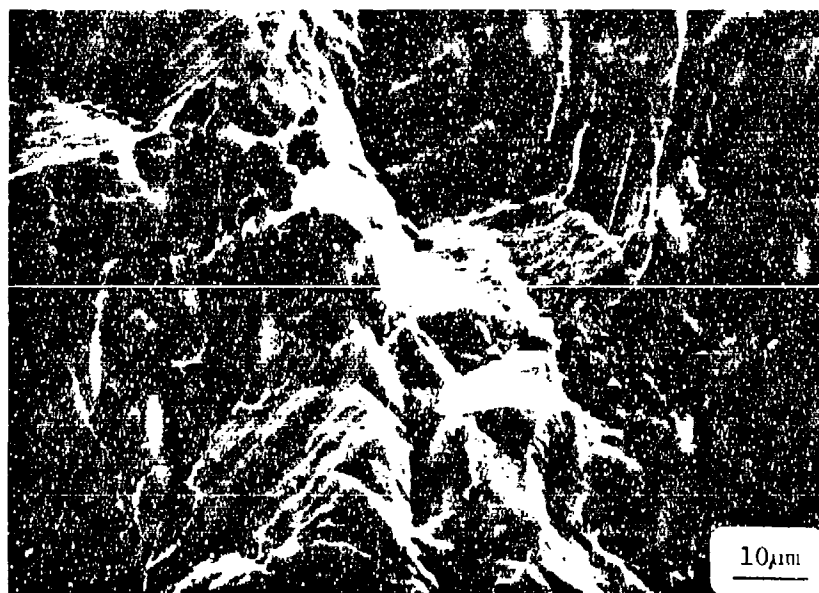
(b)

Figure 4.64 Fractographs of Waspaloy tested at 427C



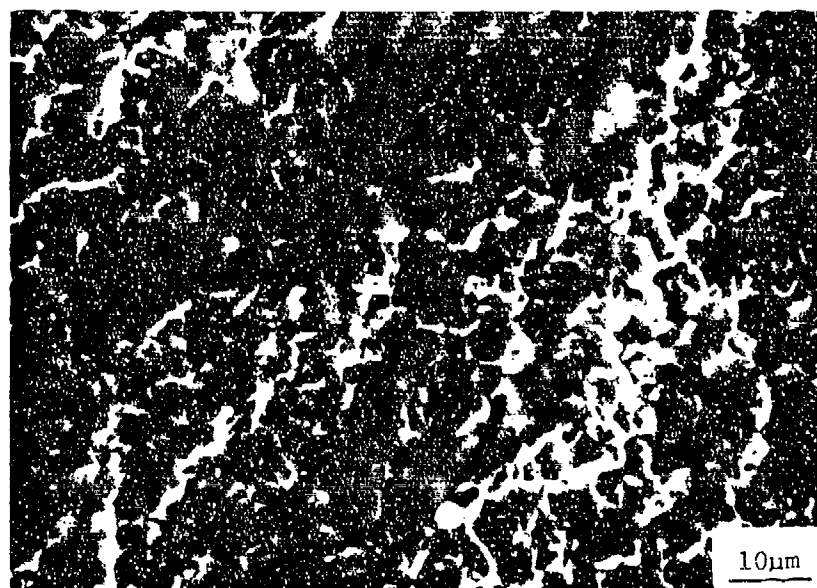


(a)

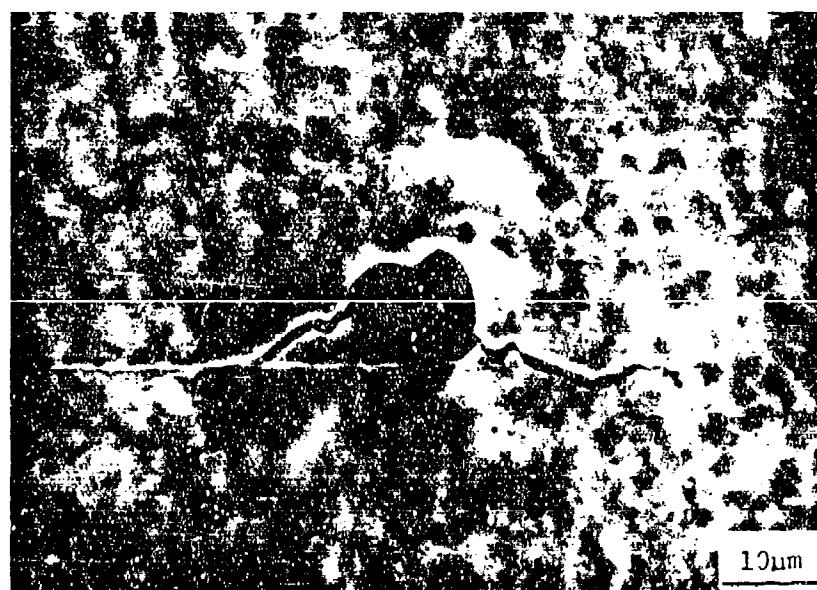


(b)

Figure 4.65 (a) Optical micrograph of fatigue crack trace on gauge section surface and (b) SEM fractograph for Inconel 718 tested at 427C



(a)



(b)

Figure 4.66 (a) SEM micrograph of a typical fracture surface and (b) SEM micrograph of pore and fatigue crack in gauge section surface after 150 cycles of strain controlled cycling at a total strain range of 0% to 0.80%

## 5. CONCLUSIONS

### Room Temperature Tests:

1. The fatigue behavior of small crystallographic cracks is strongly grain size dependent. In large grains, small cracks grew at higher rates than long cracks at the same nominal  $\Delta K$ . In fine grained materials such as René 95, the fatigue behavior of small cracks and long cracks was the same. The transition from small crack to long crack behavior occurs around 3 to 5 times the grain size.
2. The fatigue threshold behavior of small cracks was found to differ from long crack results in large grained alloys.
3. Grain boundaries serve as a constraint to the spreading of plastic slip bands and the propagation of small surface cracks. This leads to considerable scatter in threshold stress intensity factor ranges and near-threshold crack growth rates.

### Elevated Temperature Tests:

4. The mechanical driving force for fatigue crack growth of small cracks ( $a > 100 \mu\text{m}$ ) in turbine disk alloys can be characterized in terms of  $\Delta K$  when the material is subjected to nominally elastic cyclic loading. The upper bound of crack growth rates for small cracks is coincident with the long crack trend.
5. When cycling at high values of maximum stress, approaching the cyclic yield strength, crack growth rates were constant over an initial regime of crack extension ( $100 \mu\text{m} < a < 300 \mu\text{m}$ ).
6. LEFM could not consolidate crack growth rates under elastic-plastic cycling.

In General:

7. The compressive component of the cyclic stress range promotes crack initiation in PSB's and at defects. Crack growth rates are higher at the same nominal value of  $\Delta K$  when  $R < 0$ .

8. Fracture paths of small cracks exhibited transgranular crystallographic features which leads to roughness induced crack closure and a mixed mode of crack extension, Mode I and Mode II.

## References

1. W. D. Cowie, "Turbine Engine Structural Integrity Program (ENSIP)," *Journal of Aircraft*, Vol. 12, No. 4, pp. 366-369.
2. Huntington Alloy Handbook, International Nickel Company, 3rd edition, 1977.
3. R. G. Ballinger, J. W. Prybylowski and C. K. Elliott, "Microstructural Analysis of Double Aged and Annealed Plus Double Aged Inconel Alloy X-750," unpublished research report, MIT, 1984.
4. The Superalloys Ed. C. T. Sims and W. C. Hagel, John Wiley and Sons, 1972.
5. J. A. Dominge, W. J. Boesch and J. F. Radavich, "Phase Relationships in René 95," in Superalloys 1980. Proceedings of the 4th International Symp. on Superalloys, pp. 335-344, 1980.
6. G. Bellows, "Low Stress Grinding," *Machinability Data Center*, Pub. No. MDC 78-103, 1978.
7. S. J. Hudok, Jr, A. Saxena, R. J. Bucci and R. C. Malcolm, "Development of Standard Methods of Testing and Analyzing Fatigue Crack Growth Rate Data," Technical Report AFML-TR-78-40, 1978.
8. G. R. Irwin, Journal of Applied Mechanics, American Society of Mechanical Engineers, V. 29, No. 4, 1962, pp. 651-654.
9. I. N. Sneddon, "The Distribution of Stress in the Neighborhood of a Crack in an Elastic Solid," in Proc. Roy. Soc. London A187, 1946, pp. 229-260.
10. J. C. Newman, Jr., "A Review and Assessment of the Stress-Intensity Factors for Surface Cracks" A Part-Through Crack Fatigue Life Prediction, ASTM STP 687, J. B. Chang, Ed. American Society for Testing and Materials, 1979, pp. 16-42.
11. H. Nisitani and D. H. Chen, "Stress Intensity Factor for a Semi-Elliptical Surface Crack in a Shaft Under Tension," Trans. Japan Soc. Mech. Engrs., V. 50, No. 453 (1984) pp. 1077-1082.
12. I. S. Raju and J. C. Newman, Jr., "Stress-Intensity Factors for Circumferential Surface Cracks in Pipes and Rods Under Tension and Bending Loads," NASA Technical Memorandum 87594, 1985.
13. S. Suresh and R. O. Ritchie, "Propagation of Short Fatigue Cracks," Int. Met. Rev., Vol.29, No.6, 1984, pp. 445-476.
14. B. N. Leis, M. F. Kanninen, A. T. Hopper, J. Ahmad, and D. Brock, "A Critical Review of the Short Crack Problem in Fatigue," AFWAL-TR-83-4019, AFWAL Materials Lab, 1983.
15. J. Schijve, "Difference Between the Growth of Small and Large Fatigue Cracks in Relation to Threshold K Values," in Figure Threshold, ed. by J. Backlund et al., Vol.2, 1982, pp.881-908.

16. S. Taira, K. Tanaka and M. Hoshina, "Grain Size Effect on Crack Nucleation and Growth in Long-Life Fatigue of Low-Carbon Steel," ASTM STP 675, 1979, pp.135-163.
17. P. K. Liaw and W. A. Logsdon, "Crack Closure: An Explanation for Small Fatigue Crack Growth Behavior," Eng. Frac. Mech., Vol. 22, No. 1, 1985, pp. 115-121.
18. K. Tanaka and Y. Nakai, "Propagation and Non-Propagation of Short Fatigue Cracks at a Sharp Notch," Fat. Eng. Mat. Struct., Vol.6, 1983, pp. 315-327.
19. J. F. McCarver and R. O. Ritchie, "Fatigue Crack Propagation Thresholds for Long and Short Cracks in Rene'95 Nickel-Base Superalloy," Mat. Sci. Eng., 55, 1982, pp. 63-67.
20. J. C. Newman Jr., "A Nonlinear Fracture Mechanics Approach to the Growth of Short Cracks," AGARD Specialists Meeting in Behavior of Short Cracks, Toronto, Canada, Sept. 1982.
21. S. Banerjee, "A Review of Crack Closure," AFWAL-TR-84-4031, AFWAL/MLLN, 1984.
22. W. Elber, "Significance of Fatigue Crack Closure, Damage Tolerance in Aircraft Structure," ASTM STP 486, 1971, pp. 230-242.
23. W. Elber, "Fatigue Crack Closure Under Cyclic Tension," Eng. Frac. Mech., Vol. 2, 1970, pp.37-45.
24. M. Klesnil and P. Lukas, "Effect of Stress Cycle Asymmetry on Fatigue Crack Growth," Mat. Sci. Eng., Vol. 9, 1972, pp. 231-241.
25. K. Walker, "The Effect of Stress Ratio During Crack Propagation and Fatigue for 2024-T3 and 7075-T6 Aluminum," ASTM STP 462, 1970, pp. 1-14.
26. M. Jolles, "Constraint Effect on the Prediction of Fatigue Life of Surface Flaws," J. Eng. Mat. Tech., Vol. 105, 1983, pp. 215-218.
27. M. Katchner and M. Kaplan, "Effect of R-Factor and Crack Closure on Fatigue Crack Growth Rate for Aluminum and Titanium Alloy," ASTM STP 559, 1974, pp. 264-282.
28. J. Lankford, T. S. Cook and G. P. Sheldon, "Fatigue Microcrack Growth in a Nickel-Base Superalloy," Int. J. Frac., Vol.17, No.2, 1981, pp. 143-155.
29. R. T. Davenport and R. Brook, "The Threshold Stress Intensity Range in Fatigue," Fat. Eng. Mat. Struct., Vol.1, 1979, pp. 151-158.
30. P. C. Paris and G. C. Sih, "Stress Analysis of Cracks," ASTM STP 381, 1965, pp. 30-83.
31. D. L. Bowie, "Analysis of an Infinite Plate Containing Radial Cracks Originating at the Boundary of an Internal Circular Hole," J. Math. Phys., Vol. 35, 1956, pp. 60-71.

32. F. Gabrielli and R. M. Pelloux, "Effect of Environment on Fatigue and Creep Crack Growth in Inconel X-750 at Elevated Temperature," Met. Tran. A, Vol.13A, 1982, pp. 1083-1090.
33. J. Lankford and S. J. Hudak Jr, "Relevance of the Small Crack Problem to Lifetime Prediction in Gas Turbines", Proc. of Conf. on Life Prediction for High-Temperature Gas Turbine Materials, ed. by V. Weiss and W. T. Bakker, 1986, pp. 11-1-11-2.
34. D. Broek, Elementary Engineering Fracture Mechanics, Mar. Nij. pub., 1982.
35. L. Wagner, J. K. Gregory, A. Gysler, and G. Lutjering, "Propagation Behavior of Short Cracks in a Ti-8.6Al Alloy," Proc. of Conf. on Small Fatigue Cracks, ed. by R. O. Ritchie and J. Lankford, 1986, pp. 117-128.
36. M. R. James and W. L. Morris, "The Effect of Microplastic Surface Deformation on the Growth of Small Cracks," Proc. of Conf. on Small Fatigue Cracks, ed. by R. O. Ritchie and J. Lankford, 1986, pp. 145-156.
37. G. G. Trantina and M. Barishpolsky, "Elastic-Plastic Analysis of Small Defects-Voids and Inclusions," Eng. Frac. Mech., Vol. 20, No. 1, 1984, pp. 1- 10.
38. K. Tanaka and T. Mura, "A Dislocation Model for Fatigue Crack Initiation," J. Appl. Mech., Vol. 48, 1981, pp. 97-107.
39. J. M. Larsen, B. J. Schwartz, and C. G. Annis, Jr., "Cumulative Damage Fracture Mechanics Under Engine Spectra," Technical Report AFML-TR-79-4159.
40. D. Knueger, "Effects of Grain Size and Precipitate Size of the Fatigue Crack Growth Behavior of Alloy 718 at 427° C," General Electric AEG Report No. R85AEB133, 1985.
41. K. Bain, private communication, Allison GM, 1984.
42. T. Nicholas, J. H. Laflen, and R. H. Van Stone, "A Damage Tolerant Design Approach to Turbine Engine Life Prediction," in Proc. of Conf. on Life Prediction for High-Temperature Gas Turbine Materials, ed. by V. Weiss and W. T. Bakker, 1986, pp. 4-1 - 4-45

## APPENDIX A

### A Multi-Frequency A. C. Potential Drop System for the Measurement of Fatigue Micro-Cracks

The occurrence of fatigue cracks in safety critical structures and components, particularly in the aircraft industry, has led to the demand for a system capable of detecting and measuring very small surface cracks ( $<1$  mm). Presently, these components are designed employing a defect-tolerant design approach. This requires the determination of threshold stresses and stress intensities and near-threshold crack growth rates. Recent studies have demonstrated that the fatigue behavior of "short cracks" cannot be predicted from data obtained in long crack experiments. Consequently, there is considerable interest in the direct measurement of growth rates of very short fatigue cracks. The resolution required for crack length measurement in such studies far exceeds the capabilities of conventional techniques employed in "long crack" studies.

Participation in this mainstream of current fatigue research requires a system capable of accurate and continuous monitoring of very short crack lengths. In an attempt to meet this objective, a multi-frequency A. C. potential drop (A. C. PD) system for crack length measurement was built. Such a system is essential for the following reasons:

1. Resolution ( $\sim 1 \mu\text{m}$ )
2. Alternative means, such as replication, necessitates interrupting tests possibly resulting in "test transients" which obscure true behavior.
3. Measurements can be made in an environmental chamber.
4. Oxidation of surfaces during high temperature testing may prevent accurate measurement by any other means.



5. The A. C. PD technique is experimentally expedient, permitting investigations of broader scope, encompassing test variables of interest.

The unique ability of A. C. PD systems for resolving short cracks is a result of the "skin effect" associated with A. C. conduction. The skin depth is inversely proportional to the square root of the frequency of the power source. The system described below is notable for having a variable frequency capability allowing different skin depths to be scanned. This allows for the measurement of very short crack lengths as well as a determination of their shape (aspect ratio).

#### Electrical Field Measurements

Early attempts to detect and measure surface cracks have employed D. C. field measurements. The D. C. technique is illustrated in Figure A1 for a plate containing an edge crack. The electric field varies only in the x-y plane, it can be seen that in regions remote from the crack, the electric field strength is uniform but varies considerably near the crack tip. Potential probes with a fixed distance between contacts points can be used to measure the field. If used to measure the field remote from the crack, the measurement would always give the same value,  $V_{\infty}$ . Using the probe in regions close to the crack results in measured voltages less than  $V_{\infty}$  which decreases as the probe is moved closer to the crack. The relationship between  $V_1$  and  $V_2$  and the crack depth will be complex. Only if a full theoretical solution or an experimental calibration is available, can the crack depth be interpreted from these readings. In the case of a surface crack, the problem becomes more complex as the electric field distribution varies in three dimensions making both the theoretical and experimental calibration extremely difficult. In fact, it has been demonstrated that changes in crack curvature introduce significant errors in crack lengths if bowing is not accounted for during calibration.

A. C. PD systems are theoretically superior to D. C. Systems for measurement of surface cracks. The improved sensitivity is a result of the "skin effect" associated with A. C. conduction. The skin depth varies with the frequency of the power source according to the following equation:

$$\delta = \frac{1}{\sqrt{\pi \sigma \omega \mu \mu_0}}$$

Where  $\delta$  = skin depth

$\sigma$  = conductivity

$\omega$  = frequency

$\mu$  = permeability of the material

$\mu_0$  = permeability of vacuum

For example, if one used an AC power source of 5 KHz on mild steel, the skin depth would be about 130  $\mu\text{m}$ .

At low frequencies the skin depth is large and this makes it suitable for through-thickness crack length measurement. At high frequencies ( $\sim 100$  KHz), the skin effect is pronounced and the current flow is primarily in the outer boundaries of the specimen. With this skin effect, the measured potential would indicate local crack growth in the near-surface regions rather than through-thickness crack growth. Obviously, this phenomenon is highly desirable for the case of part-through surface cracks (see Figure A2).

One difficulty encountered in using the AC method is that the impedance of the electrical circuit is sensitive to mechanical stress, chemical composition; etc. This means that the use of some remote calibration device could lead to unacceptable errors. In

applying this approach it would be preferable to make all the field measurements directly on the metal test specimen. This is only possible if all stray voltages are eliminated from the measuring system so that the local measured voltage is the true voltage at the metal surface. Recent advances in the understanding of this problem make it possible to measure the true surface voltage. Consequently, a much improved AC field measurement system can be constructed and used for most metals. These A. C. field measurements can be interpreted in terms of crack depth and shape.

#### Comparison of A. C. and D. C. Methods

The advantages and disadvantage of the two techniques are listed in Table A1. The major advantages of the DC method are that it does not rely on advanced electronics and for certain specimen sizes and geometries, it is a well-known, established technique. However, it does have the disadvantage of a complex relationship between PD and crack length and the problems inherent in handling low-level, millivolt, DC signals including difficulties arising from thermal EMF effects.

The major advantage of the AC technique are the ease of calibration for different specimen geometries and the lack of size dependence of the technique as well as the high sensitivity to small crack detection.

#### System Design

A schematic of the AC potential system is shown in Figure A3. The system consists of two basic segments; these are the excitation circuit which supplies a constant AC current to the specimen, and the measurement circuit which detects the AC potential drop across the specimen. These circuits are interconnected through a lock-in amplifier.

The lock-in amplifier has two basic functions in this system. First, a 1 volt AC reference signal drives the power amplifier at the reference frequency. Second, the lock-in

measures the amplitude of the AC potential across the specimen, but unlike an AC voltmeter, the lock-in accepts for measurement only that component of the potential at the reference frequency. The use of asynchronous rectifies, instead of a lock-in amplifier, would add complications in that the phase characteristics of the filtering becomes important and careful attention must be given to the oscillator and filter stability and matching.

In principle, all that is required from the power source is a sufficient current ( $\sim 2$ amps) through the test piece. However, to monitor cracks over a period of time, it is essential that the current be held at a constant value so that the voltage readings can have long-term significance. Current stability is largely a matter of economics, but a long term stability of better than .1% is definitely required.

In order to produce variable skin depth, a sweep oscillator or frequency synthesizer will be used to drive the power supply. The oscillator must be capable of low distortion such that the signal be reasonably sinusoidal to prevent harmonic causing, radio frequency interference. For practical purposes the oscillator should cover the range of 1 Hz-200 KHz.

The input signal consists of the desired potential signal at the reference frequency combined with broad-band noise picked-up from stray magnetic and electrical fields and other sources. Since the potential signal at the specimen is small ( $\leq 100 \mu V$ ), the signal-to-noise ratio of the input signal may also be quite small and the resolution of the potential signal within the noise may be unacceptable. The frequency discrimination characteristic of the lock-in is used to selectively amplify the desired potential signal for measurement. The noise rejection capabilities of available lock-in amplifiers allow them to handle signals with signal to noise ratio as low as 0.1. The process for finding a submerged signal begins by preamplifying the entire input signal and then attenuating the frequency component above and below the reference frequency through a bandpass filter. A phase-sensitive-detector then reverses the polarity of the remaining signal each half period of the reference

frequency. This causes the reference frequency component of the signal to reverse polarity at every integral half-period, causing that component to become rectified and produce an average net DC component. All portions of the signal at the input of the phase-sensitive-detector, which do not have the reference frequency, reverse polarity at some non-integral multiple of their half-period, producing an average zero net DC component. A capacitive filter then converts the rectified reference frequency signal into a DC signal with a ripple factor which depends on the filter time constant. This DC signal is proportional to only that component of the original input signal which entered the lock-in at the reference frequency. The amplified DC signal is then digitized and stored for further data analysis.

#### Approach

A multi-frequency A. C. PD system was built to study the fatigue behavior of "short cracks" at elevated temperature, in air and in an environment chamber. Although the system is capable of crack sizing in the case of multiple surface cracks, greater accuracy can be obtained by consideration of singular surface cracks of known origin. In this short crack study, cracks were artificially initiated at carefully made EDM pits. Potential measurement probes were welded at precise locations on either side of the initiation site. The potential probes were metal foils at the location of attachment to prevent unintended initiation due to local penetration, as would be the case with round wire. A semi-elliptical surface crack with potential probes is depicted in Figure A4.

A brief summary of the data analysis will be presented here.

The crack geometry is described in Figure A5 where  $a$  denotes the crack depth on the center line,  $2c$  the length of the crack trace on the surface,  $x$  and  $y$  are the axes in the plane of the metal surface. The A. C. power supply provides a constant current  $I_0$  through the specimen test section via remote attachment. For a given frequency, a constant current is maintained by application of an electric field  $E_0$ . The value  $E_0$  is dependent on the

overall impedance of the specimen between the location of attachment of the power supply. This impedance will increase with increasing crack lengths in the specimen gauge section resulting in an increase in  $\vec{E}_0$  required to maintain a constant current.

The value of  $\vec{E}_0$  is also dependent on the applied frequency. As the frequency is increased, the skin depth decreases according to Equation 1 resulting in a higher current flux  $\vec{J}_0$  according to

$$\vec{J}_0(\omega) = \frac{\vec{I}_0}{2 \pi r \delta(\omega)} \quad (2)$$

Consequently, the applied potential of the power supply must vary as

$$\vec{E}_0(\omega) = \rho_0 \vec{J}_0(\omega) \quad (3)$$

The equation governing the electric field in the metal interior is

$$\nabla^2 \vec{E}(x, y) = \mu \sigma \frac{\partial \vec{E}}{\partial t} \quad (4)$$

The field on the metal surface is shown in Figure A6 and the discontinuous difference in potential which occurs across the surface edge of the crack, denoted by  $V_c$ , is now evident. if we solve for  $E(x, y)$  for a fixed frequency knowing the boundary conditions and  $E_0 = E_0(\omega)$ , the solution to Equation 4 can be used to determine the potential drop across the crack. The maximum value of this potential difference, which occurs on the crack center-line is

$$V_c(0) = \vec{E}(0, y^+) - \vec{E}(0, y^-) \quad (5)$$

$$V_c(0) = \frac{4_c \vec{E}_0}{n} \cotan \frac{\pi}{n} \quad (6)$$

where  $n$  is related to the crack aspect ratio by

$$a = \left| c \cotan \frac{n\pi}{4} \right| \quad (7)$$

The distribution of  $V_C$  along the surface edge is shown for various aspect ratios in Figure A7. For a given punctual position of the probe ( $x/c$ ) and by changing the frequency, therefore changing  $E_0$ , the value of  $n$  can be obtained numerically. With this value of  $n$  and Equations A6 and A7,  $c$  and  $a$  can be determined uniquely. These calculations must be confirmed by an experimental calibration.

The utility of the multi-frequency capability is now evident in that it permits continuous determination of aspect ratios as well as effecting maximum sensitivity over a range of cracks lengths.

#### A Demonstration of System Capabilities

The A. C. potential drop measurement system described above was assembled. A calibration experiment was performed. A short crack was propagated in Inconel 718 at room temperature under fully reversed loading at near threshold stress intensities. A crack growth rate of approximately  $5 \times 10^{-9}$  m/cycle was observed. A current of 1 amp (rms) at a frequency of 40 KHz was employed. The test was periodically interrupted to record the potential at zero load and at 80% of maximum load. The surface crack length was measured directly using the plastic replica technique. The results are plotted in Figure A8.

There are numerous features of this plot which require explanation. The most obvious is the sudden increase in potential beyond a surface crack length of 800  $\mu\text{m}$ . This is a result of the geometry of the potential probes. As shown in Figure A4a, the foil width was exactly 800  $\mu\text{m}$  in this experiment. This illustrates the importance of using punctual

probes. The foil design shown in Figure A4b was used in future experiments. Punctual probes, approximated by the foil in this experiment for crack lengths beyond 800  $\mu\text{m}$ , effects a greater resolution in crack length increment and results in a steeper slope. A resolution of 1.6  $\mu\text{m}$  demonstrated in this experiment, is quite adequate for studying the fatigue behavior of short cracks. The system is inherently capable of a resolution of better than 0.1  $\mu\text{m}$  in crack length increment!

Also noteworthy is the increase in potential at 80% of maximum load. This indicates that the system is capable of measuring crack closure stresses. The crack closure phenomenon is believed to play an important role in the fatigue behavior of short cracks. To simultaneously measure and record load, in addition to potential, an analog-digital converter has been added to the system design.

#### System Shortcomings

Although the system calibration at room temperature (Figure A8) was encouraging, attempts to proceed to continuous monitoring of crack growth rates in elevated temperature fatigue tests were unsuccessful. Potential measurements proved to be unstable over long periods of time ( $> 4$  hrs.), even at constant crack length. The calibration experiment was performed in about 3 hours. This problem was later attributed to instability in the A. C. power supply. This component was custom built by an outside electronics firm. Consequently, being a one-of-a-kind item, the iteration process required for perfecting this unit was bypassed.

Since the principal objective of this research was to measure the fatigue behavior of small cracks at elevated temperature, testing proceeded using the plastic replication technique for measuring crack lengths. This same system, with an improved A. C. power supply, was later successfully used in a study of stress corrosion crack initiation in a nickel-base superalloy tested under monotonic loading in a PWR environment.



Table A1

	ADVANTAGES	DISADVANTAGES
d.c.	<ol style="list-style-type: none"> <li>1. Simple technique does not rely on advanced electronics.</li> <li>2. Well established technique for certain specimen sizes and geometries.</li> </ol>	<ol style="list-style-type: none"> <li>1. Complex relationship between P.D. and crack length.</li> <li>2. Thermal emf effects.</li> <li>3. Technique sensitive to specimen size and geometry.</li> </ol>
a.c.	<ol style="list-style-type: none"> <li>1. Ease of calibration for differing specimen geometries.</li> <li>2. Inherently linear response.</li> <li>3. Lack of size dependence of method.</li> <li>4. Ease of amplification of input signal.</li> <li>5. Multiple P.D. probe systems can be used.</li> </ol>	<ol style="list-style-type: none"> <li>1. Reliance on advanced electronics.</li> <li>2. Lead interaction.</li> <li>3. Requirement for high stability in electronics.</li> </ol>

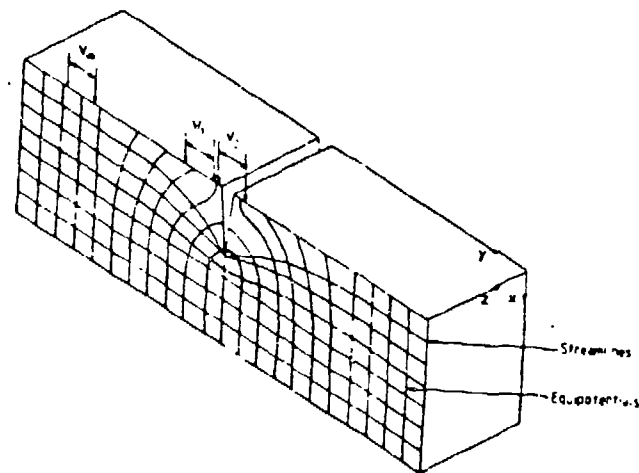


Figure A1 Illustration of the d.c. electrical field distribution for an edge crack specimen

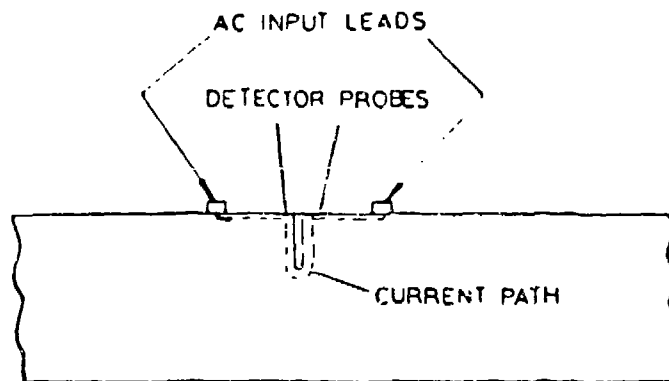


Figure A2 Illustration of the skin effect associated with a.c. conduction

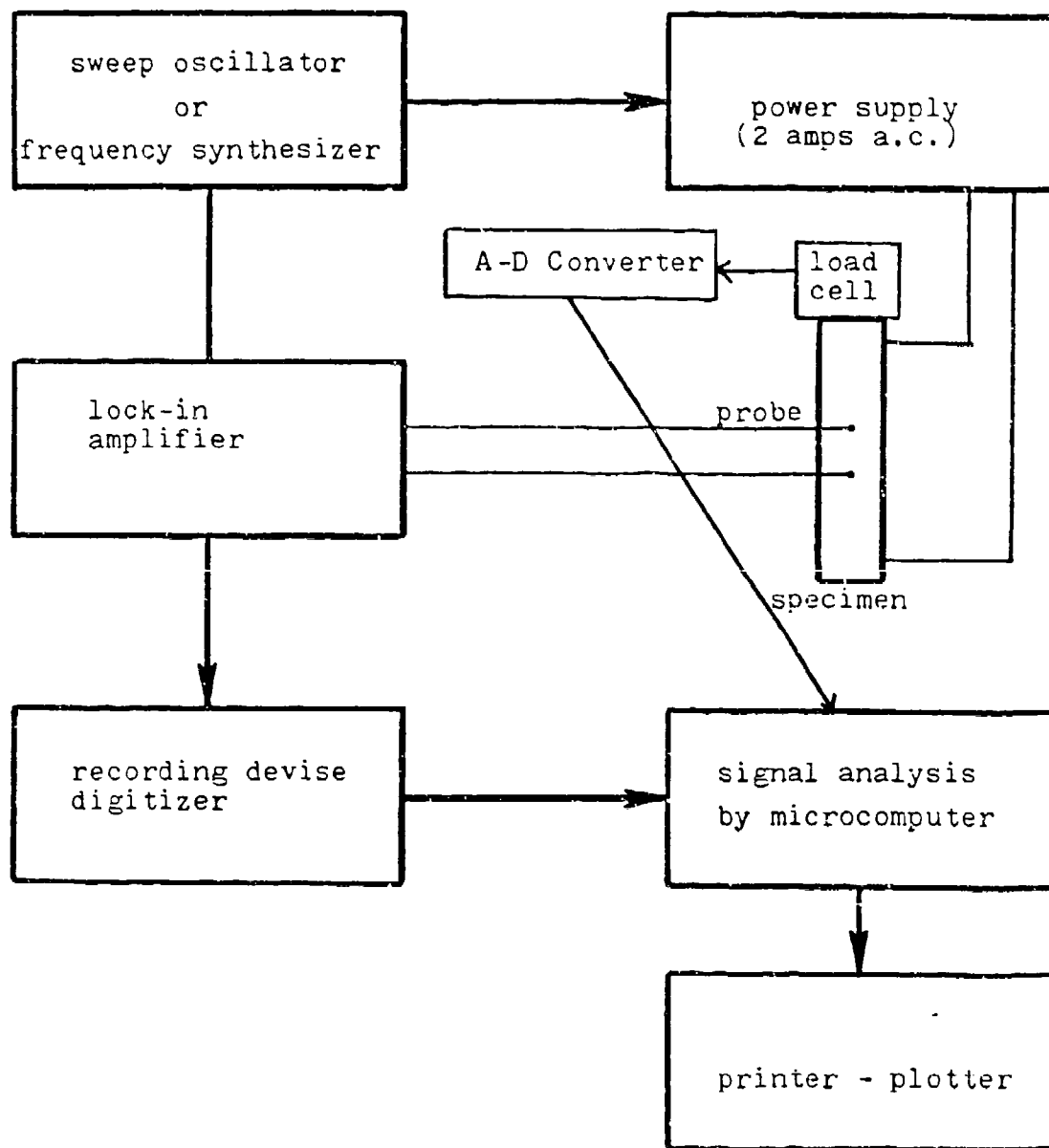


Figure A3 Schematic diagram of the multi-frequency a.c. potential drop system for crack length measurement

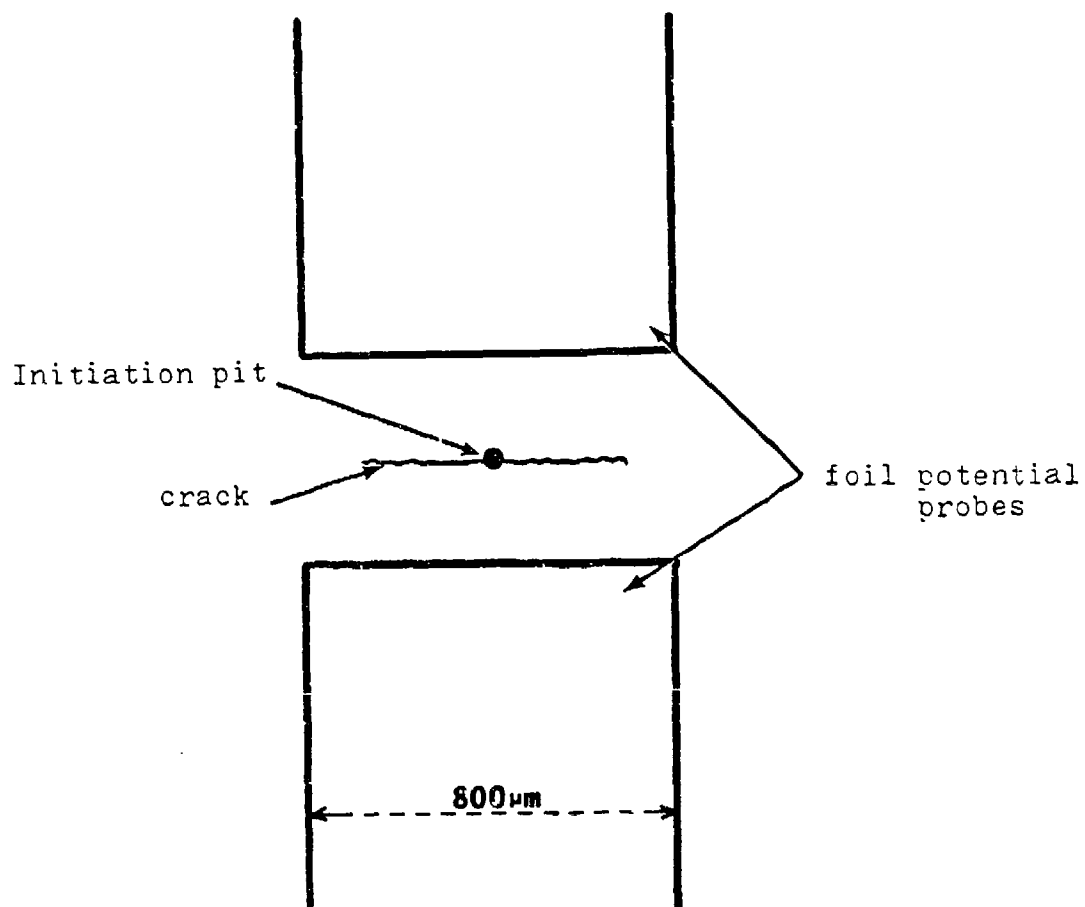


Figure A4.a Illustration of potential probes used in the calibration experiment

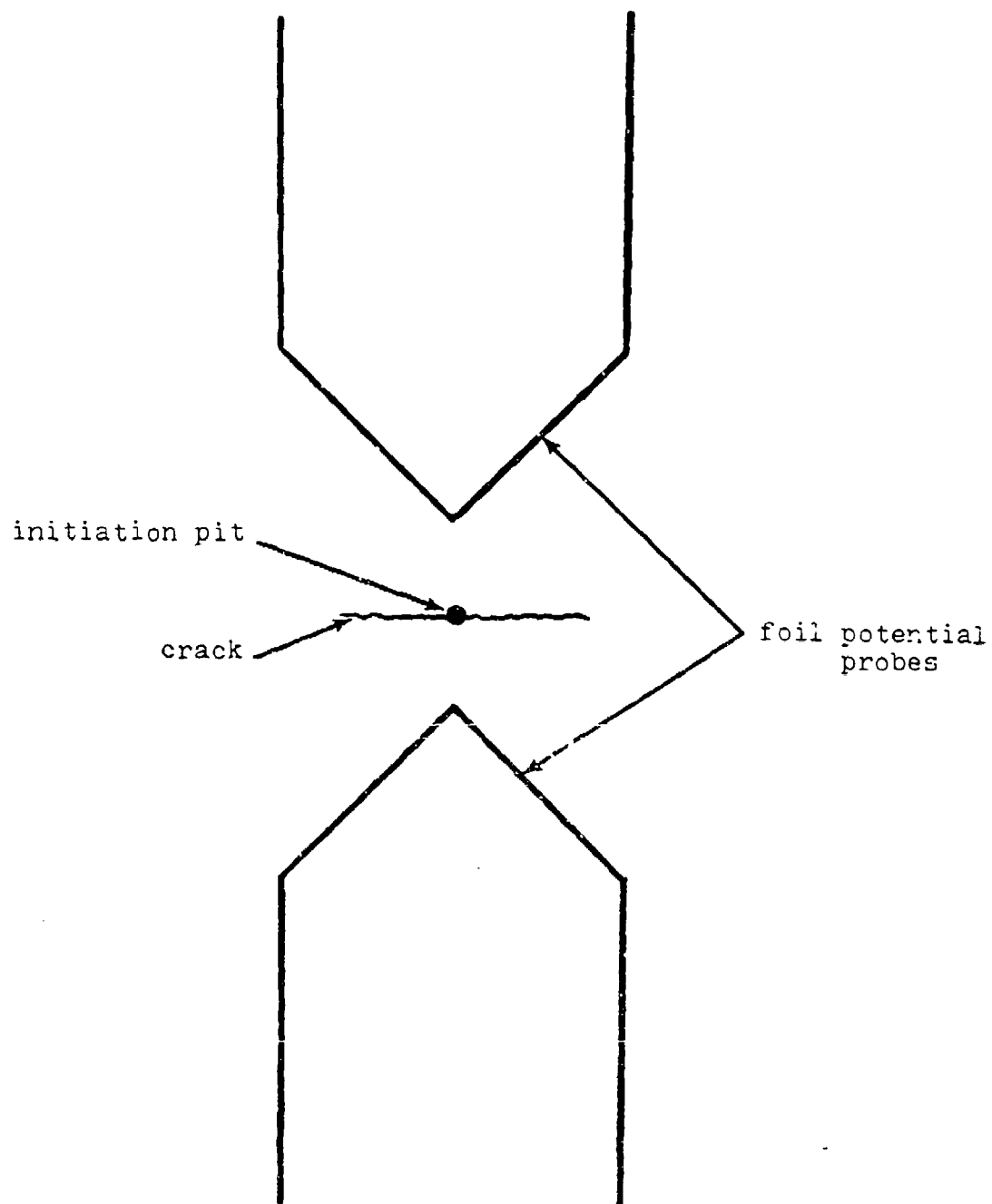


Figure A4.b Illustration of potential probes to be used in subsequent experiments. This geometry will serve as an ideal punctual probe.

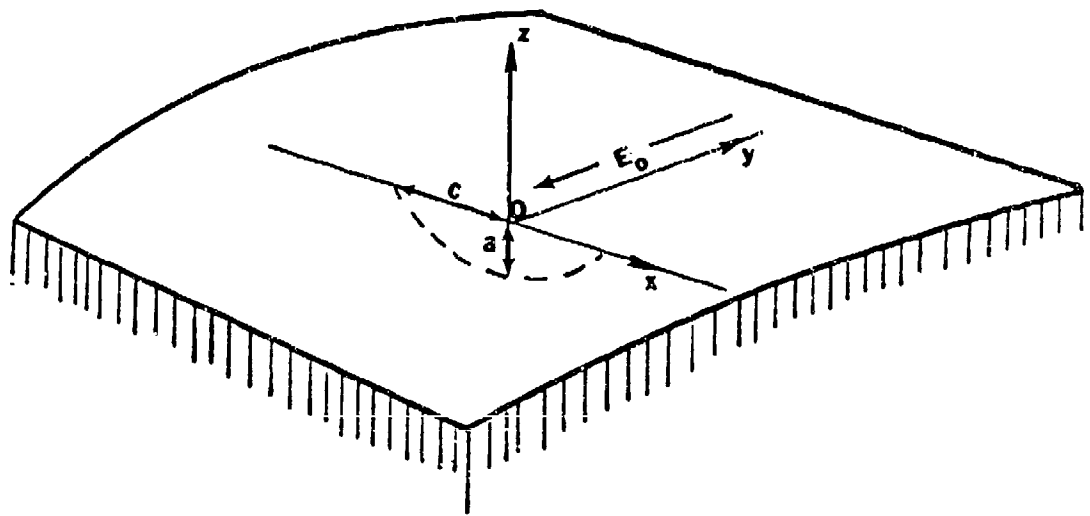


Figure A5 General description of a symmetrical surface crack

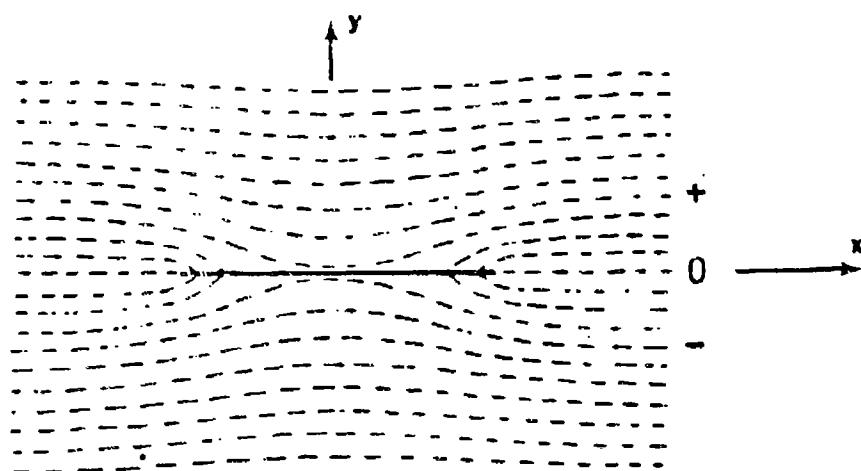


Figure A6 Lines of constant potential on the metal surface around crack

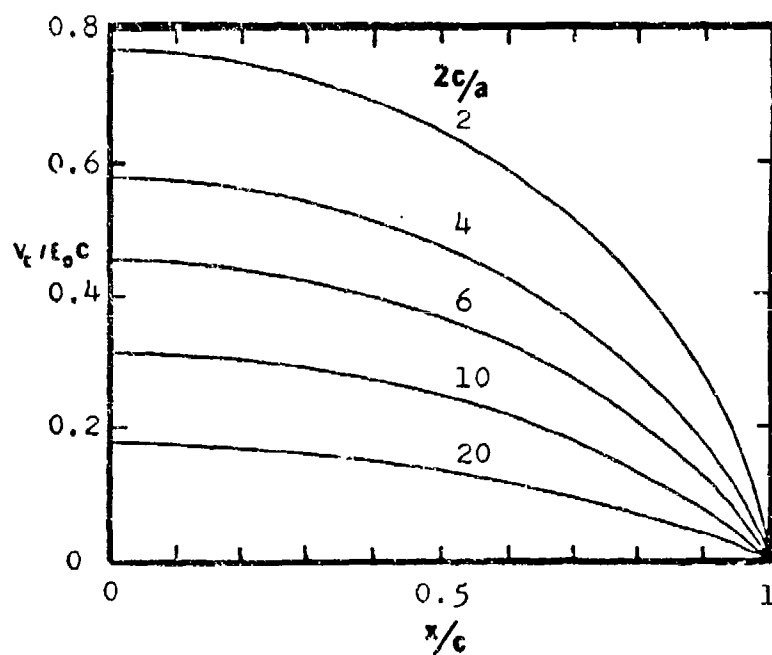


Figure A7 Distribution of the discontinuous difference in potential across a circular arc crack for various crack aspect ratios

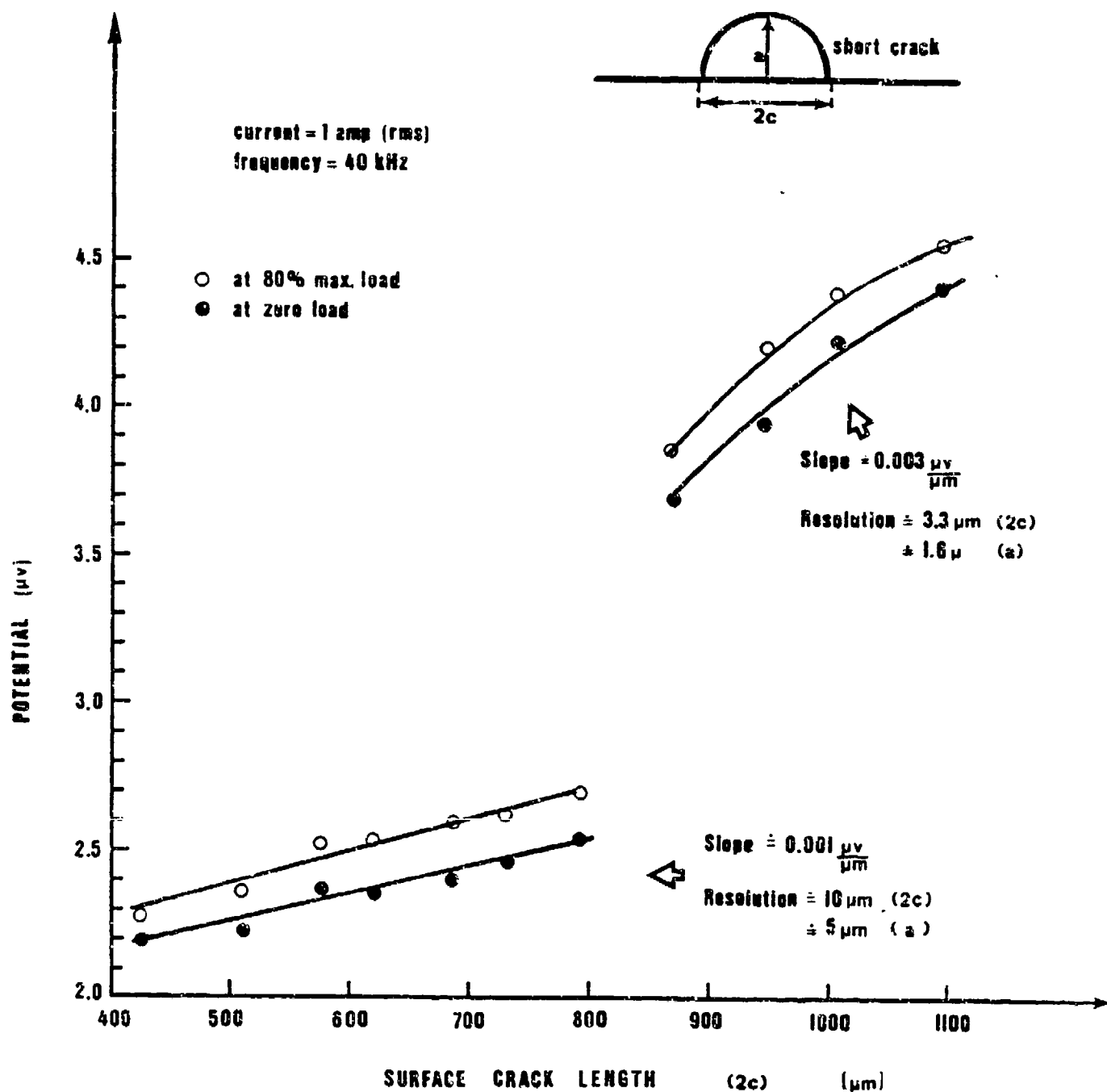


Figure A8 Potential drop calibration illustrating:  
1) the importance of using punctual potential probes  
2) a high resolution in crack length increment  
3) the ability to detect a crack closure stress



## APPENDIX A References

1. K. Wallin, T. Saario, P. Auerkari, H. Saarelna and K. Torronen, "Comparison of Potential Drop and Unloading Compliance Methods in Determining Ductile Crack Extension," Elastic-Plastic Fracture Test Methods: The user's Experience, ASTM STP 856, E. T. Wessel and F. J. Loss, Eds., American Soc. for Testing and Mat., 1985, pp. 363-374.
2. T. V. Tenkatasubramanian and B. A. Unvala, "An AC Potential Drop System for Monitoring Crack Length," Journal of Physics and Eng. Sci. Instrument., V. 17, 1984.
3. I. Verpoest, E. Aernoudt, A. Deruyttere and M. Neyrinck, "An Improved A.C. Potential Drop Method for Detecting Surface Microcracks during Fatigue Tests of Unnotched Specimens," Fatigue of Engineering Materials and Structures, V. 3, 1981, pp. 203-217.
4. D. H. Michael, R. T. Waechter and R. Collins, "The Measurement of Surface Cracks in Metals by Using A. C. Electric Field," Proc. R. Soc. Lond A381, 1982, pp. 139-157.
5. D. H. Michael, R. Collins, and W. D. Dover, "Detection and Measurement of Cracks in Threaded Bolts with an A. C. Potential Difference Method," Proc. R. Soc. Lond, A385, 1983, pp. 145-168.
6. F. D. W. Charlesworth and W. D. Dover, "Some Aspects of Crack Detection and Sizing using A. C. Field Measurements," in The Measurement of Crack Length and Shape During Fracture and Fatigue, Edited By. C. J. Beevers, EMAS, West Midlands, U. K., 1982.
7. I. Verpoest, E. Aernoudt, A. Deruyttere and M. Neyrinck, "An A. C. Potential Drop Method for Detection and measurement of Surface Microcracks during Fatigue Testing of Wires," in The Measurement of Crack Length and Shape During Fracture and Fatigue, Edited by C. J. Beevers, EMAS, West Midlands, U. K., 1982.
8. D. Mirshekar-Syahkal and R. Collins, "Induction Effects during Crack Measurement by the A. C. Field Technique," in The Measurement of Crack Length and Shape during Fracture and Fatigue, Edited by C. J. Beevers, EMAS, West Midlands, U. K., 1982.
9. K. R. Wari, "A Consideration of an A. C. Potential Drop Method for Crack Length Measurement," in The Measurement of Crack Length and Shape during Fracture and Fatigue, Edited by C. J. Beevers, EMAS, West Midlands, U. K., 1983.
10. R. P. Wei and R. L. Brazill "An A. C. Potential System for Crack Length Measurement," in The Measurement of Crack Length and Shape during Fracture and Fatigue, Edited by C. J. Beevers, EMAS, West Midlands, U. K., 1983.